



DTIC FILE COPY

AD-A201 170

Contract N00014-87-F-0066

Annual Report
 to the
 Strategic Defense Initiative Organization
 on the
 Free-Electron Laser Driven by the NBS CW Microtron
 for the period
 April 1, 1987 to March 31, 1988
 by the
 U.S. Department of Commerce
 National Bureau of Standards
 and the
 U.S. Department of Defense
 Naval Research Laboratory

DTIC
ELECTE
S **D**
 OCT 27 1988
 GIVE
 E

This document has been approved
 for public release and only its
 distribution is unlimited.

88 9 16 22 7

TABLE OF CONTENTS

1. Project Goals 1

2. Activities and Accomplishments 1

 2.1 System Design, FEL Physics, and Performance Calculations. 2

 2.2 Optical Cavity and Wiggler. 4

 2.3 RTM and Electron Beam Transport 6

 2.4 High-Current Injector 8

 2.5 User Facility 10

3. Plans for the Coming Year. 11

4. Publications 12

5. Talks. 13

6. References 13

7. Appendices

 Appendix A - NBS-NRL Free-Electron Laser Conceptual Design Report

 Appendix B - Design Note 1 - Issues Involved in the Choice of
 Injector Pulse Frequency and Optical
 Cavity Length

 Appendix C - Design Note 2 - RTM Shielding Requirements

 Appendix D - Design Note 3 - Optical Cavity Length Choice

 Appendix E - Design Note 4 - Electron Beam Transport Design

 Appendix F - Design Note 5 - Predicted FEL Performance at 74.375
 MHz

 Appendix G - Design Note 6 - FEL Optical Cavity

 Appendix H - Design Note 7 - Tuning the Optical Wavelength and
 Diffraction Losses in the IR

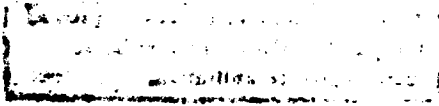
 Appendix I - Design Note 8 - Electron Beam Phase Stabilization

 Appendix J - Design Note 9 - Lasing on the Harmonics

 Appendix K - Analysis of Free Electron Laser Performance Utilizing
 the National Bureau of Standards' CW Microtron

 Appendix L - Reflection Matrix for Optical Resonators in FEL
 Oscillators

Accession For	
NTIS GRA&I	
DTIC TAB	
Unannounced	
Justification	
By	
Distribution/	
Availability Codes	
Dist	Avail and/or Special
A-1	



1. Project Goals

The overall goal of this project is to construct and bring into operation a free-electron laser (FEL) driven by the racetrack microtron (RTM) electron accelerator at NBS. NBS is providing the RTM, radiation-shielded laboratory space for the RTM and FEL, and experimental areas. The scope of the project includes: modifying the RTM injector for increased peak current; developing electron beam transport from the RTM to the FEL; developing a wiggler and optical cavity; and developing optical beam transport and diagnostics. The plan for the completed facility is shown in Figure 1 of Appendix K.

2. Activities and Accomplishments

In the first year of the project good progress was made on many fronts. The accomplishments are summarized here and are presented in more detail in the sections that follow. The conceptual design of the FEL was completed, including decisions on optical cavity length and pulse frequency, and detailed calculations were done to predict its performance. For the wiggler, specifications were written, proposals from several potential vendors were evaluated, a vendor was selected, and a contract was prepared for signing. The shielded room that will house the FEL was cleared of other equipment. Three schemes to increase the RTM peak current were identified and are being investigated. The 5 MeV RTM injector beam tests were completed, and the electron transport line from the injector to the RTM was installed. The beam-optical design of

Keywords: Electron beam
stabilization; Laser cavities; Diffraction loss;
Infrared lasers. (edc) *

the electron transport line from the RTM to the FEL was completed. Requirements for the user facility were identified, and we began clearing the existing experimental area and designing the new one.

2.1 System Design, FEL Physics, and Performance Calculations

On September 9, 1987 a conceptual design review of the NBS-NRL FEL was held at NBS. Members of the design team presented all aspects of the design to the project staff and to two outside consultants, Dr. Richard Freeman of AT&T Bell Laboratories and Dr. Lloyd Young of Los Alamos National Laboratory. The presentations and discussions that took place are summarized in the Conceptual Design Report, which is attached to this report as Appendix A. In addition, detailed design notes on different aspects of the FEL were written by the project staff throughout the year. These are attached as Appendices B-J.

We have used the self-consistent, three-dimensional computer code SHERA, which was developed at NRL, to assess the effects of the transverse emittance of the electron beam on the performance of the FEL. A complete description of this work is given in Appendix K. We calculated values of the small-signal power gain, G_p , for normalized transverse emittance, ϵ_n , between 5 mm·mrad (or μm) and 20 μm , with the results shown in Figure 5 of Appendix K. The design value of ϵ_n for the RTM is 5 μm , and the measured value for the 5 MeV injector beam is less than 1 μm . The power gain calculated for the design emittance will readily support lasing over the planned wavelength range. It may also be

seen from Figure 7 of Appendix K that, due to the good emittance, some electron-beam guiding of the optical beam can be expected for the nominal peak electron current of 2 A.

We have developed a Gaussian optical beam formalism for including mirrors in SHERA to convert it to an oscillator code. This will allow us to study the evolution of radiation in the optical cavity and evaluate performance of the FEL in the presence of diffraction and mode mixing. This work is described in Appendix L. Meanwhile, we have used published diffraction tables to estimate losses from the mirrors and intracavity vacuum chamber apertures. These losses are negligible for UV and visible wavelengths and are small for the IR wavelengths at which we plan to lase. The losses from diffraction on the vacuum chambers of the wiggler and the electron beam dump magnet are estimated to be 0.6% and 0.2% per pass, respectively, at 10 μm . These losses increase rapidly with wavelength and will prevent lasing at wavelengths above 12 μm . Details of these calculations are given in Appendices G and H.

Imperfections in the wiggler magnetic field can degrade FEL performance by causing the electrons to "walk" off the radiation axis and by altering the path length of the electrons and hence their phase relative to the radiation field. In order to evaluate these effects, we have developed computer codes to model the propagation of electrons through wiggler fields with errors and with no radiation field, and have checked the results for agreement with analytic expressions. We have also modified computer code SHERA to include wiggler field errors. A preliminary SHERA calculation was performed for a wiggler with no electron steering correction and with 0.5% rms random (uncorrelated)

field errors. The phase error calculated for this case would degrade performance significantly. The real wiggler, however, will have electron steering coils and field errors that are predominantly correlated, both of which will reduce phase errors substantially. We are currently incorporating these features into the formalism and computer codes.

For a saturated FEL in the one-dimensional, low-gain model with a perfect, untapered, N-period wiggler, the maximum efficiency for extracting power from the electron beam is $1/2N$.¹ Using this model, we have estimated the optical output power of our FEL for commercially available laser mirrors. This work is presented in Reference 2 and in Appendix G. The calculated cw output power is in the range 50-200 W for $200 \text{ nm} \leq \lambda < 7 \text{ } \mu\text{m}$, and is approximately 20 W for $7 \text{ } \mu\text{m} < \lambda \leq 10 \text{ } \mu\text{m}$. We are performing more accurate, three-dimensional calculations.

2.2 Optical Cavity and Wiggler

The conceptual design of the optical cavity is complete. Details are given in Appendix G. We have chosen a two-mirror, linear cavity with a mirror spacing of 8.062 m. This spacing gives a round trip light travel time of 53.78 ns, which, at the RTM injector frequency of 74.375 MHz, implies that there will be two electron pulses and four light pulses in the optical cavity at one time. Since the RTM is a cw accelerator and there is gain in the laser only when an electron bunch is present, the FEL behaves as a cw, harmonic-mode-locked laser. The cw nature of the accelerator results in very high average output power for the FEL.

For cavity mirrors, we plan to use multi-layer dielectric (MLD) coatings on transparent substrates. An advantage of MLD coatings is the ability to couple the light out through one mirror by using a partially transmitting/partially reflecting MLD coating. Compared to metal mirrors, the spectral bandwidth, or tuning range, is narrow. However, in the visible and UV, metal mirrors cannot be constructed with the high power reflection coefficients (up to $R = 99.9\%$) that are necessary because ours is a low-gain laser. The cavity mirrors must have high damage thresholds, as we expect the peak irradiance to be $1-2 \text{ GW}\cdot\text{cm}^{-2}$, and the average power to be $200-400 \text{ kW}\cdot\text{cm}^{-2}$. As discussed above, the losses from diffraction on the cavity mirrors and the intracavity vacuum chamber apertures will be negligible at ultraviolet and visible wavelengths and small at the infrared wavelengths at which we plan to operate.

The minimum wavelength for lasing can be reduced by lasing on the third harmonic because G_p for the third harmonic exceeds that for the fundamental, as discussed in Appendix J. This is done by maintaining a high-Q optical cavity at the desired wavelength while decreasing the electron beam energy by the factor $3^{-1/2}$. We may be able to reach 150 nm by this means.

The wiggler will have a peak field of 0.54 T, 130 periods of 2.8 cm for UV and visible operation, and 65 periods for IR operation. Specifications for the wiggler were written in June, 1987, and a request for proposals was sent to potential wiggler contractors in August. Several proposals were received in October and were evaluated by an internal technical committee, with Dr. Brian Kincaid (AT&T Bell

Laboratories) acting as an outside consultant. Negotiations with prospective vendors began in November. A signed contract is imminent.

The room where the wiggler and optical cavity will be located has been cleared of interfering equipment. We have measured ionizing radiation levels in this area during operation of the NBS neutron time-of-flight facility, when a 5 kW electron beam from the NBS 110 MeV linac passes through the FEL area. The measured radiation levels are in the range of 10-100 krad per year, which will give the samarium-cobalt wiggler magnets an estimated useful lifetime of 5000 years. Lifetimes of optical components at this radiation level will be 1-10 years, longer than lifetimes due to optical radiation damage. We have also initiated sound and vibration measurements in the room in order to determine isolation specifications for the optical cavity.

2.3 RTM and Electron Beam Transport

The RTM, which is described in Reference 2, consists of a 5 MeV injector feeding a microtron. In the microtron, a pair of 180° end magnets are used to recirculate the electron beam through a 12 MeV rf linac up to 15 times for an energy gain of up to 180 MeV. See Appendix E, Figure 1. The beam can be extracted from any of 14 separate return lines in 12-MeV steps. In the past year, 5 MeV injector beam tests were completed, and the beam transport line between the injector and microtron was installed. The 12 MeV linac was rf-tested at full power, and all beam transport components on the linac axis and the end magnet vacuum chambers were installed. All magnets for the return lines were designed, and beam-optical design of the transport line between the RTM and the FEL

was completed. We are currently preparing to perform 17 MeV beam tests with one pass through the linac.

The results of the RTM injector beam tests are given in Reference 3. The measured, normalized transverse emittance at 5 MeV is less than $1 \mu\text{m}$, considerably better than the $10 \mu\text{m}$ required for FEL operation at wavelengths down to $90 \mu\text{m}$. The measured energy spread of 5 keV at 5 MeV is below the criterion of 0.4% for lasing. Furthermore, we expect the fractional energy spread to decrease with increasing beam energy.

The 5 MeV beam transport system between the injector linac and the RTM linac axis is now complete, including alignment of all bending magnets and quadrupole focusing magnets, and leak checks of the vacuum envelope. All magnets on the accelerator axis have been installed and aligned.

The two sections of the 12 MeV linac on the RTM axis have each been conditioned to a power level between 115 kW and 120 kW. This corresponds to a voltage gradient exceeding that required for accelerating the recirculating beam to the nominal full energy of 185 MeV. A beam line for testing the beam after one pass through the 12 MeV linac is presently being installed at the exit of end magnets E1. This beam line includes a high-power beam stop and sufficient beam profile monitors for beam emittance and energy spread measurements.

Designs have been completed for the steerers, $S_{19} - S_{21}$, and for quadrupoles Q_{10} and Q_{11} on the RTM return lines. The electron beam optics design for the RTM-FEL beam transport line is complete and is presented in Appendix E. This design includes proper transport of the RTM beam over all energies between 29 MeV and 185 MeV, and provides for

an achromatic beam on the FEL axis. Preliminary designs have been established for the movable deflecting magnet, D11, and the first two dipole magnets, D_{12H} and D_{12V}. The remaining magnets in the transport line are (See App. E, Figs. 1 and 3): three 2-inch-bore quadrupole doublets and a dipole bending magnet in the RTM room; two quadrupole doublets that act as a telescope to form the optimal beam size and waist position on the FEL axis; an achromatic system of 4 dipoles to guide the electron beam around the upstream cavity mirror; and a 90° beam dump magnet before the downstream mirror.

2.4 High-Current Injector

The RTM injector consists of a 100 kV, 5 mA dc, thermionic electron gun followed by a chopper/buncher system and a 5 MeV cw linac. The injector produces beam pulses at 2380 MHz (the rf drive frequency) with a maximum of 0.35 pC per pulse. A peak electron beam current of 2-4 A is required in the FEL to achieve lasing. For a 3.5-ps long beam pulse, this is 7-14 pC per pulse. We have proposed to increase the charge per pulse without increasing the average current in the RTM (limited by the rf power available) by reducing the beam pulse frequency to 74.375 MHz, the 32nd subharmonic of the rf frequency.

We are investigating three possible ways to achieve the required charge per pulse: subharmonic bunching, a laser-driven photoelectron gun, and subharmonic chopping. In the subharmonic bunching option, a 3-ns long pulse from a 110 kV thermionic gun goes through a bunching cavity operating at 74.375 MHz and is compressed to 70 ps. The beam is then further compressed by the existing buncher to 15 ps before entering the

injector linac, where it is further compressed to 3 ps. This technique has the advantage of having low source currents, but impresses a large energy variation ($\pm 20\%$) on the beam due to the large bunching ratios needed.

An electron gun driven by a mode-locked, cw laser requires a photocathode with a 1% quantum efficiency and a one-week lifetime to be acceptable for user facility operation. We are collaborating with the AT-7 group at Los Alamos to identify a suitable cathode material. Several materials have been found with more-than-adequate quantum efficiency, but their lifetimes are short: a few hours even in high vacuum (10^{-10} Torr) at average currents that are less than 2% of what we require. Further tests at higher currents will begin soon at Los Alamos with a dc gun configuration. Meanwhile, we have been operating a cw, mode-locked Nd:YAG laser as a prototype photocathode driver.

A very promising, recently-conceived method of increasing the peak current involves replacing the present dc electron gun with a 100-150 mA, 110 kV, thermionic gun pulsed at 74.375 MHz. The 2-ns long gun pulses would then be chopped and bunched to the required length. The required electron gun is commercially available, the chopper would be similar to the existing one, and the existing buncher would remain intact. We are currently doing design calculations for this system. After completion of these calculations and the Los Alamos dc photocathode tests early this summer, we will decide which method to use.

2.5 User Facility

The user facility will consist of two experimental rooms. The first, XA1, is an existing room adjacent to the FEL, about 1600 ft² in area and approximately 40 ft below ground level. It contained a beam transport line and a magnetic spectrometer connected with the NBS 110 MeV linac. We removed most of this equipment this year for conversion to the FEL facility. A building addition at ground level will contain a second experimental area, XA2, of about 2400 ft². In the past year we visited several laser laboratories to define requirements for experimental areas. We will take several precautions to minimize vibrations and sound in the user facility. These include: thick exterior walls to minimize wind-induced vibrations; isolation of motors, etc. from the experimental area; and constant, laminar-flow air conditioning. We also drilled a test hole for location of the optical transport system between the two experimental areas. A feasibility study is underway to determine if the site provides satisfactory support for the proposed addition. A preliminary building design was completed, and we are preparing a bid package for engineering and architectural design and construction.

3. Plans for the Coming year

In the period April 1, 1988 through March 31, 1989, we plan to:

- Select a method of increasing the charge per pulse of the 100 keV injector to at least 7 pC.
- Design components for a new injector based on the method selected.
- Perform one-pass beam tests of the RTM linac.
- Procure components for the RTM return beam lines and the RTM-FEL beam transport line.
- Sign a contract with a wiggler vendor and oversee the magnetic and engineering design and initial construction of the wiggler.
- Calculate the FEL gain using computer program SHERA and a realistic model of the wiggler, including steering and coherent field errors.
- Evaluate FEL performance for a range of electron pulse lengths and longitudinal profiles.
- Study mirror damage in FEL's and apply this knowledge to our case.
- Prepare an engineering design of the optical cavity.
- Prepare a conceptual design of optical beam transport to the user areas.
- Complete the removal of existing equipment from XA1 and begin conversion to an FEL user facility.
- Complete the architectural and engineering design of the building addition and begin construction.

4. Publications

P.H. Debenham, and B.C. Johnson, "Research Opportunities Below 300 nm at the NBS Free-Electron Laser Facility," 1988 Technical Digest Series Volume 4, Optical Society of America, Washington, DC.

X.K. Maruyama, S. Penner, C.M. Tang and P. Sprangle, "Proposal for a Free Electron Laser Driven by the National Bureau of Standards CW Microtron," Nuclear Instruments and Methods in Physics Research A259, 259-262 (1987), North-Holland, Amsterdam.

S. Penner, R. Ayres, R. Cutler, P. Debenham, B.C. Johnson, E. Lindstrom, D. Mohr, J. Rose, M. Wilson, P. Sprangle and C.M. Tang, "The NBS/NRL Free Electron Laser Facility," to be published in Nuclear Instruments and Methods in Physics Research.

S. Riyopoulos, P. Sprangle, C.M. Tang, and A. Ting, "Reflection Matrix for Optical Resonators in FEL Oscillators," to be published in Nuclear Instruments and Methods in Physics Research.

C.M. Tang, P. Sprangle, S. Penner, and X.K. Maruyama, "Analysis of Free Electron Laser Performance Utilizing the National Bureau of Standards CW Microtron," Proceedings of the 1987 IEEE Particle Accelerator Conference, March 16-19, 1987, Washington, DC, p 205.

5. Talks

S. Penner, "NBS Free Electron Laser Facility," NBS Special Seminar, Gaithersburg, MD, June 15, 1987.

S. Penner, "NBS/NRL Free Electron Laser Facility," Ninth International Free Electron Laser Conference, Williamsburg, VA, September 16, 1987.

S. Penner, "NBS Free Electron Laser Facility," Univ. of MD, College Park, MD, October 23, 1987.

P.H. Debenham, "The NBS Free-Electron Laser Facility," George Washington University, Washington, DC, February 12, 1988.

S. Penner, "NBS Free Electron Laser Facility," JILA, February, 1988.

P.H. Debenham, "Research Opportunities Below 300 nm at the NBS Free-Electron Laser Facility," Topical Meeting on Free-Electron Laser Applications in the Ultraviolet, Cloudcroft, NM, March 2-5, 1988.

M. Wilson, "Beam Performance Expectations from the NBS-Los Alamos Racetrack Microtron," Naval Surface Warfare Center, Silver Spring, MD, March 30, 1988.

References

1. P. Sprangle, R.A. Smith, and V.L. Granatstein, "Free Electron Lasers and Stimulated Scattering from Relativistic Electron Beams," NRL Memorandum Report 3911 (1978).
2. S. Penner et al., IEEE Trans. Nucl. Sci. NS-32, 2669 (1985).
3. M. Wilson et al., Proc. of the 1987 IEEE Particle Accelerator Conference, 322 (1987).

APPENDIX A

NBS-NRL Free-Electron Laser Conceptual Design Report

Injector Modifications

Our goal is to develop an injector with a charge output of 12 pC locked to the 32nd subharmonic of the RF frequency. The desired beam parameters after acceleration in the RTM are ϵ_n (transverse) $< 10 \mu\text{m}$, ϵ (longitudinal) $< 30 \text{ keV degrees}$, peak current 4 A, pulse length 3 ps. Frequencies corresponding to the 8th, 16th, 64th and 128th RF subharmonics are also desirable, consistent with the average power of the RTM klystron. A peak current after acceleration of 2 A is acceptable for FEL performance.

Our baseline design is a Cs_3Sb photocathode excited by a mode-locked frequency-doubled Nd-Yag laser. We hope to make use of the ongoing development program at Los Alamos by Rich Sheffield et al. The Los Alamos staff has expressed a willingness to cooperate with us but a formal collaboration has not been established. The main unknown appears to be photocathode lifetime and reliability.

We recognize that the photocathode concept is in the research and prototyping stage: No working accelerator uses a photocathode injector. A great deal of new information should be available from Los Alamos in the next few months. If the new information is disappointing, the possibility of a thermionic-cathode gun with subharmonic bunching appears to be a viable option.

The existing electron gun geometry is not useable at the required current level because the anode-cathode spacing is too large. Bill Hermansfeldt at SLAC has calculated the performance of a new gun design with reduced anode-cathode spacing. He predicts a normalized emittance of about $2 \mu\text{m}$ at a current of 0.2 A at an operating voltage of 110 keV, which would satisfy all of our requirements. (0.2 A for 60 ps at 110 keV would compress to 4 A for 3 ps

after acceleration.) The space-charge limit of Bill's design is about 2 A at 110 keV.

Calculations must be done with PARMELA to determine if the existing capture section can handle the higher current (by a factor of 40) and higher gun voltage. It may be necessary to add solenoidal focussing (B_z field) over the entire capture section. In the worst case, the capture section might have to be redesigned and replaced. These calculations should be started immediately. These calculations should include different assumed laser intensity profiles and pulse widths on the cathode. Uniform illumination or a gaussian profile may produce quite different performance.

High Peak Current Effects

The existing RTM injector linac produces a beam in which every RF bucket contains the same charge, approximately 0.26 pC. We now want about 50 times as much charge in the micropulse, but with only one RF bucket in 32 filled. To put the problem in proper perspective, several RF linacs have successfully accelerated micropulses of about 10 nC - three orders of magnitude above our goal. What is unique to our situation is that we are dealing with a microtron instead of a one-pass linac, and our emittance and energy spread requirements are very tight. The following list enumerates the known potential effects.

1. Wakefields
2. Intra-beam scattering
3. RF heating
4. Beam loading
5. Beam breakup (BBU)
6. Beam-beam scattering
7. Overlapping micropulses

We now briefly consider these effects in order.

1. Wakefields - The longitudinal wakefield effect produces an uncompensable beam energy spread of about 1% in typical high current S- and L-band linacs. In our case, with a factor of 10^3 less charge but an aperture of a factor of 3 smaller than other S band accelerators, we expect a fractional energy spread of about 10^{-4} . Taking account of the longitudinal optics of the RTM, the result of the wakefield energy loss would be an increase of the longitudinal emittance from an initial value of 20 keV degrees to about 30 keV degrees at 185 MeV. The energy spread and phase spread would each increase by about 20% in the process. A more accurate calculation of both the longitudinal and transverse wakefield effects is needed.
2. Intra-beam scattering - The "Touschek lifetime" of our beam is at least three orders of magnitude longer than the transit time of the beam pulses from injector to FEL, so actual losses should be negligible.¹ Emittance growth due to intra-beam scattering has not been calculated but we expect it to be negligible since in our estimate of Touschek lifetime we actually used the beam energy spread (10 keV) as the energy change which would cause an electron to be lost.
3. RF heating - This effect is due to the high frequency components of the image currents in beam tubes. The effect has been calculated for the parameters of our beam and wiggler vacuum chamber by Kelvin Neil of Lawrence Berkeley National Laboratory. The heating rate is a trivial few milliwatts per meter of chamber length.

¹W. Scharf, "Particle Accelerators and Their Uses," English translation edited by Francis T. Cole, Harwood Academic Publishers, New York (1986), equation 8.25, page 540.

4. Beam loading - This depends primarily on the average current because the quality factor (Q) of the RF structure is very large compared to the subharmonic number of the beam pulses. The single-pulse beam loading is the longitudinal wakefield effect considered above. Beam current fluctuations on a time scale which is slow compared to Q/f but fast compared to the RF system response time (~ 0.1 second due to the mechanically driven power splitters) result in beam energy fluctuations given by

$$\frac{\Delta E}{E} = -\left(\frac{1}{1 + \frac{.037}{N_p I}}\right) \frac{\Delta I}{I}, \quad (1)$$

where N_p is the number of passes of beam in the RTM, and I is the average beam current in amperes. In the worst case ($N_p = 15$, $I = 0.55$ mA), a 1% increase in current causes an 0.18% decrease in energy. This shows the importance of good current stability.

5. BBU - This is also primarily an average current effect. The BBU threshold for the RTM has been estimated to be above 2 mA. However the subharmonic structure has a different Fourier spectrum than a beam with every bucket filled. One of the harmonics of the beam fundamental frequency could be very close to a blowup mode frequency. Then the blowup would be driven by this Fourier component - possibly much larger than the driving term due to noise on a true CW beam. Further calculations should be performed.
6. Beam-beam scattering - The beam micropulses being accelerated from 5 to 17 MeV "collide" with the pulses travelling in the opposite direction. We calculated this effect for the every-bucket-filled case. The net effect was equivalent to a (defocussing) focal length of a

few thousand meters during the 5 to 17 MeV pass (and even weaker at higher energies). Since the sum of the impulses after 32 RF periods depends only on the average current, our first guess is that this is negligible. Further study is recommended (low priority).

7. Overlapping micropulses - When operating at the 32nd subharmonic, a snapshot of the beam pulses in the RTM linac section would show that of every 32 RF buckets there are twenty empty buckets, ten containing one micropulse each, and two containing two micropulses (of different energies) each. The only resulting effect that occurs to us is an increased space charge force, but since this overlapping occurs only at higher energies, it is negligible, except perhaps as a modulation of the wakefield-induced energy spread.

In summary, while none of the high peak current effects appear serious, several should be studied more carefully.

RTM

The DoE-funded RTM development will terminate in April 1988, although the RTM will not be completed at that time. It will be completed with a combination of NBS (STRS) funding and FEL funding. The FEL funding will be used for the completion of the electron beam line through the wiggler.

An outline of the RTM schedule as it relates to the FEL program is as follows:

- December 1987 - begin one pass beam tests (acceleration to 17 MeV)
- March 1988 - complete one pass beam tests, begin installation of recirculation beam lines and extraction line
- November 1988 - begin RTM final beam tests (with existing thermionic-cathode injector system)

April 1989 - complete final beam tests, begin installation of photo-cathode injector system

January 1990 - provide beam to FEL to begin FEL testing

Electron Beam Transport

The physics design of the electron beam transport system for the FEL has been completed. The results are reported in FEL Design Note #4.* The system consists of the following subsystems: (1) the RTM extraction line which places a non-dispersed electron beam on the FEL axis; (2) a four-dipole achromatic chicane to carry the beam around the upstream optical cavity mirror; (3) a two-quadrupole-pair telescope to match the electron beam to the optical mode in the FEL cavity; and (4) a dumping magnet which precedes the downstream cavity mirror, provides the capability of electron beam energy spectrum measurement, and conducts the beam to the beam dump to dispose of it with minimal background radiation. The transport system has a normalized acceptance greater than the 63 μm normalized acceptance of the RTM. Conceptual designs exist for all magnets in the system (8 dipoles and 5 pairs of quadrupoles). Detailed engineering design can start as soon as personnel become available.

FEL Performance Calculations

Three dimensional calculations of single-pass power gain have been performed for radiation wavelengths in the range $\lambda = 0.15 - 12.0 \mu\text{m}$. The electron beam energy range is $\gamma = 50$ to $\gamma = 350$. Calculations were performed for

*FEL Design Notes 1-7 are appended to this report as Appendix A.

normalized emittance $\epsilon_n = 5, 10, \text{ and } 20 \text{ } \mu\text{m}$ and peak currents of $I = 0.5, 2, \text{ and } 4 \text{ A}$. The results for $I = 2 \text{ A}$ are summarized in figure 1. These results are in good agreement with earlier one-dimensional estimates. The calculated gains are nearly independent of emittance so that lasing can probably be achieved down to $\lambda \approx 0.2 \text{ } \mu\text{m}$ even with ϵ_n as poor as $20 \text{ } \mu\text{m}$. Over the entire range of parameters, the gain is nearly linear in beam current. The effect of optical guiding is becoming significant even at $I = 2 \text{ A}$ because of the small emittance. The effects of wiggler field errors, finite pulse length, and beam energy spread have not yet been included in the calculations, although the computer programs that have been developed are capable of including them. The effect of the $< 0.1\%$ energy spread of the RTM beam should be negligible. The main effects of the finite pulse length are expected to be a shortening of the optical output pulse length and a corresponding decrease in energy per pulse and time-averaged power.

Additional calculations are planned for the duration of the project. Some of the topics to be examined are: harmonic yields (of spontaneous coherent light), efficiency enhancement by wiggler tapering, and lasing on the third harmonic.

Wiggler

The wiggler parameters are given in Table I. Since pulse slippage and diffraction effects become serious for $\lambda > 2 \text{ } \mu\text{m}$, we will use the half-length wiggler above this wavelength. After a series of visits and discussions with FEL laboratories and wiggler builders, we have concluded that a wiggler to satisfy our requirements can be obtained commercially via a fixed-price contract.

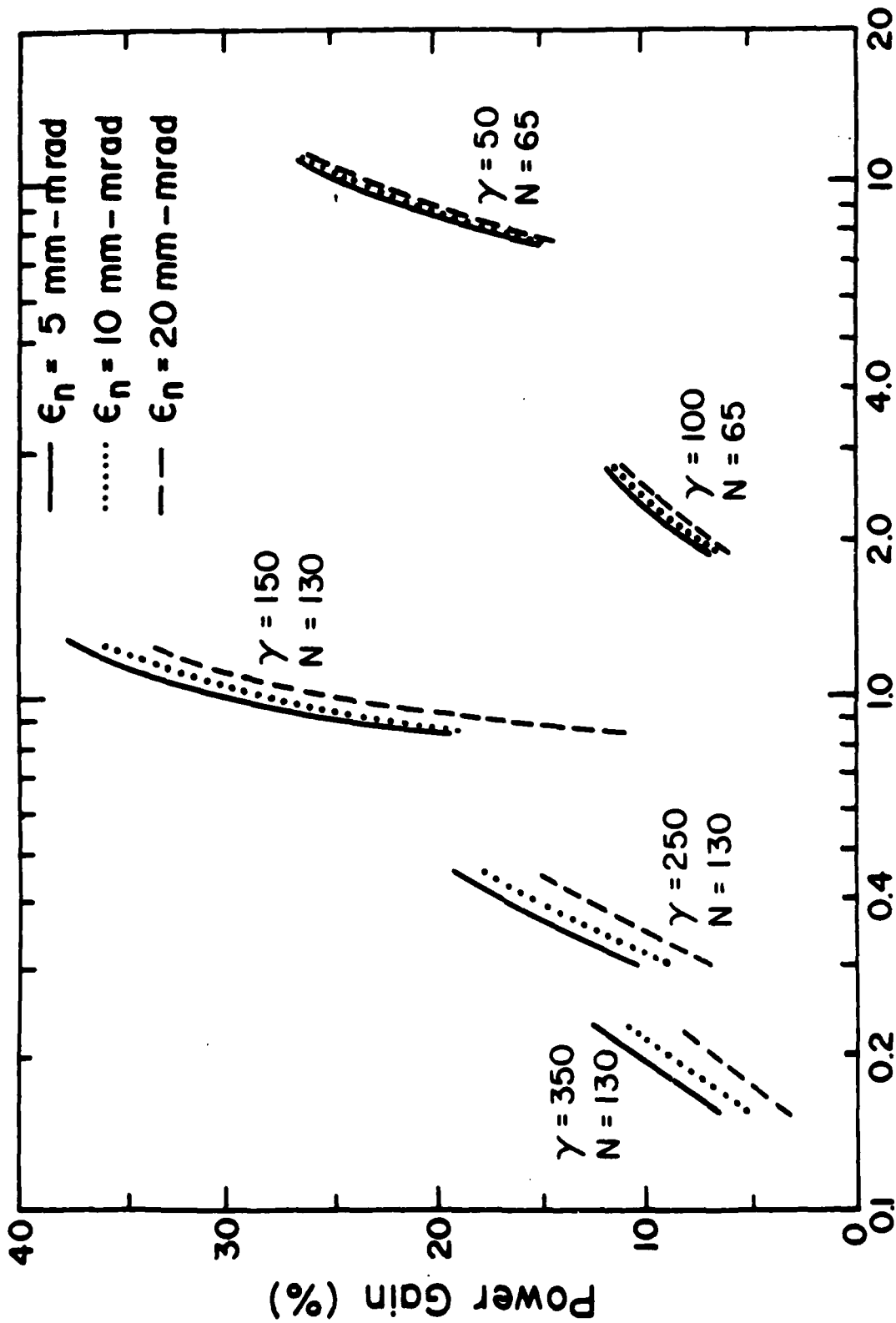


Figure 1 Power gain as a function of radiation wavelength from the 3-D calculations with $l = 2 \text{ A}$.

Table 1 Wiggler Parameters

WIGGLER SPECIFICATIONS	
Wavelength	28 mm
Number of Periods:	Full wiggler 130 + ends Half wiggler 65 + ends
Minimum Gap	10.0 mm
Peak Field at Minimum Gap	>0.54 Tesla
Permanent Magnet Material	(Any) SmCo alloy
Taper:	Adjustable 0 - 0.5 mm/m Independently adjustable, each half
Steering:	Both ends and every 33 periods
Vacuum Chamber:	8.4 x 16 mm ² bore, pairs of ports every 33 periods

WIGGLER TOLERANCES

RMS field error < 27 gauss (0.5% B_0 max)

Integral field errors (both planes)

$$\left| \int_{33 \text{ periods}} Bdz \right| < 23 \text{ gauss cm}$$

Third harmonic amplitude < 0.1 B_0

Transverse field variation < 0.5% B_0 for $|x| < 5$ mm

Optical Cavity

The FEL optical cavity will have a round-trip transit time of 128 RF periods. The distance between cavity mirrors is 8.0616 meters. When the full-length wiggler is used, the cavity configuration is symmetric, so that the radii of curvature of the mirrors are equal. The cavity is asymmetric when the half-length wiggler is used. The baseline design, described in FEL Design Note #6, employs multi-layer dielectric mirrors. The downstream mirror will be partially transmitting (0.5 to 4.0%) for outcoupling. Dielectric mirrors generally have higher reflectivity and damage thresholds than broad-band metal mirrors. Metal mirrors are too lossy to lase in the UV. The disadvantage is that the useful bandwidth of dielectric mirrors is less than 20%, limiting the on-line tunability of the FEL. Several mirrors could be loaded into a changing and aligning mechanism to permit a wider tuning range without breaking vacuum, but this may be cumbersome and would certainly be expensive.

Diffraction losses in the optical cavity have been estimated, using previously-determined vacuum system apertures. The vacuum chamber of the wiggler causes a diffraction loss of 0.6% at 10 μm , which decreases rapidly with decreasing optical wavelength. All other diffraction losses are negligible. The largest mirror size required is < 50 mm diameter for the downstream mirror at $\lambda = 10 \mu\text{m}$. Over most of the operating range, 25 mm diameter mirrors will be adequate.

The output power, fluence, and irradiance have been calculated for the above cavity design in FEL Design Note #6. The calculation uses reflectivity, absorption, and scattering coefficients of commercially available dielectric mirrors. In these calculations, the extraction efficiency is taken to be $(2N)^{-1}$, where N is the number of wiggler periods, which is the theoretical

value for an untapered wiggler. Wiggler magnetic field errors will tend to decrease the efficiency somewhat, whereas tapering the wiggler can increase it dramatically. For the majority of the output spectrum, the outcoupling fraction is chosen, as a function of wavelength, to allow at least a 3% margin between calculated small signal gain (one-dimensional calculation) and total losses. This margin decreases to about 1% for $0.2 \text{ nm} < \lambda < 0.3 \text{ nm}$. Graphs of output power, fluence, and irradiance are give in figures 2 and 3.

The possibility of using an on-axis hole coupler in place of a partially transmitting mirror will be investigated. The desired outcoupling is small enough that a hole coupler would not seriously distort the optical mode in the cavity. It is technically feasible to laser-drill a $50 \text{ }\mu\text{m}$ diameter hole in a $1/4$ " thick quartz substrate. This is about 5% of the mirror spot size of the fundamental ($\lambda = 500 \text{ nm}$). This is the only known outcoupling method for extracting harmonic radiation below about 150 nm .

The possibility of a cavity dumped configuration for FEL operation was discussed briefly. The cavity dumper could consist of an electro-optic "polarization shutter" or an acousto-optic "beam deflector." Rick Freeman pointed out that the acousto-optic method is superior in terms of damage thresholds and wavelength selection, although it may mean that a three-mirror optical cavity is necessary. This area will be investigated further.

The most serious concern in cavity development is mirror damage. Serious damage has been observed at other FELs. Harmonic radiation in the far UV appears to be a major factor. Rick Freeman expressed an interest in collaborating on an experimental program to measure UV damage to our mirrors, using the FEL on the VUV ring at the NSLS facility.

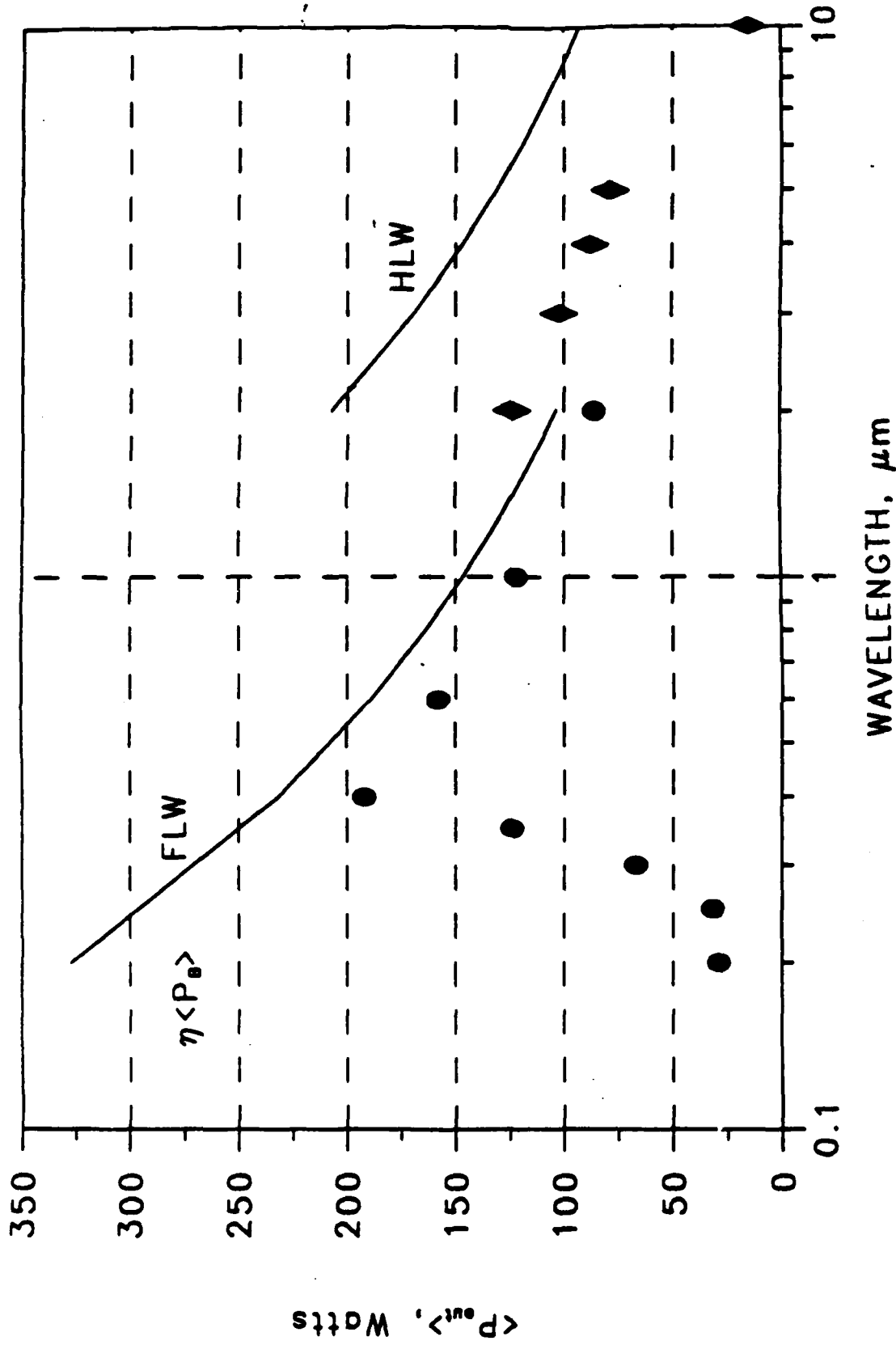


Figure 2 Predicted average output power as a function of wavelength. The solid curves are the upper limit, $\langle P_B \rangle / 2N$, for the case of perfectly reflecting cavity mirrors and no diffraction losses. The circles (for the FLW) and diamonds (for the HLW) are calculated values of output power using the published reflectivities of commercially-available dielectric mirrors, realistic outcoupling fractions (as discussed in the text), and calculated values of D.

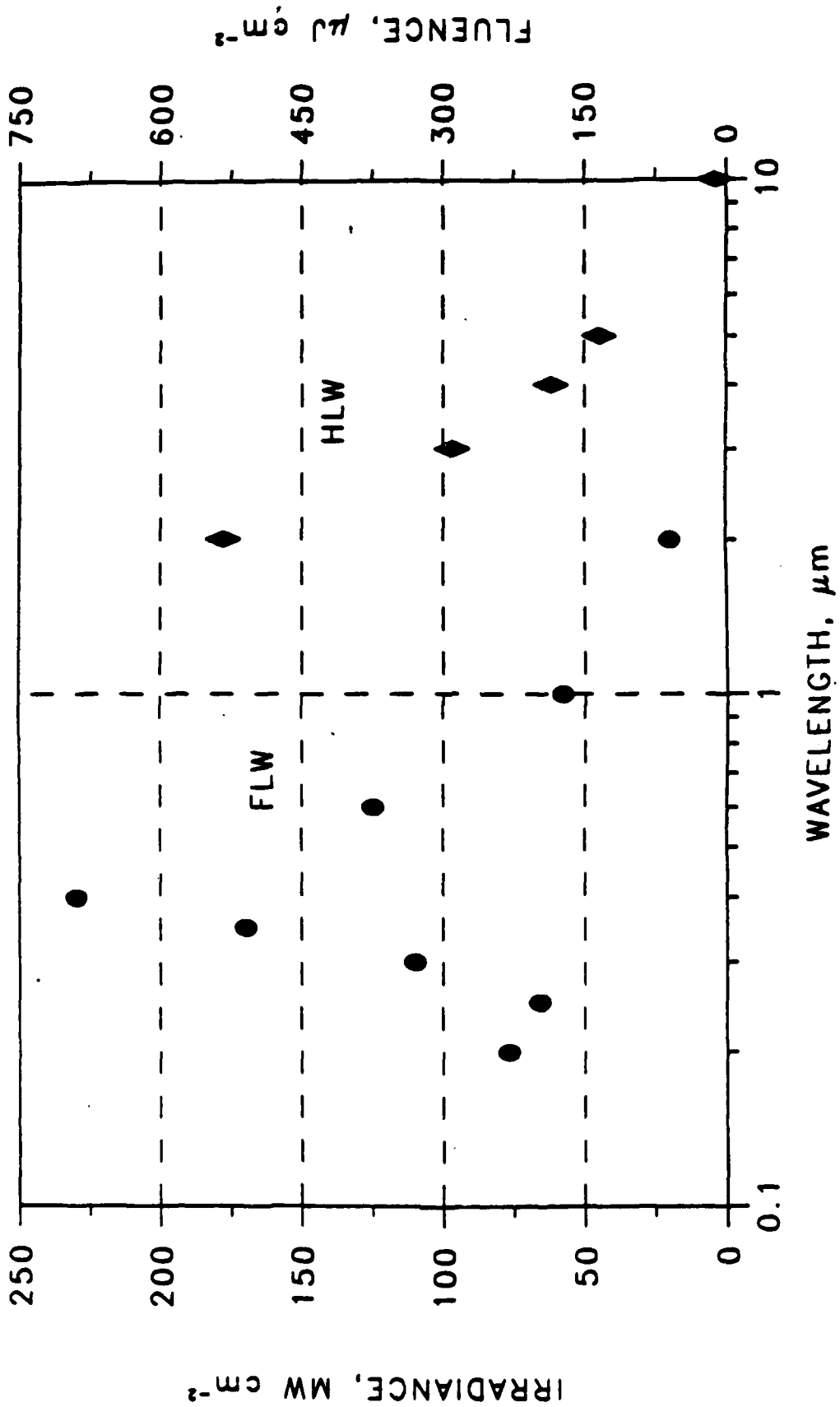


Figure 3 Predicted output fluence per micropulse and peak irradiance as a function of wavelength, corresponding to the average power in figure 2. The mode areas used to obtain these values are the beam 1/e (amplitude) sizes, corrected for the defocussing of the output coupler.

Optical Beam Transport

Design of the optical beam transport system will be deferred until we have better information on user requirements. Because of the long distances involved (up to ~ 100 m), the full power beam will be transported in vacuum. This will also help with the very severe safety concerns due to the high power. A safety protocol will have to be developed.

Optical Diagnostics

A wide variety of optical instrumentation is needed because of the large wavelength interval, high power, and short time structure. A very wide dynamic range in intensities must be covered since we must be able to diagnose the spontaneous emission from the FEL in order to tune up for lasing. For pulse lengths of one picosecond or less, autocorrelation methods appear to be the only available means for temporal measurements.

Electron Beam Diagnostics

Methods for measuring electron beam size profile and emittance are available.² The ability to measure the beam energy distribution will be incorporated in the beam dump magnet. A method for fast temporal measurements is not readily available. Streak cameras have time resolutions of a few picoseconds, which is not adequate for optimizing the peak current. The possibility of using transition radiation interferograms for temporal measurements will be investigated.

²M.A. Wilson, et al., "Performance of the 5 MeV Injector for the NBS-Los Alamos Racetrack Microtron," 1987 IEEE Particle Accelerator Conference, IEEE Catalog 87CH2387-9, (1987) pp 322-324.

Controls

The control system for the FEL will be integrated with the existing RTM controls. Unfortunately, the RTM control system is rapidly approaching its maximum capacity. It is not feasible to add a dedicated secondary station for the FEL. Both hardware and software improvements are needed. In the hardware area, the major change needed is to convert the 8-bit microprocessors to 32-bit. In addition to increasing the processing speed, this will allow us to expand the data base beyond the present limit of 1200 devices. This change would require a complete rewrite of the secondary station software and the redesign and fabrication of all special interface boards, an estimated 3-5 man year effort. A gradual, step-by-step upgrading of the system is planned over several years. This will begin with the purchase of a 32-bit dual processor system for the yet to be constructed primary station wire scanner display subsystem. This 32-bit dual processor system will not only form the wire scanner display system, but has sufficient processing power to permit the replacement of the present control system DEC PDP 11/44 CPU and 8-bit CP/M system. This can be done with a minimum amount of effort (~ 1 man year). Later addition of a third processor to this system would complete the replacement of the existing 8-bit processors in the primary station. This would require a much larger effort (~ 2-3 man years) to recode the existing primary station hardware and replace the primary-to-secondary station link. It is essential that we have a functional system for beam tests in November 1988 and in January 1990.

Building

The existing above ground building that houses the neutron time of flight facility (NTOF) will be modified with a 2000 ft² addition for FEL users. Except for a relatively small office area, the addition will be configured as a single large research hall. Partitions, optical curtains, etc, will be installed to suit user needs. Staff visits to other laboratories will help us plan for user needs. Detailed engineering design of the addition is being carried out by the NBS Plant Division.

APPENDIX B

Design Note 1

Issues Involved in the Choice of
Injector Pulse Frequency and Optical Cavity Length

FEL Design Note #1

Issues Involved in the Choice of Injector Pulse Frequency
and Optical Cavity Length

S. Penner
April 30, 1987

The round trip transit time must be an integral multiple of the RTM RF period. Thus the cavity length L is given by

$$L = N c/2f_0 \quad (1)$$

where $f_0 = 2.38 \times 10^9$ Hz, $C = 2.9979 \times 10^8$ m/s, and N is any integer. For $N = 120$ ($L = 7.558$ m) we have determined that the optical cavity will fit in the available space. It will be difficult to work with a shorter cavity. A somewhat larger cavity is feasible, especially if the cavity mirrors can be asymmetrical with respect to the wiggler center, or if we can reduce the shielding wall (between RTM room and magnet room) to six feet. A longer cavity reduces the heat load on the mirrors, but makes the mirror alignment more difficult. $N = 128$ ($L = 8.062$ m) appears to be feasible.

The injector pulse frequency f_I must be an integral sub-multiple of the RF frequency and an integral multiple of N ; i.e. $f_I = m f_0/N$, where $m = 1, 2, \dots$. We want to be able to operate at $m = 1$, which corresponds to the minimum average beam power, and at the largest m that is compatible with the available electron beam power, $\bar{P} \approx 100$ kW. For our minimum peak current and micropulse length requirements, $I = 2$ A and $\tau = 3$ pS, and design maximum energy, $E = 185$ MeV,

$$\bar{P} = \left(\frac{m}{N}\right) f_0 I \tau E \lesssim 100 \text{ kW.} \quad (2)$$

Thus $\frac{N}{m} \gtrsim 26.4$.

Our original choice was $m(\text{max}) = 5$, with $N = 120$, but it may prove difficult to operate the drive laser for the photocathode at $m = 5$. It may in fact be much easier and operationally convenient to provide $m = 1, 2$, and 4 by acousto-optical techniques applied to the mode-locked drive laser.

The frequency ratio N/m must have excellent phase stability, approximately 1° of f_0 . This may be easier to achieve at some particular values of N/m . Possible choices include, $N/m = 32 = 2^5$ and $N/m = 30 = 5 \times 3 \times 2$. Phase stability depends not only on the choice of N/m but on the choice of the master oscillator frequency, which could be f_0 , using frequency division to obtain f_I ; or f_I , using frequency multiplication to obtain f_0 . Finally, the mode-locked laser frequency should be in the range where commercial instruments are available, roughly $80 - 140$ MHz.

Some numerical possibilities are:

N	$m(\text{max})$	$N/m(\text{max})$	f_I	Other Possible m values
120	5	24	99.167	1 (?)
120	4	30	79.333	1, 2
128	8	16	148.750	1, 2, 4
128	4	32	74.375	1, 2

Our original choice was $m(\max) = 5$, with $N = 120$, but it may prove difficult to operate the drive laser for the photocathode at $m = 5$. It may in fact be much easier and operationally convenient to provide $m = 1, 2$, and 4 by acousto-optical techniques applied to the mode-locked drive laser.

The frequency ratio N/m must have excellent phase stability, approximately 1° of f_0 . This may be easier to achieve at some particular values of N/m . Possible choices include, $N/m = 32 = 2^5$ and $N/m = 30 = 5 \times 3 \times 2$. Phase stability depends not only on the choice of N/m but on the choice of the master oscillator frequency, which could be f_0 , using frequency division to obtain f_I ; or f_I , using frequency multiplication to obtain f_0 . Finally, the mode-locked laser frequency should be in the range where commercial instruments are available, roughly $80 - 140$ MHz.

Some numerical possibilities are:

N	$m(\max)$	$N/m(\max)$	f_I	Other Possible m values
120	5	24	99.167	1 (?)
120	4	30	79.333	1, 2
128	8	16	148.750	1, 2, 4
128	4	32	74.375	1, 2

APPENDIX C

Design Note 2

RTM Shielding Requirements

RTM Shielding Requirements
FEL Design Note #2

S. Penner
May 12, 1987

Because space in the magnet room for the FEL is very limited, the question has been raised if we can reduce the thickness of the shielding wall between the RTM room and the magnet room from 12 ft to 6 ft. The original design of the linac complex called for shielding sufficient to reduce the exposure in occupied areas to less than 2.5 mrem per hour under "worst conditions." Worst conditions were taken to be 100 kW of 110 MeV electrons hitting an unshielded, thick, high-Z target. This turned out to require a shield of 12 ft of concrete, assuming a target-to-exposure-site distance of 24 ft. The calculations are contained in my old data book "Design of Magnet System for Linac," No. 3, March 1 - September 6, 1960, pages 74-83. These old calculations are experimentally verified in the sense that measured neutron fluxes in the linac complex due to shield penetrations are below the predicted level, often by a large factor. One large factor of conservatism is the assumption that the fast neutrons which survive thick shields are isotropic. In fact, they are strongly peaked in the electron beam forward direction. For both background calculations discussed here, the direction of interest is $> 90^\circ$ from the electron beam direction, which should provide a substantial additional decrease in dose.

Now, we are concerned with exposure in the RTM room when the linac is operating. The linac now operates < 1200 hours/year at < 5 kW beam power at energies ≤ 110 MeV. The beam line for neutron time-of-flight work is 36 ft from the nearest occupyable point in the RTM room. My old calculations conclude that the neutron flux through a 6 ft shield due to a 110 MeV electron

beam is 1.8×10^6 neutrons/kw sec. Thus the flux due to 5 kW of beam at 36 ft from the source is 0.6 neutrons/cm² sec = 0.15 mrem/hr. Since the required maximum dose rate for 40 hour/week occupancy remains 2.5 mrem/hr, a 6-ft shield is safe by a factor of 17. In terms of integrated exposure, since the linac operates less than 1200 hours per year, and we cannot expect any individual to be in the area more than 20% of his working time, and the beam loss in the magnet room is $\leq 20\%$ of the total beam power, the expected maximum exposure per year is 7 mrem. This is a factor of ~ 400 below legal limits. We conclude that reducing the shielding wall thickness to 6 ft is completely safe.

We can also calculate the exposure in MR#2, which will be the new "UV Laboratory" due to the 100 kW RTM beam being dumped in the magnet room. The minimum shield thickness is equivalent to 12 ft of concrete (it is actually 4 ft of concrete plus 12 ft of fill dirt), and the source-to-exposure distance is > 24 ft. Assuming 200 MeV operation, the neutron flux is 4.3×10^6 n/kw-sec implying 64 neutrons/cm² sec, equivalent to 160 mrem/hr. The existing beam dump provides a reduction of a factor of ≤ 100 due to the fact that the "target" is water rather than a high-Z material and there is a 4 inch Pb shield built into the dump. This reduces the maximum exposure in one corner of the UV laboratory to 1.6 mrem/hour. It will be necessary to survey the UV lab with the RTM running. Some additional shielding around the beam dump may be needed. (Note that the half-value thickness of Pb for high energy neutrons is about 1.7 inches).

APPENDIX D

Design Note 3

Optical Cavity Length Choice

FEL Design Note #3
Optical Cavity Length Choice

S. Penner, C. Johnson, and P. Debenham
June 19, 1987

Further study of the issues discussed in FEL Design Note #1 have led to the choice of an optical cavity whose round trip length in units of RF wavelengths is $M = 128$, instead of $M = 120$ as stated in the proposal.* The mode-locked laser that drives the photocathode will operate at $n = 32$, i.e., the 32nd subharmonic of the RF frequency, instead of the 24th subharmonic as originally proposed. This choice corresponds to the bottom line of the table in FEL Design Note #1.

Reasons for these choices are:

1. The longer optical cavity, $L = 8.06158$ m, allows a 36 inch working space between the back of the dumping magnet and the downstream cavity mirror. The increased distance is needed for optical diagnostic and alignment equipment, and possibly for outcoupling and/or a device to permit Q-switched operation of the FEL.
2. The longer cavity allows more space around the upstream cavity mirror for the electron beam chicane. In particular, the transverse distance between the optical axis and the electron beam center line, in the plane of mirror, can be increased to 2.97 inches, compared to 1.87 inches in the old design. There is 16.2 inches between the upstream mirror and the position where the transverse distance between the electron beam and the optic axis is 1 inch, so that optical components could be installed in this region as well.

*We have changed notation from Design Note #1, switching from N to M for the optical cavity round trip length, and defining n as the ratio of RF frequency to mode-locked laser frequency.

3. The lower photocathode frequency, 74.375 MHz (instead of 99.167 MHz for $n = 24$), allows a peak current of 2.42 A in a micropulse length of 3 pS at the electron beam design power limit of 100 kW at 185 MeV maximum energy. The older design would have allowed only 1.62 A with all other parameters unchanged. The higher peak current is very important at high energies in order to obtain the gain needed for lasing at short wavelength. We have determined that a mode-locked laser frequency of 74.375 MHz is not a problem.
4. The $m = 4$ design^{*} now used allows for operation of the photocathode with $m = 2$ or 1 by dividing the mode-locked laser frequency by powers of 2. This can be done by electro-optical techniques which maintain good timing stability. The old design was for $m = 5$. The only other synchronous value would have been $m = 1$, but dividing the optical frequency by 5 is difficult. It is very valuable to have the flexibility of micropulse frequency so that the FEL can be turned on and tuned up with reduced electron beam power. Also, if we succeed in obtaining peak beam current higher than 2.4 A, we can reduce the micropulse frequency to stay within the beam power limit. For example, at $m = 2$ (37.1875 MHz micropulse frequency), $I = 4.8$ A in 3 pS pulses at 185 MeV corresponds to 100 kW.
5. Space in the Magnet Room for the longer cavity can be provided by reducing the thickness of the shielding wall between the RTM room and the Magnet Room to 6 ft. FEL Design Note #2 considers the radiation safety consequences of this, and concludes that it is safe.

^{*} m is the number of electron beam micropulses per optical cavity round trip length.

Figure 1 shows the accessible electron beam peak current that can be achieved as a function of electron beam energy for various values of m . The upper energy limit is set by the magnetic field capability of RTM components. The injector limit of 4 A is our design goal for the new photocathode injector. The hyperbolic curves labeled $m = 4, 8, 16$ are imposed by the 100 kW limit on electron beam average power. (Values of $m > 4$ can be obtained by splitting, delaying, and recombining the optical pulses from the mode locked laser.) For $m < 4$, beam power > 100 kW cannot be achieved within the design range of the energy and peak current. For $m > 16$ another potential limit at low energies is due to average current. The 2 mA average current value is a guess of the beam breakup (BBU) limit. Another potential average current limit might be the average power available from the mode-locked laser.

The power limit curves in figure 1 are obtained from the relation

$$I = \frac{M \bar{P}}{m f_0 \tau E} \quad (1)$$

where I is the peak current, \bar{P} the power and E the energy of the electron beam, f_0 is the RF frequency (2380 MHz), and τ is the micropulse length (~ 3 pS). The dependence of peak current on average current, i , is

$$I = \frac{M i}{\tau m f_0} \quad (2)$$

Figure 2 shows the new layout of the upstream optical cavity mirror and the dipole magnets near the mirror. The dipole magnets are made smaller than our previous estimated size by using water-cooled coils, and a picture frame design. There will be a total of 5 magnets of this design: D13 which completes the RTM extraction beam line; D14-D15, located in the RTM room; and

D16-D17, shown in figure 2. The four magnets D14, 15, 16, 17 form an achromatic chicane whose purpose is to deflect the electron beam around the cavity mirror. The smaller transverse dimension of D16 results in a clear line-of-sight along the FEL optic axis.

Figure 3 shows the new layout of the FEL in the magnet room. This layout incorporates the 8 meter optical cavity, the reduced shielding wall thickness and the new design of the achromatic chicane.

CURRENT LIMIT VS. ENERGY

MICROPULSE FREQUENCY = 18.594 m MHz

I, A

INJECTOR LIMIT

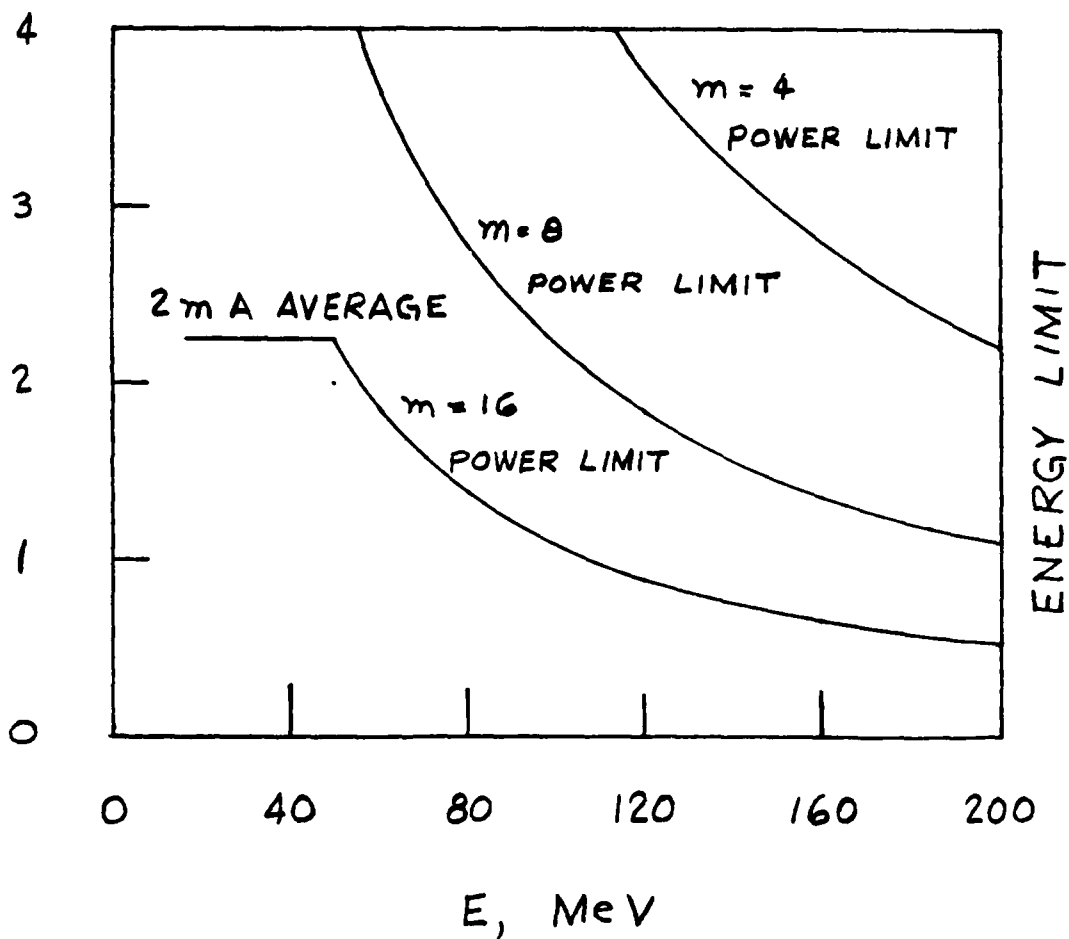
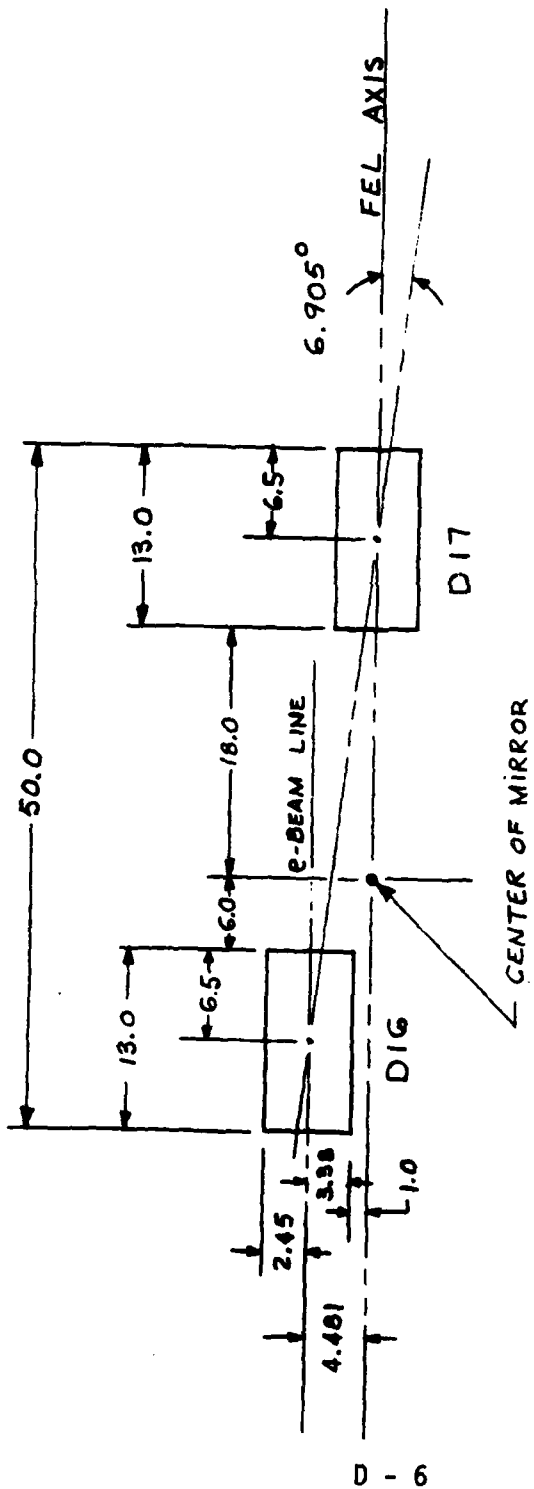


FIGURE # 1

ORIGINAL DATE OF DR	
NO.	S. C. N.
1	
2	
3	
4	



D - 6

PIECE NO.	NATIONAL
	GAITI
	UPSTREAM
FOR	F
MODEL	
DIMENSIONS IN INCH (Unless otherwise specified)	
TOLERANCES (Unless otherwise specified)	
DECIMALS FRACTIONS ANGLES	
DO NOT SCALE THIS P.	
DIV. SEC.	THIS PRINT '85
03	03
	6-16

FIGURE # 2

APPENDIX E

Design Note 4

Electron Beam Transport Design

FEL Design Note #4
Electron Beam Transport Design

S. Penner and E. Lindstrom
July 7, 1987

I. Introduction

This note presents the physical layout and electron beam optics design for the RTM/FEL beam transport system. The function of this system is to transport the beam from the RTM through the FEL wiggler and into the electron beam dump. The system consists of two major sections, the RTM extraction line and the FEL transport section.

The RTM extraction line accepts the beam which is deflected from the RTM by the moveable extraction magnet, D11, and transports it onto the FEL axis. The three major criteria for this beam line are: (1) it must transport the beam through and around a maze of other RTM components (especially the RF drive system), (2) it must function properly at all beam energies, 29-185 MeV, and (3) it must provide an achromatic beam on the FEL axis. A design which meets these criteria is presented in section III of this note.

The FEL transport section operates on the beam which exits the RTM extraction line. The beam must be guided around the FEL upstream optical cavity mirror achromatically, transported through the wiggler with a beam envelope which is concentric with the optical mode shape, and removed to a beam dump, avoiding the downstream optical cavity mirror. In addition to the requirement of operating over the full range of beam energies, this section must function properly over the full range of wiggler field strength, and must provide the diagnostic capability of measuring the electron beam spectrum with and without lasing. The design of the FEL transport section is presented in section IV of this note.

II. Electron Beam Model

In order to calculate beam sizes, aperture requirements, and focusing strengths we need a characterization of the six-dimensional phase space of the electron beam in the RTM. At present, the only available experimental data is the beam emittance measured at 5 MeV.¹ The normalized transverse emittance is 0.56 ± 0.1 mm mrad in the horizontal plane, and 0.70 ± 0.17 mm mrad in the vertical plane. The longitudinal emittance has an upper limit of 5 keV degrees. These are essentially envelope emittances, containing $\geq 95\%$ of the beam current. However, we expect larger emittances from the completed RTM because of (at least) two important effects. First, the high current injector needed for the FEL will have larger emittance than the present injector. Second, the injection transport system from the 5 MeV linac to the RTM has significant chromatic aberrations. For purposes of estimating beam sizes and focal strengths, we will continue to use our design goal emittances of $\epsilon_N = 5$ μm transverse (normalized) and 20 keV degrees longitudinal.

For the purpose of determining the aperture requirements of the system, we must be much more conservative. The limiting aperture of the RTM is the 8 m linac. Its aperture is 5 mm radius. With a 5 MeV injected beam and 12 MeV energy gain in the first pass, the linac acceptance is $\epsilon_{\text{max}} = 63.4$ μm , normalized.² Our design goal for the normalized acceptance, A_N , of the transport system is

$$A_N > \epsilon_{\text{max}} = 63.4 \mu\text{m}, \quad (1)$$

so that the system will never intercept any beam, assuming that there are no significant sources of emittance growth after the first pass through the linac. All beam transport calculations are performed with a beam emittance of $\epsilon_N = 5$ μm , and the acceptance calculated from

$$A_N = \epsilon_N \cdot \text{smallest } (R_A/r_C)^2, \quad (2)$$

where r_c are the calculated beam envelope radii, and R_A the design aperture radii at locations throughout the system in both transverse planes. From equations (1) and (2) the minimum aperture radii required are given by

$$R_{\min} > \sqrt{\frac{\epsilon_{\max}}{\epsilon_N}} \cdot r_c = 3.56 r_c \quad (3)$$

Additional margin above this value is desirable to allow for misalignments and steering errors.

The orientation of the phase ellipsoid at the entrance to the extraction system is needed to calculate beam sizes. The basic optics design of the RTM produces an upright orientation of the phase ellipses at the center of the accelerating section on every pass in all three phase planes. We use this as the starting point of our calculations, with the beam sizes in all four transverse coordinates (x, x', y, y') taken from calculations performed with the (first-order) optics code RTM.OPTICS for transverse tunes of $\mu_x = \mu_y = 45^\circ$ per pass.³ The longitudinal phase ellipse coordinates are taken from STRACE calculations which give $\phi = 1.11$ degrees, $\delta E = 18$ keV for an area of 20 keV degrees.⁴ From this starting point, the following transformations are applied to the beam:

- (1) The transverse beam coordinates are multiplied by $(1 - \frac{6 \text{ MeV/c}}{p})^{1/2}$, where p is the beam momentum at extraction, to account for the transverse optics of the linac.
- (2) The beam matrix is given a transformation which differs from the unit matrix only in the R_{56} element, given by

$$R_{56} = \frac{6 \text{ MeV} \sin 9^\circ}{p} \times \left(\frac{\pi}{180}\right) \times 10^2 \frac{\text{percent}}{\text{degree}}, \quad (4)$$

which accounts for the energy focusing of the linac. (9° is the resonant phase for $\mu_z = 90^\circ$ per pass).

(3) The beam drifts 5.9 meters.

These transformations project the beam to the entrance of end magnet E2. From this point onward, the system is represented by standard TRANSPORT elements.

The origin of floor layout coordinates in the TRANSPORT calculations is the point where the linac axis intersects the effective edge of E1. The Z-axis points north along the linac axis, positive X is to the west, and positive Y is up. The X coordinate of the starting point is adjusted for the closed orbit offset correction of the injection chicane. Except for this correction, the injection chicane and injection quads (Q6-Q7) are ignored. End magnets E1 and E2, the extraction magnet D11, and D8 are explicitly included in all calculations. E1 and E2 are constrained to have no vertical focusing for normal entry and exit by setting their gap height to zero. TRANSPORT calculates the vertical focusing for non-normal entry and exit of E1. All other dipoles have vertical focusing effects appropriate to their gap dimensions and fringe-field type. (We distinguish between pole-tip type and picture frames by the K_1 parameter in TRANSPORT).

Table I gives floor layout coordinates, axis direction angles, magnetic fields and bend angles, for extraction at 29 MeV and 185 MeV.

In the 185 MeV calculations, the return leg quadrupoles are turned off because they have an unrealistic large effect on the dispersion in the beam model used. In actual operation, the dispersion on the linac axis is not zero on every pass because of the return leg quadrupoles. The return leg quadrupoles on the extraction orbit would be adjusted to match the recirculation tune. This would result in a dispersion on the extraction line close to that used in the model with return leg quads turned off, and a converging beam into the extraction line. In our calculations, we have varied Q10-Q11 strengths over a realistic range of values, and determined that achromaticity and

adequately small beam size can be obtained by adjustment of the extraction line quadrupoles. In the 29 MeV case, there is no constraint on the setting of Q10-Q11, and we adjust them in the calculations to obtain the desired beam sizes.

III. RTM Extraction Line

This system transports the beam from the RTM onto the FEL axis. Since we want to accomplish this without resorting to physically moving any magnet other than D11, the layout shown in figure 1 was chosen. The extraction process begins with a deflection of the beam on the appropriate return leg, through approximately 2° . After passing through E1 and D8, the beam has attained enough horizontal displacement to clear D7 on the linac axis. At this point, the beam encounters D12H, which completes the deflection into the extraction channel. Before D12H, the beam axis depends on the extraction energy. After D12H, the beam axis is independent of which return leg D11 is located on. The beam is then deflected vertically by D12V, after which it traverses most of the RTM room at angles $\theta_x = -6.91^\circ$, $\theta_y = 1.88^\circ$ relative to the Z axis. The final extraction line deflecting magnet, D13, is located at the intersection point of this angled beam line with the FEL axis. The FEL axis is parallel to the Z axis at $x = -1.057$ m, $y = 0.254$ m. In order to provide the required bend in both planes, D13 is rotated about the FEL axis by -15.26° from the horizontal plane. As can be seen in figure 1, this beam line passes very close to some RF plumbing components of the RTM. Some adjustment at assembly time may be needed. The location of the FEL axis and the direction of the angled beam can be changed slightly, if necessary. After these calculations were completed, the decision was made to locate the FEL axis 57 inches above the floor instead of 58 inches. This corresponds to $y = 0.229$ m, a change which is small enough to be ignored here.

All bending magnets produce momentum dispersion in the bend plane. The extraction line must be made non-dispersive, i.e., achromatic, so that the beam can be properly transported through the FEL. The principle of the method used to make the extraction line achromatic is illustrated schematically in figure 2. In figure 2, we show a beam line containing two dipole magnets, D12 and D13, which bend through equal angles in opposite directions to produce a parallel-offset beam. The dashed line indicates the trajectory of a particle whose energy is slightly higher than the central trajectory (which is indicated by the long-dash - short-dash line). The high-energy particle would be displaced from the central trajectory by an amount $x = R_{16} \left(\frac{\Delta p}{p} \right)$ after leaving D13. $\frac{\Delta p}{p}$ is the fractional momentum difference between the high energy particle and the central trajectory. If the focusing lenses Q1 and Q2 are turned on, the high-energy particle will follow the trajectory indicated by the solid line in figure 2. It is easy to see that R_{16} will be zero if the distances from the center of D12 to Q1 and the distance from Q2 to the center of D13 are $S/4$, and the focal lengths of Q1 and Q2 are $S/8$. The same transformation will make $R_{26} = 0$, where $x' = R_{26} \left(\frac{\Delta p}{p} \right)$.

In the actual situation, we have dispersion in both planes. Since all vertical dispersion originates at D12V, while there are contributions to the horizontal dispersions from several magnets (D11, E1, D8, and D12H), the dispersion ray is not coplanar with the system axis. This is not really a problem, since the focusing elements are quadrupoles. Thus each thin lens in figure 2 is replaced by a quadrupole doublet in the actual system of figure 1. ($Q_1 + Q12$ and $Q13$, $Q_2 + Q16$ and $Q17$). The system can be made achromatic in both planes simultaneously. This solution is described in table II, which gives quadrupole strengths, beam sizes, and acceptances for both 29 MeV and 185 MeV beams.

The only important shortcoming of this "two quad pair" solution to the achromaticity requirement is that beam sizes, particularly in Q16 - Q17 and D13 are uncomfortably large, especially at low extraction energy. At 29 MeV, the system acceptance is less than the desired value, ϵ_{\max} . The reason for this is easily understood from figure 2. The two-dimensional transfer matrix between D12 and D13 is

$$R_{\text{two quad}} = \begin{bmatrix} 1 & 0 \\ \frac{16}{S} & 1 \end{bmatrix} . \quad (5)$$

With $S = 8$ m determined by the constraints of the extraction geometry, $(R_{\text{two quad}})_{21} = 2$ m/mm, meaning that an input beam size of 1 mm is growing at the rate of 2 mm per meter of path length. This shortcoming can be improved by the insertion of a third quadrupole doublet. A thin lens (QA) inserted at the center of the schematic system of figure 2 has no effect on the dispersion but changes the two dimensional transfer matrix to

$$R_{\text{three quad}} = \begin{bmatrix} +1 & 0 \\ \frac{16}{S} - \frac{1}{f} & +1 \end{bmatrix} . \quad (6)$$

where f is the focal length of QA. In principle, the extraction system from D12 to D13 becomes a unit matrix transformation when $f = S/16$. In practice this is difficult to achieve in both planes simultaneously and requires very strong quadrupoles. In the TRANSPORT solution to the "three quad pair" system, we used the central quadrupole doublet Q14 - Q15 to minimize the vertical beam size at D13 after observing that this was always the limiting aperture of the system. This corresponds to $f = S/8$ in the schematic model,

which reduces R_{21} by a factor of two and provides adequate aperture size everywhere. This solution is described in table III.

We will implement the three-quad pair solution to be certain that the system has the required acceptance. The two-quad pair solution can be used if the design goal emittance is achieved. It will be possible to operate the system in the two-quad pair mode by turning off Q14 - Q15 and changing the settings of the other quadrupoles, since the locations of all components are the same for both solutions. The advantage of the two quad pair solution is simplicity - fewer adjustments to make and elimination of steering corrections due to misalignment of Q14 - 15.

IV. FEL Transport Section

The FEL transport section is shown schematically in figure 3. Dipole magnets D14, 15, 16, and 17 comprise a chicane whose purpose is to transport the electron beam around the upstream optical cavity mirror,⁶ indicated by the large X in figure 3. This chicane is manifestly achromatic. The dump magnet deflects the beam through 90° in front of the downstream optical cavity mirror. Its large dispersion provides the capability of energy spectrum measurement. All bends are in the horizontal plane. The two quadrupole pairs Q18-Q19 and Q20-Q21 form a variable magnification telescope, capable of placing beam waists of adjustable sizes at the wiggler center in both transverse planes. An intermediate waist is formed by the telescope in the chicane region, which tends to minimize the dipole aperture requirement.

FEL gain is maximized by maximizing the overlap of the electron beam with the optical mode in the cavity. The optical mode has a Gaussian transverse intensity profile with root mean square radius at the waist given by

$$\sigma_0 = \sqrt{\frac{z_0 \lambda}{\pi}} \quad , \quad (7)$$

where λ is the optical wavelength and z_0 the "Rayleigh length." The root mean square optical mode size is a function of distance, z , from the waist, given by

$$\sigma(z) = \sigma_0 \sqrt{1 + (z/z_0)^2} \quad . \quad (8)$$

In a low-gain FEL system, the optical waist is placed at the wiggler center and the optimum Rayleigh range is one half of the wiggler length. We maximize overlap with the electron beam by putting its waist at the wiggler center, with a waist size

$$x_0 = \sqrt{\frac{L\epsilon}{2}} \quad , \quad (9)$$

where L is the wiggler length and ϵ the (unnormalized) emittance. The electron beam size at the ends of the wiggler will then be

$$x(L/2) = \sqrt{2} x_0 \quad , \quad (10)$$

while the optical mode radius is

$$\sigma(L/2) = \sqrt{2} \sigma_0 \quad . \quad (11)$$

Note the electron beam will be "inside" the optical mode when

$$\epsilon = \frac{\epsilon_N}{\beta\gamma} < \frac{\lambda}{\pi} \quad . \quad (12)$$

The situation in the y - z plane is more complicated because the planar magnetic wiggler focusses the electrons in the y -direction.⁷ (The wiggle is

in the x z plane.) The y-direction first order transfer matrix of a wiggler segment of length z is

$$R_y = \begin{bmatrix} \cos\left(\frac{z}{\beta_w}\right) & \beta_w \sin\left(\frac{z}{\beta_w}\right) \\ -\frac{1}{\beta_w} \sin\left(\frac{z}{\beta_w}\right) & \cos\left(\frac{z}{\beta_w}\right) \end{bmatrix}, \quad (13)$$

where

$$\beta_w = \frac{\gamma \lambda_w}{2\pi \bar{K}}. \quad (14)$$

λ_w is the wiggler period (28 mm), and

$$\bar{K} = \frac{e B_0 \lambda_w}{2\sqrt{2} \pi m c} \quad (15)$$

is the wiggler parameter averaged over a wiggler period (in MKS units). This result is obtained by averaging over the rapid small amplitude motion at the wiggler period. In the same approximation, all remaining elements of the six dimensional transfer matrix are given by

$$R_{ij} = \delta_{ij}, \quad (16)$$

except $R_{12} = Z$.

In our TRANSPORT calculations we represent the wiggler by four drifts of length $L/4$, plus the parameters of R_y in equation (13), supplied numerically by the "Arbitrary Transformation" (type code 14) input option. We require a vertical waist at the wiggler center with the matched beam size

$$y_0 = \sqrt{\beta_w \epsilon}. \quad (17)$$

The y beam size then remains constant within the wiggler, as can be calculated by application of equation (13).

In table IV we present a summary of magnetic field strengths, beam sizes, and ratios of planned aperture sizes to beam sizes for a 185 MeV electron beam. Four cases are presented: (a) two quad pair extraction system, no wiggler focusing; (b) same input as (a) but with maximum strength wiggler focusing; (c) three quad pair extraction system, no wiggler focusing; and (d) same input as (c) but with wiggler focusing. Table V is constructed like table IV for a 29 MeV beam. Since the cases based on the two quad pair extraction system give acceptances much less than ϵ_{\max} , these cases will probably not be useful.

Table I Extraction Line Layout

A. Magnet location coordinates [(a) 185 MeV, (b) 29 MeV]

	Beam Positions in Meters						Magnet Axis Direction in Degrees		
	Entrance			Exit			θ_x	θ_y	ψ
	x	y	z	y	x	z			
D11	1.2359 (a) 0.1730 (b)	0	0.950	1.2300 (a) -0.1672 (b)	0	0.650	180	0	0
D8	-0.0452 (a) -0.0658 (b)	0	0.275	-0.0508 (a) -0.0695 (b)	0	0.425	0	0	0
D12H	-0.0726 (a) -0.0762 (b)	0	1.050	-0.0959	0	1.3494	-2.000	0	0
D12V	-0.1079	0	1.4486	-0.1440	.0049	1.7465	-6.910	0	90
Q12-Q13	-0.3280	.0551	3.2645	-0.3641	.0650	3.5622	-6.910	1.880	0
Q14-Q15	-0.5806	.1240	5.3482	-0.6166	.1339	5.6458	-6.910	1.880	0
Q16-Q17	-0.8270	.1913	7.3823	-0.8631	.2011	7.6798	-6.910	1.880	0
D13	-1.0388	.2491	9.1301	-1.0570	.2540	9.4299	0	0	-15.260

B. Dipole fields, bend angles (α) and edge angles (β_1, β_2)

	29 MeV				185 MeV			
	B, kg	α	β_1	β_2	B, kg	α	β_1	β_2
E1	9.9831	175.550	-2.225	-2.225	9.9831	175.487°	-2.256°	-2.256
D11	0.1274	2.225°	0	2.225°	0.8121	2.256°	0	2.256°
D8	0.1847	1.613	2.225	-0.612	0.1847	0.257	2.256	-2.000
D12H	0.3603	6.298	1.388	4.910	1.7657	4.911	0	4.911
D12V	0.1077	1.880	0	1.880	0.6767	1.880	0	1.880
D13	0.4090	7.160	7.160	0	2.5711	7.160	7.160	0

Table II Extraction Line with Two Quad Pairs

A. Quadrupole Strengths

Quad	Gradient (gauss/cm)	
	29 MeV	185 MeV
Q10	- 23	0
Q11	22	0
Q12	104	637
Q13	-111	-696
Q16	-113	-705
Q17	116	736

B. Envelope radii (mm)

Location	29 MeV		185 MeV	
	x	y	x	y
D12H-D12V	1.81	2.24	1.15	1.11
Q12-Q13	1.77	5.10	0.82	2.00
Q16-Q17	10.27	8.42	4.13	3.80
D13	2.86	2.90	1.28	1.39

C. Limiting Relative Apertures*

	29 MeV	185 MeV
Aperture/beam size	2.3	5.8
Normalized acceptance, A_N (μm)	26.5	165

*Limit occurs in Q16-Q17 vacuum chamber, assumed physical aperture 47.5 mm diameter

Table III Extraction Line with Three Quad Pairs

A. Quadrupole Strengths

Quad	Gradient (gauss/cm)	
	29 MeV	185 MeV
Q10	- 27	0
Q11	27	0
Q12	147	871
Q13	-135	-780
Q14	106	763
Q15	-121	-909
Q16	84	533
Q17	- 81	-588

B. Envelope radii (mm)

Location	29 MeV		185 MeV	
	x	y	x	y
D12H-D12V	2.23	1.98	1.15	1.11
Q12-Q13	1.15	5.89	0.82	2.32
Q14-Q15	4.19	5.90	2.48	1.53
Q16-Q17	3.28	1.97	1.07	0.42
D13	1.51	2.41	0.93	1.08

C. Limiting Relative Apertures

	29 MeV	185 MeV
Aperture location	Q14-Q15(y)	D13(y)
Assumed aperture size	47.5 mm dia	20 mm
Aperture/beam size	4.0	9.3
Normalized acceptance, A_N (μm)	81.0	430

Table IV FEL Transport Section at 185 MeV

Extraction line focussing type	2 quad pair	2 quad pair	3 quad pair	3 quad pair
Wiggler focussing	None,	Maximum	None	Maximum

A. Quadrupole Strengths (gauss/cm)

Q18	-723	-725	-455	-451
Q19	625	625	472	469
Q20	915	927	637	597
Q21	-526	-549	-591	-490

B. Envelope radii (mm)

Location	x	y	x	y	x	y	x	y
Q18-Q19	5.18	1.93	5.19	1.93	1.98	1.20	1.98	1.20
Chicane	3.35	1.08	3.35	1.04	1.18	0.61	1.18	0.67
Q20-Q21	0.39	0.26	0.38	0.15	0.47	0.29	0.44	0.20
Wiggler	0.226	0.225	0.224	0.143	0.241	0.240	0.240	0.180
Dump Magnet	0.27	0.34	0.27	0.21	0.30	0.38	0.38	0.26

C. Limiting Relative Apertures*

Aperture/beam size	3.6	3.6	10.2	10.1
Normalized acceptance, A_N (μm)	64.1	64.2	518	514

*Limit occurs in D14 vacuum chamber, in the bend plane, assumed physical aperture 24.0 mm

Table V FEL Transport Section at 29 MeV

Extraction line focussing type	2 quad pair	2 quad pair	3 quad pair	3 quad pair
Wiggler focussing	None	Maximum	None	Maximum

A. Quadrupole Strengths (gauss/cm)

Q18	-118	-117	-102	-102
Q19	101	101	91	91
Q20	174	168	109	120
Q21	-138	-167	-108	-147

B. Envelope radii (mm)

Location	x	y	x	y	x	y	x	y
Q18-Q19	12.33	4.05	12.32	4.05	3.95	3.15	3.94	3.15
Chicane	7.98	2.05	7.89	2.15	2.34	1.63	2.27	1.71
Q20-Q21	0.89	0.61	1.13	0.41	0.97	0.54	1.15	0.43
Wiggler	0.435	0.415	0.398	0.143	0.399	0.398	0.398	0.144
Dump Magnet	1.08	1.66	1.10	2.16	1.07	1.36	1.10	2.22

C. Limiting Relative Apertures*

Aperture/beam size	1.5	1.5	5.4	5.3
Normalized acceptance, A_N (μm)	11.3	11.6	145	139

*Limit occurs in D14 vacuum chamber, in the bend plane, assumed physical aperture 24.0 mm

References

1. M.A. Wilson, et al. "Performance of the 5 MeV Injector for the NBS-Los Alamos Racetrack Microtron," Proceedings of the 1987 Particle Accelerator Conference (to be published).
2. See S. Penner "CW Linac book III" data book, pp 1-4 (January 20, 1984).
3. See S. Penner "CW Linac book II" data book, p 18 (April 4, 1980).
4. See S. Penner "CW Linac book III" data book, pp 135-137 (January 23, 1985).
5. K.L. Brown, et al. SLAC-91, Rev 2 (May 1977)
David C. Carey, "New Features in TRANSPORT," TM-1064,2041.000 (Fermilab) September 7, 1981.
6. S. Penner, C. Johnson, and P. Debenham, "Optical Cavity Length Choice," FEL Design Note #3, June 19, 1987
7. S. Penner "RF Linac Based Free Electron Lasers," Proceeding of the 1987 particle Accelerator Conference (to be published).

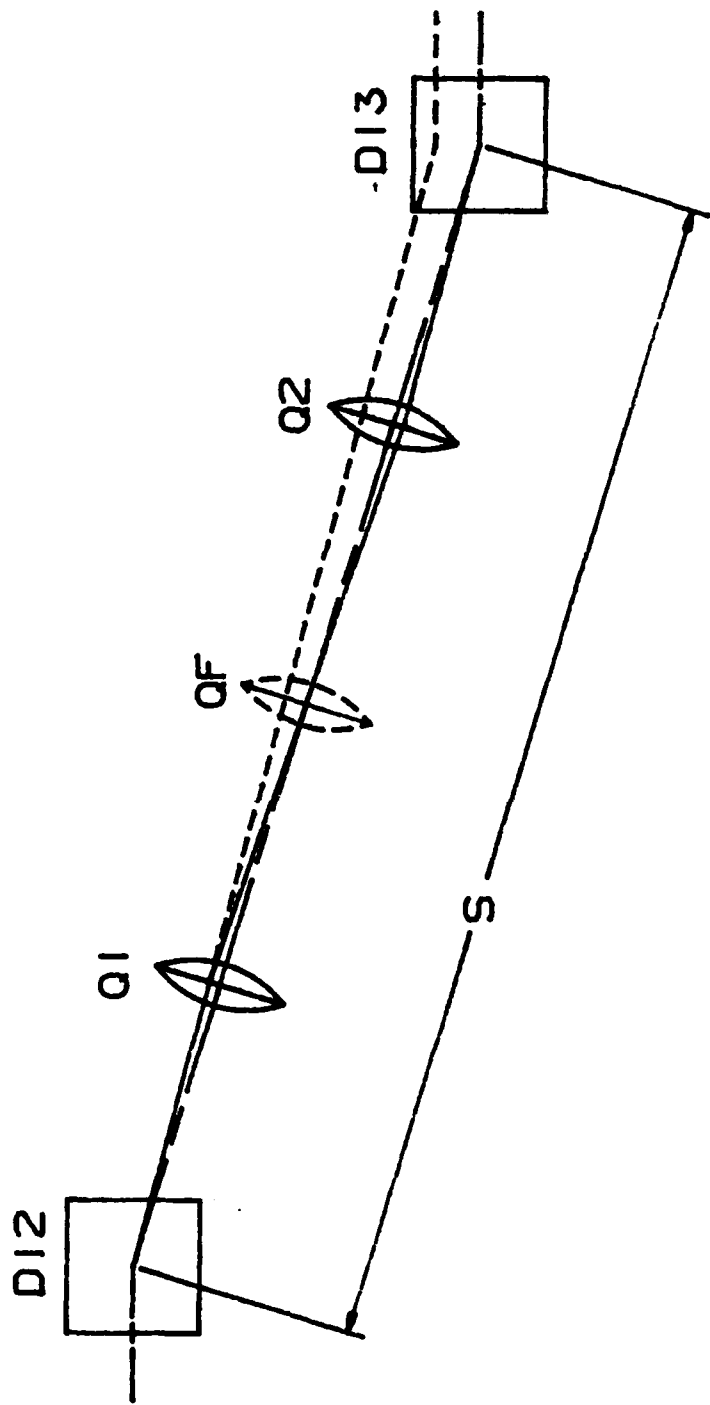


FIGURE 2
Simplified Schematic of Extraction Line

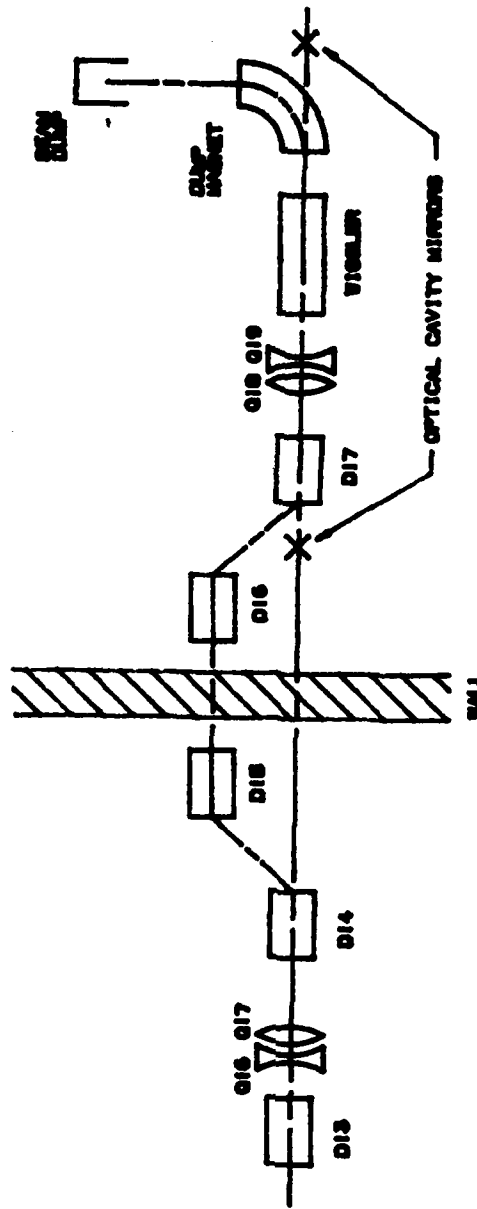


FIGURE 3
FEL Transport System

APPENDIX F

Design Note 5

Predicted FEL Performance at 74.375 MHz

Predicted FEL Performance at 74.375 MHz
FEL Design Note No. 5

P. Debenham, C. Johnson and S. Penner
July 20, 1987

The simplest way to inject electrons into the RTM for FEL operation is to illuminate a photocathode directly with a drive laser. This will provide electron pulses at the drive laser frequency, 74.375 MHz.¹ Because of its simplicity, this mode of operation is especially attractive for initial operation of the FEL. The FEL light output for this case is estimated in what follows.

The small signal power gain of the NBS FEL has been calculated by Tang et al.² for a peak electron beam current, I , of 2A. It is 8% or more over the wavelength range $0.25 \mu\text{m} < \lambda < 10 \mu\text{m}$. Assuming a power reflectivity, R , of 99% for the highly reflective end mirror of the FEL optical cavity, and an unspecified additional power loss, U , of 1% per cavity round trip, we can choose a power outcoupling, C , of 3% to limit the round trip power loss to 6%. This leaves a 2% margin to the gain and ensures that the FEL will lase.

The average output power of the FEL is given by the expression

$$\bar{P}_{out} = \frac{C}{C + 2(1-R) + U} \cdot \frac{\bar{P}_b}{2N}$$

Here, N is the number of periods in the wiggler, and \bar{P}_b is the average power in the electron beam, given by

$$\bar{P}_b (W) = f_i (\text{MHz}) I (A) \tau (\text{ps}) T (\text{MeV}),$$

where f_i , τ and T are the pulse frequency, pulse length and kinetic energy, respectively, of the electron beam. T may be written as

$$T = (\gamma - 1)m_0c^2 = \gamma m_0c^2.$$

The fundamental wavelength, λ , is given by

$$\lambda = \frac{\lambda_w}{2\gamma^2} \left(1 + \frac{K^2}{2} \right),$$

where λ_w is the wiggler wavelength, $K = eB_0\lambda_w/2\pi m_0c$ (in MKS units), and B_0 is the

peak magnetic field in the wiggler. Substituting the above expressions and the following values,

$$\begin{aligned} C &= 0.03 & Z &= 3 \text{ ps} & N &= 130 \text{ for } \lambda < 2 \mu\text{m} \\ U &= 0.01 & \lambda_w &= 2.8 \text{ cm} & N &= 65 \text{ for } \lambda > 2 \mu\text{m} \\ R &= 0.99 & B_0 &= 0.54 \text{ T} & f_1 &= 74.375 \text{ MHz} \\ I &= 2 \text{ A,} \end{aligned}$$

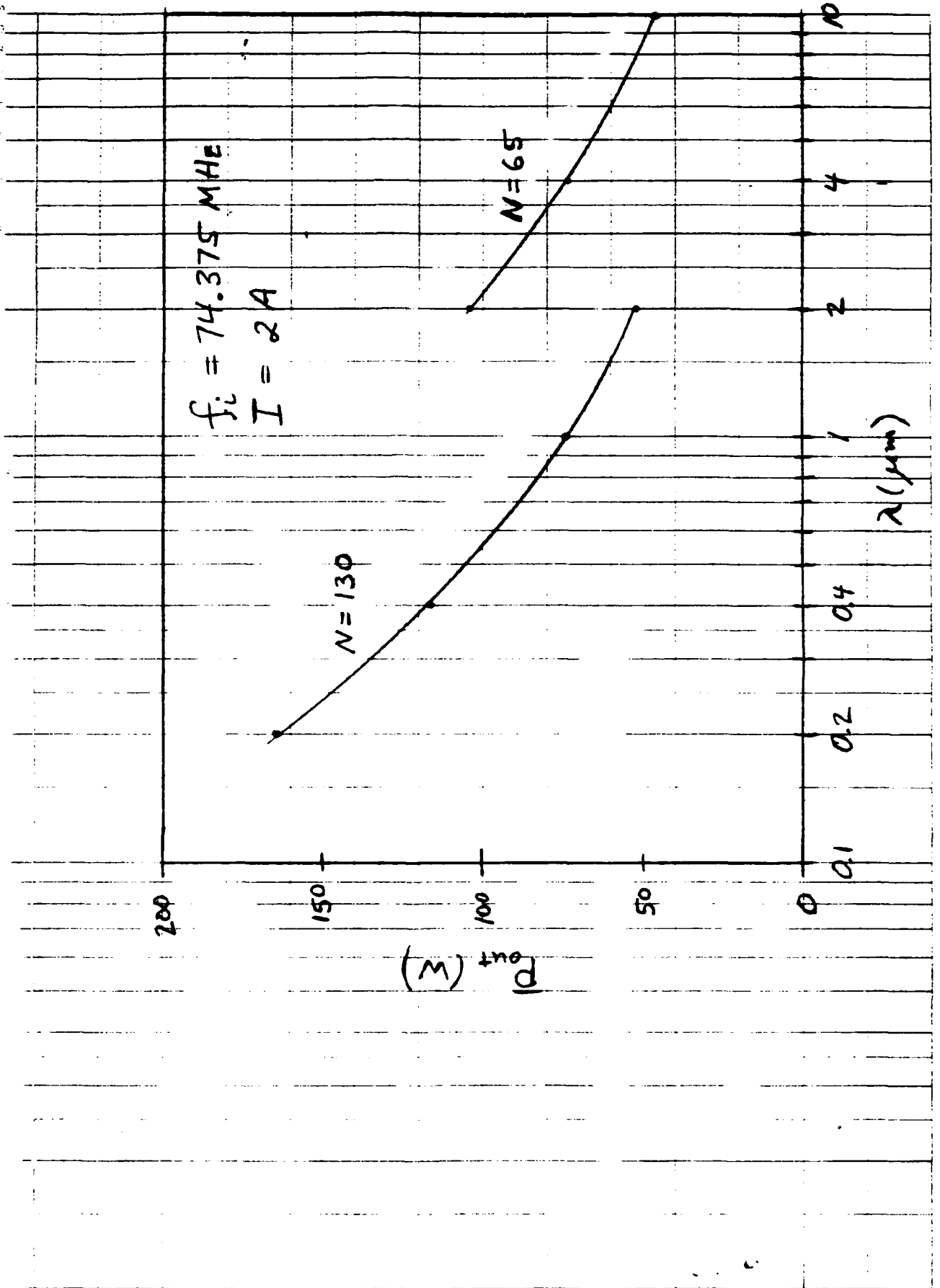
we obtain a formula for the output power as a function of the fundamental wavelength:

$$\begin{aligned} \bar{P}_{\text{out}} (\text{W}) &= 73.3 \lambda^{-0.5} (\mu\text{m}) \text{ for } \lambda < 2 \mu\text{m,} \\ &= 147. \lambda^{-0.5} (\mu\text{m}) \text{ for } \lambda > 2 \mu\text{m.} \end{aligned}$$

As is shown on the accompanying graph, this mode of FEL operation can provide between 45 W and 165 W of radiation over the full wavelength range of $0.25 \mu\text{m}$ to $10 \mu\text{m}$.

References

1. S. Penner, C. Johnson and P. Debenham, "Optical cavity length choice", FEL Design Note #3 (1987), unpublished.
2. C.-M. Tang, P. Sprangle, S. Penner and X. K. Maruyama, "Analysis of free electron laser performance utilizing the National Bureau of Standards cw microtron", to be published in the Proceedings of the 1987 IEEE Particle Accelerator Conference.



APPENDIX G

Design Note 6

FEL Optical Cavity

FEL Design Note 6

FEL Optical Cavity

C. Johnson
September 9, 1987

I. Optical Resonator Geometry

The inverse of the round trip light travel time of the optical resonator is constrained to be a submultiple of the RTM rf frequency, and, in addition, the length must be compatible with the physical dimensions of the wiggler room. The design value is $L = 806.158$ cm. The Rayleigh length, z_0 , of the optical radiation field is equal to half the length of the wiggler, and the optical beam waist is centered in the wiggler. The radii of curvature of the cavity mirrors are constrained by L , z_0 , and the position of the optical waist. The parameters for the optical resonators are summarized in Table 1 for the full and half length wigglers. The upstream mirror, M_2 , is highly-reflecting, and the downstream mirror, M_1 , the output coupler, is partially transmitting. Both mirrors are formed from multi-layer dielectric coatings on polished substrates. The parameter $g_i = 1 - L/R_i$, where $i = 1,2$ is commonly encountered in optical resonator nomenclature; the product g_1g_2 is a measure of the stability of the cavity ($|g_1g_2| < 1$). The distance t is from the cavity waist to M_1 . Note that the optical beam radius, σ_0 , at the waist is given by $\pi\sigma_0^2 = \lambda z_0$. The radius scales as $\frac{\sigma(z)}{\sigma_0} = (1 + \frac{z^2}{z_0^2})^{1/2}$.

Table 1

NBS/NRL FEL Optical Resonators

Parameter	Full Length Wiggler	Half Length Wiggler
Wavelength, cm	2.10^{-5} to 2.10^{-4}	2.10^{-4} to 10^{-3}
Mirror separation, L, cm	806.158	806.158
Rayleigh length, z_0 , cm	182.0	91.0
Cavity waist to M_1 , t, cm	403.079	494.079
Outcoupler radius, R_1 , cm	485.256	510.839
High reflector radius, R_2 , cm	485.256	338.614
Cavity stability g_1	-0.661	-0.578
Parameters g_2	-0.661	-1.381
$g_1 g_2$	0.437	0.798
TEM ₀₀ radius σ_{M_1}/σ_0	2.430	5.521
on mirrors σ_{M_2}/σ_0	2.430	3.572
($1/e^2$) power		
Minimum waist, $\sigma_0(\lambda_{min})$, mm	0.340	0.761
Longitudinal mode spacing, $c/2L = \text{FSR}$, MHz	18.59	18.59

When light is coupled out of an optical cavity through a partially transmitting coating and a substrate with an index of refraction $n(\lambda)$, the substrate acts as a negative lens, so that the Gaussian beam parameters of the emergent TEM₀₀ mode are altered. The beam waist for the emergent mode is located a distance h behind the output coupler and the new Rayleigh length, z_0' , is smaller than z_0 -- the emergent beam is more divergent. The waist location and the Rayleigh length depend weakly on λ through $n(\lambda)$. The substrates, chosen for their resistance to γ and x-radiation, are UV grade fused silica (SiO₂) (Suprasil) for 0.2 μm to 1.0 μm , IR grade fused silica (Optosil) for 1.0 μm to 2.5 μm , and zinc selenide (ZnSe) for 2.5 μm to 10 μm . Representative values for h and z_0' are given in Table 2.

Table 2
Emergent TEM₀₀ Mode

λ , μm	$n(\lambda)$	h , cm	z_0' , cm	Substrate
0.2	1.55051	288.5	84.0	Suprasil
0.3	1.48719	298.8	90.7	Suprasil
0.4	1.46962	301.7	92.7	Suprasil
0.5	1.46252	302.9	93.5	Suprasil
0.6	1.45840	303.6	94.0	Suprasil
0.7	1.45515	304.2	94.4	Suprasil
0.8	1.45330	304.5	94.6	Suprasil
0.9	1.45170	304.8	94.8	Suprasil
1.0	1.45024	305.0	95.0	Optosil
2.0	1.43809	307.2	96.4	Optosil
2.75	2.44	208.2	15.7	ZnSe
5.0	2.43	209.0	15.8	ZnSe
7.5	2.42	209.9	16.0	ZnSe
9.5	2.41	210.7	16.1	ZnSe
11.0	2.40	211.6	16.2	ZnSe

II. Optical Resonator Losses

The source of losses considered here include the outcoupled radiation, absorption and scattering on the cavity mirrors, and diffraction losses. I have designed the cavity such that the apertures of the wiggler vacuum chamber are the limiting factor, with respect to diffraction losses. I ignore distributed losses, such as absorption and scattering in the gain medium. The outcoupled fraction is variable, $T =$ a few percent. The absorption and scattering losses on the mirrors are taken to be $A + S = 1 - R_{HR}$. These losses are between 0.1% and 5% for multi-layer dielectric mirrors. (Typical values for R_{HR} may be found from manufacturer's data.)

Diffraction losses were estimated from published solutions¹ to the integral equations that result from the Fresnel-Kirchhoff formulation of Huygen's

¹H. Kogelnik and T. Li, Proc. IEEE, 54, 1312 (1966), and G.D. Boyd and J.P. Gordon, Bell Sys. Tech. J., 40, 489 (1961).

principle. For the case of square mirrors (or apertures), the field distributions are given approximately by Hermite-Gaussian functions, and for the case of circular mirrors, approximately by Laguerre-Gaussian functions. The losses were calculated only for the TEM_{00} mode. In the case of an asymmetric aperture, the smaller dimension was taken, so these diffraction losses are conservative estimates. Apertures were treated as if they were mirrors with a radius of curvature equal to that of the wavefronts of the optical field at the location of the aperture.

Kogelnik and Li publish solutions for symmetric ($g_1 = g_2$) cavities with circular mirrors for the confocal case ($|g| = 0$) through to the concentric/planar case ($|g| = 1$). Boyd and Gordon publish solutions for square mirrors and symmetric, confocal geometry. We have a symmetric situation for the full length wiggler end mirrors and wiggler vacuum chamber apertures, but otherwise the situation is asymmetric. In all cases the geometry is non-confocal.

Asymmetric resonators were transformed into symmetric resonators with the same diffraction loss using the equivalence principles for spherical mirror resonators:

1. The mirrors can be interchanged;
2. The sign of both of the stability parameters can be reversed, $g_1, g_2 = -g_1, -g_2$;
3. Resonators with the same values for $N, G_1,$ and G_2 are equivalent, where N is the Fresnel number, $N = a_1 a_2 / (\lambda L)$, $G_1 = g_1 a_1 / a_2$, and $G_2 = g_2 a_2 / a_1$.

Here $2a$ is the diameter of a circular mirror or the length of a square mirror. In other words, using principle 3, a resonator with $g_1 \neq g_2$ was transformed into a resonator with $G_1 = G_2$ by varying the ratio of a_1 to a_2 . Then, for

circular mirrors, the diffraction loss per reflection was calculated by using the value of G for g , calculating N , and using Figure 22 in Kogelnik and Li.

For an asymmetric, non-confocal cavity with square mirrors, I estimated the diffraction losses by transforming to a symmetric cavity as before and then assuming that the loss is equal to that of a confocal resonator with the reflector dimensions scaled by the ratio of the spot sizes. This amounts to "derating" the Fresnel number by the factor

$$N^* = N(2L/R - (L/R)^2)^{1/2},$$

and then using Figure 3 in Boyd and Gordon.

The results of the calculations are given in Table 3, which lists the diffraction loss per reflection, D_v , for the significant apertures. The point $z = 0$ corresponds to the waist of the resonator. Note that for efficient operation of the half length wiggler, the vacuum aperture for the dump magnet should be increased to 2.5×2.5 cm.

III. FEL Operating Characteristics

In order to lase, the losses must be smaller than the small signal power gain. By estimating the losses and the small signal power gain, I've determined the lower limit for the wavelength.

I calculated the small signal power gain from

$$G_p = F_1^2 \frac{\pi^2}{\pi \sigma_0^2} \frac{I}{I_A} \frac{\lambda_w^2}{\gamma^3} K^2 N^3 \frac{\partial}{\partial v} \frac{\sin^2 v}{v^2}, \text{ where}$$

$$\frac{\partial}{\partial v} \frac{\sin^2 v}{v^2} = 0.54,$$

Table 3

Diffraction Losses

(a) Full Length Wiggler

Aperture	2a, actual, cm	2a, effective, cm	z, cm	R, cm	λ , μm	N	G	N*	D_v
High Reflector Output Coupler	2.54, circular	2.54, circular	-403.1	-485.3	0.2	100	-0.661	--	0
	2.54, circular	2.54, circular	403.1	485.3	0.6	33	-0.661	--	0
					2.0	10	-0.661	--	0
Wiggler Chamber	0.84 x 1.6, oval	0.84, circular	-198.1	-365.3	0.2	22	-0.085	--	0
	0.84 x 1.6, oval	0.84, circular	198.1	365.3	0.6	7.4	-0.085	--	0
					2.0	2.2	-0.085	--	$5 \times 10^{-4}\%$
D17, in Dump, Output	2.4 x 2.0, rectangular	2.0, square	-355.9	-448.9	0.2	68	-0.540	57	0
	2.4 x 2.0, rectangular	1.8, square	309.9	416.8	0.6	23	-0.540	19	0
					2.0	6.8	-0.540	6	0

(b) Half Length Wiggler

Aperture	2a, actual, cm	2a, effective, cm	z, cm	R, cm	λ , μm	N	G	N*	D_v
High Reflector Output Coupler	2.54, circular	2.54, circular	-312.1	-338.6	2.0	15	-0.90	--	0 $8 \times 10^{-4}\%$
	5.08, circular	3.92, circular	494.1	510.8	5.0	6.2	-0.90	--	$8 \times 10^{-2}\%$
					10.0	3.1	-0.90	--	
Wiggler Chamber	0.84 x 1.6, oval	0.84, circular	-108.5	-184.8	2.0	4.0	-0.11	--	0 $7 \times 10^{-4}\%$
	0.84 x 1.6, oval	0.78, circular	95.0	182.2	5.0	1.6	-0.11	--	0.6%
					10.0	0.81	-0.11	--	
D17, in Dump, Output	2.4 x 2.0, rectangular	1.36, square	-264.9	-296.1	2.0	5.1	-0.85	2.7	$<10^{-4}\%$
	2.4 x 2.0, rectangular	2.00, square	400.9	421.5	5.0	2.0	-0.85	1.1	$3.5 \times 10^{-3}\%$
					10.0	1.0	-0.85	0.54	2.0%
D17, in Dump, Output	2.4 x 2.0, rectangular	1.70, square	-264.9	-296.1	2.0	8.0	-0.85	4.2	0
	2.5 x 2.5, square	2.5, square	400.9	421.5	5.0	3.2	-0.85	1.7	$<10^{-4}\%$
					10.0	1.6	-0.85	0.85	0.2%

B = 5400 Gauss, so that $K = 1.41$, and then $F_1 = 0.824$

$N = 130$ or 65 (full length or half length wiggler),

$\lambda_w = 2.8$ cm

$I = 2$ Amps, and

$\pi\sigma_0^2 = \lambda z_0$.

By substituting for γ^2 from the FEL resonance relation,

$$\lambda = \frac{\lambda_w}{2\gamma^2} \left(1 + \frac{K^2}{2}\right),$$

I get $G_p(\lambda) = 17.09 \sqrt{\lambda}$ full length wiggler

$G_p(\lambda) = 4.272 \sqrt{\lambda}$ half length wiggler,

where λ is in cm. This formula for the small signal power gain is based on the 1-D calculations and with a conservative estimate for the filling factor (the overlap between the electron and optical spatial modes inside the wiggler). C.M. Tang has revised the estimation for the small signal gain to include several 3-D effects, and a more realistic estimation for the filling factor. The overall result is about the same values for G_p as what I have used.

According to the engineers at Acton Research, it is not possible to construct multilayer dielectric coatings for wavelengths below 146 nm. Typical reflectivities, taken from the Acton Research catalog, at 146 nm are $R_{HR} = 0.94 \pm 0.02$. At 2 Amps peak current, we'll have $G_p(146 \text{ nm}) \cong 6.5\%$, which requires $R_{HR} > 0.97$ (see below). Below 146 nm, metallic coatings are used, with typical reflectivities of 0.70 to 0.90. Therefore, without an improvement in the small signal power gain (or better mirrors), lasing below 146 nm will not be possible with the NBS/FEL. Note that below 200 nm, we would have to change to MgF_2 or LiF for all of the transmissive optics. Below 110 nm,

no material transmits, and this defines the start of the "extreme ultraviolet," or EUV, region.

After lasing begins, the FEL will saturate. The output no longer depends on the small signal power gain. In theory, the average power increase per round trip is $\bar{P}_b/2N$, where \bar{P}_b is the average power in the electron beam. The beam power is determined by the kinetic energy of the electrons, the peak current, the pulse width, and the frequency:

$$\bar{P}_b(\lambda) = f_j \cdot I \cdot \Delta t (\gamma m_0 c^2) \text{ Watts, or}$$

$$\bar{P}_b(\lambda)/2N = 1.465/\sqrt{\lambda} \text{ Watts (full length wiggler)}$$

$$= 2.931/\sqrt{\lambda} \text{ Watts (half length wiggler),}$$

where λ is in cm and I've used the FEL resonance relationship to eliminate γ .

For the saturated FEL, it is straightforward to calculate the average intracavity and output power in terms of $\bar{P}_b(\lambda)$. After one complete round trip, the power in the optical field must be the same, i.e., the fractional increase in average power, $\bar{P}_b/(2N\bar{P}_{cav})$, is equal to the sum of the fractional losses -- here diffraction at the vacuum apertures (D_v) and cavity mirrors (D_m), absorption and scattering losses on the mirrors, and transmission loss (the output power). The average normalized, intracavity power on the output coupler is

$$\frac{\bar{P}_{cav,oc}}{\bar{P}_b/2N} \equiv \epsilon = \frac{(1 - D_v)}{1 - R_{HR} R_{OC} (1 - D_v)^4 (1 - D_m)^2}$$

The average, normalized output power is

$$\frac{\bar{P}_{out}}{\bar{P}_b/2N} = \frac{(1 - D_m)(1 - D_v)T}{1 - R_{HR} R_{OC} (1 - D_v)^4 (1 - D_m)^2} = \epsilon T.$$

At the beginning of the wiggler, the average, normalized intracavity power is

$$\frac{\bar{P}_{cav}}{\bar{P}_b/2N} = \frac{R_{eff}^2}{1 - R_{eff}^2}, \text{ where } R_{eff}^2 = R_{oc} R_{HR} (1 - D_v)^4 (1 - D_m)^2.$$

The condition that the small signal fractional power gain must exceed the fractional losses can now be made quantitative:

$$G_p > \frac{1 - R_{eff}^2}{R_{eff}^2} \equiv \frac{1}{\epsilon_{min}}$$

The higher R_{HR} is, the easier it will be to achieve saturation, the larger T can be, and the more efficient the FEL will be. For higher values of G_p , the minimum value of R_{HR} decreases, i.e., $R_{HR} > 0.90$ at $2 \mu\text{m}$ for the full length wiggler, where $G_p = 24\%$. If absorption and scattering losses are small at this wavelength, say, 0.1% , then T could be as large as 19% .

Efficient laser operation requires low losses. However, if the losses (including T) are made small enough, the intracavity power will reach levels that are capable of mirror damage. Therefore, we must consider damage thresholds of the multilayer dielectric coatings when choosing the appropriate values for R_{HR} and T . The average irradiance (W cm^{-2}) and peak fluence (J cm^{-2}) are the important quantities, so we must calculate the effective area of the radiation on the cavity mirrors. The area is $\pi\sigma_M^2 = \pi\sigma_0^2 \left(\frac{\sigma_M}{\sigma_0}\right)^2$, where $\frac{\sigma_M}{\sigma_0} = 2.43$ (full length wiggler) and $\frac{\sigma_M}{\sigma_0} = 3.57$ (half length wiggler)* (see Table 1). The average intracavity irradiance and peak intracavity fluence on the output coupler can be put in terms of the FEL wavelength using the expression for $\bar{P}_b(\lambda)/2N$:

*This is a conservative estimate, because I've used σ_m/σ_0 for the high reflector.

$$\bar{I}_{oc} = \frac{\epsilon \bar{P}_b}{2N} \cdot \frac{1}{\lambda z_0} \left(\frac{\sigma_0}{\sigma_M} \right)^2, \text{ W cm}^{-2}$$

$$F_{oc} = \frac{\langle I \rangle}{f_i} \text{ J cm}^{-2}.$$

Numerically,

$$\bar{I}_{oc} = \frac{\epsilon}{734 \cdot \lambda^{3/2}} \text{ W cm}^{-2} \quad \epsilon \geq \epsilon_{min} \quad \frac{7.98 \cdot 10^{-5}}{\lambda^2} \text{ W cm}^{-2},$$

$$F_{oc} = \frac{\epsilon \cdot 1.83 \cdot 10^{-11}}{\lambda^{3/2}} \text{ J cm}^{-2} \quad \epsilon \geq \epsilon_{min} \quad \frac{1.07 \cdot 10^{-12}}{\lambda^2} \text{ J cm}^{-2},$$

for the full length wiggler, and

$$\bar{I} = \frac{\epsilon}{396 \cdot \lambda^{3/2}} \text{ W cm}^{-2} \quad \epsilon \geq \epsilon_{min} \quad \frac{5.915 \cdot 10^{-4}}{\lambda^2} \text{ W cm}^{-2},$$

$$F_{oc} = \frac{\epsilon \cdot 3.39 \cdot 10^{-11}}{\lambda^{3/2}} \text{ J cm}^{-2} \quad \epsilon \geq \epsilon_{min} \quad \frac{7.94 \cdot 10^{-12}}{\lambda^2} \text{ J cm}^{-2},$$

for the half length wiggler. As before, the wavelength is in cm. The minimum intracavity average irradiance on the output coupler is plotted in Figure 1 (solid line), along with observed cw damage thresholds for high power, multi-layer dielectric, laser mirrors (dashed line), overcoated silver (dash-dot line), and overcoated aluminum (dotted line). If we regard the FEL as a cw laser, then these metallic coatings are too fragile for our use, because they are destroyed before the laser saturates. The individual points represent calculated solutions.

Damage thresholds for pulsed laser radiation are generally quoted for 10 ns wide pulses at 10 Hz repetition rate at 1.06 μm . To derate for our short pulse, I fitted observed breakdown fluences (see Melles Griot Optics Guide 3) at several pulse widths to the form $F_{BD} = t^n$ to find $F_{BD} = 1.6 \cdot 10^6 t^{0.56} \text{ J cm}^{-2}$, or $F_{BD} = 0.6 \text{ J cm}^{-2}$ for 3 ps wide pulses. The observed data were for near-IR wavelengths; standard practice is to derate by a factor of 5 for the

UV and by a factor of 2 for the visible. The minimum intracavity fluence on the output coupler is plotted in Figure 2, along with the estimated damage thresholds for high power laser mirrors with 3 ps wide pulses, and the calculated solutions.

With an idea of permissible build-up ratios, typical reflectivities, and diffraction losses, we can estimate the output power. Note that to convert to output irradiance or fluence, the correct area is $\lambda z'_0$ (see Table 2). The results are summarized in Table 4 and in Figures 3, 4, and 5. In all cases, the pulse width is 3 ps and the repetition rate is 74.375 MHz. The average diffraction losses are given by \bar{D} , where $\bar{D} \equiv 1 - (1 - D_v)^2(1 - D_m)$. The efficiency is defined for the overall process, taken to be the product of the RTM, wiggler, and optical cavity efficiencies: $\text{Efficiency} \equiv \frac{0.08 \cdot \epsilon T}{2N}$. The parameter $\theta_{1/2}$ is the half-angle of the divergence of the optical TEM₀₀ mode: $\theta_{1/2} = \tan \sigma'_0/z'_0 \approx \sigma'_0/z'_0 = \lambda/\pi\sigma'_0$.

In addition to the output power and spatial mode characteristics, there are a number of other important parameters. The output is linearly polarized. The spectral bandwidth is expected to be Fourier-transform limited, so that the bandwidth depends on the pulse width and shape: for pulses with a Gaussian temporal distribution with a FWHM of 3 ps, the spectral bandwidth is about 200 GHz, or 7 cm^{-1} , or 1.7 \AA at 500 nm. This bandwidth corresponds to about 10^4 longitudinal modes of the 8.06 m-long oscillator. If the pulse width is 3 ps over the entire wavelength range, then the resolution, $\Delta\lambda/\lambda$, is the smallest in the UV. It should be possible to compress the pulse width to about 100 fs.

The tuning range of standard high-power, multi-layer dielectric, laser mirrors is about $\pm 12\%$; so-called broad band multi-layer dielectric reflectors

Table 4

FEL Operating Parameters

λ μm	ϵ_{min}	RHR	T	D	ϵ	ϵT	P_{cav} KW	$I_{\text{cav,oc}}$ GW cm^{-2}	P_{out} W	P_{out} KW	E_{out} μJ	I_{out} MW cm^{-2}	Efficiency (total)	σ'_0 mm	$\theta_{1/2}$
0.20	13	0.975	0.005	0	18.4	0.09	5.7	1.26	29	130	0.39	77	$2.8 \cdot 10^{-5}$	0.23	0.27
0.25	12	0.980	0.005	0	22.5	0.11	6.4	1.10	32	140	0.42	66	$3.4 \cdot 10^{-5}$	0.26	0.30
0.30	11	0.985	0.010	0	25.2	0.25	6.5	0.94	67	300	0.90	110	$7.7 \cdot 10^{-5}$	0.29	0.32
0.35	10	0.995	0.010	0	50.2	0.50	12.2	1.48	124	560	1.7	170	$1.5 \cdot 10^{-4}$	0.32	0.35
0.35	10	0.995	0.030	0	25.1	0.75	6.0	0.75	186	830	2.5	260	$2.3 \cdot 10^{-4}$	0.32	0.35
0.40	9	0.999	0.010	0	83.4	0.83	19.1	2.01	192	860	2.6	230	$2.6 \cdot 10^{-4}$	0.34	0.37
0.40	9	0.999	0.040	0	23.8	0.96	5.5	0.57	222	990	3.0	270	$3.0 \cdot 10^{-4}$	0.34	0.37
2.00	4.1	0.999	0.010	$5 \cdot 10^{-6}$	83.3	0.83	8.5	0.18	86	380	1.1	20	$2.6 \cdot 10^{-4}$	0.78	0.81
2.00	4.1	0.999	0.040	$5 \cdot 10^{-6}$	23.8	0.96	2.4	0.05	99	440	1.3	23	$3.0 \cdot 10^{-4}$	0.78	0.81
2.00	17	0.990	0.010	0	33.6	0.33	6.7	0.13	68	300	0.90	96	$2.0 \cdot 10^{-4}$	0.32	0.81
2.00	17	0.990	0.030	0	20.2	0.60	4.0	0.08	124	560	1.7	178	$3.7 \cdot 10^{-4}$	0.32	0.81
4.00	12	0.990	0.010	0	33.6	0.33	4.7	0.05	48	220	0.66	35	$2.0 \cdot 10^{-4}$	0.45	2.8
4.00	12	0.990	0.030	0	20.2	0.60	2.8	0.03	88	390	1.2	62	$3.7 \cdot 10^{-4}$	0.45	2.8
5.00	10	0.990	0.010	$2.4 \cdot 10^{-5}$	33.5	0.33	4.3	0.03	43	190	0.57	24	$2.0 \cdot 10^{-4}$	0.50	3.2
5.00	10	0.990	0.030	$2.4 \cdot 10^{-5}$	20.1	0.60	2.6	0.02	79	350	1.0	45	$3.7 \cdot 10^{-4}$	0.50	3.2
10.00	7.4	0.990	0.005	$1.7 \cdot 10^{-2}$	17.4	0.09	1.5	0.006	8	36	0.11	2.2	$5.4 \cdot 10^{-5}$	0.72	4.5
10.00	7.4	0.990	0.010	$1.7 \cdot 10^{-2}$	16.0	0.16	1.4	0.006	15	66	0.20	4.1	$1.0 \cdot 10^{-4}$	0.72	4.5

are about a factor of two broader -- this corresponds to a bandwidth of 200-250 nm in the visible. Hence, in order to oscillate in the fundamental from 0.2 μm to 10 μm , many mirrors will be needed. However, it is important to realize that the FEL will be flexible without changing mirrors -- the FEL output can be used to generate harmonics from second-harmonic generation and/or mixing in nonlinear crystals, four wave mixing in gases, and Raman shifting in H_2 . In addition, the FEL will have sufficient power to pump a number of tunable lasers, i.e. organic dye lasers for the near-UV to near IR, and color-center or FIR lasers in the infrared. It may be possible to synchronously pump a dye laser in order to generate femtosecond pulses.

IV. Cavity Modifications

There are several disadvantages to the use of partially transmitting/partially reflecting multi-layer dielectric coatings for the output coupler. The bandwidth may be narrower than that of the high reflector, T is variable by as much as 50% for some coatings, and to change T one must change the mirror. A possible alternative to this cavity would consist of two highly reflecting end mirrors and an intracavity, variable output coupler, for example an electrooptic modulator and a polarization beamsplitter. If the E/O crystal were cut to act like a half-wave plate at zero applied voltage, then the output would vary as $\sin^2\Gamma$, where Γ is small and proportional to the applied voltage. The disadvantage to this scheme is that the E/O crystal and polarization beamsplitter must be anti-reflection (AR) coated to minimize losses, and these coatings also have limited bandwidth. If the voltage was switched rapidly, so that Γ changed from 0 to $\pm \pi/2$, then the E/O modulator could be used as a cavity dumper.

An alternative method of cavity dumping involves acousto-optic modulation. Basically, a pulse of rf voltage is applied to a transducer that is mounted on a piece of optical quality quartz. Acoustic waves are generated, and it is possible to deflect an optical beam off the diffraction grating set up by the acoustic waves. The A/O cavity-dumper is superior to the E/O modulator because the quartz can be cut at Brewster's angle, thus eliminating the need for AR coatings, and therefore extending the tuning range. For efficient use of the A/O beam deflector, it is necessary to have an optical waist in the quartz, so that a three mirror FEL optical cavity might be necessary. Acousto-optic cavity dumpers can be used as output couplers in conventional lasers. An application involving a dye laser is shown in Figure 6.

FIGURE 1
 AVERAGE INTRACAVITY IRRADIANCE ON THE OUTPUT COUPLER
 AS A FUNCTION OF WAVELENGTH

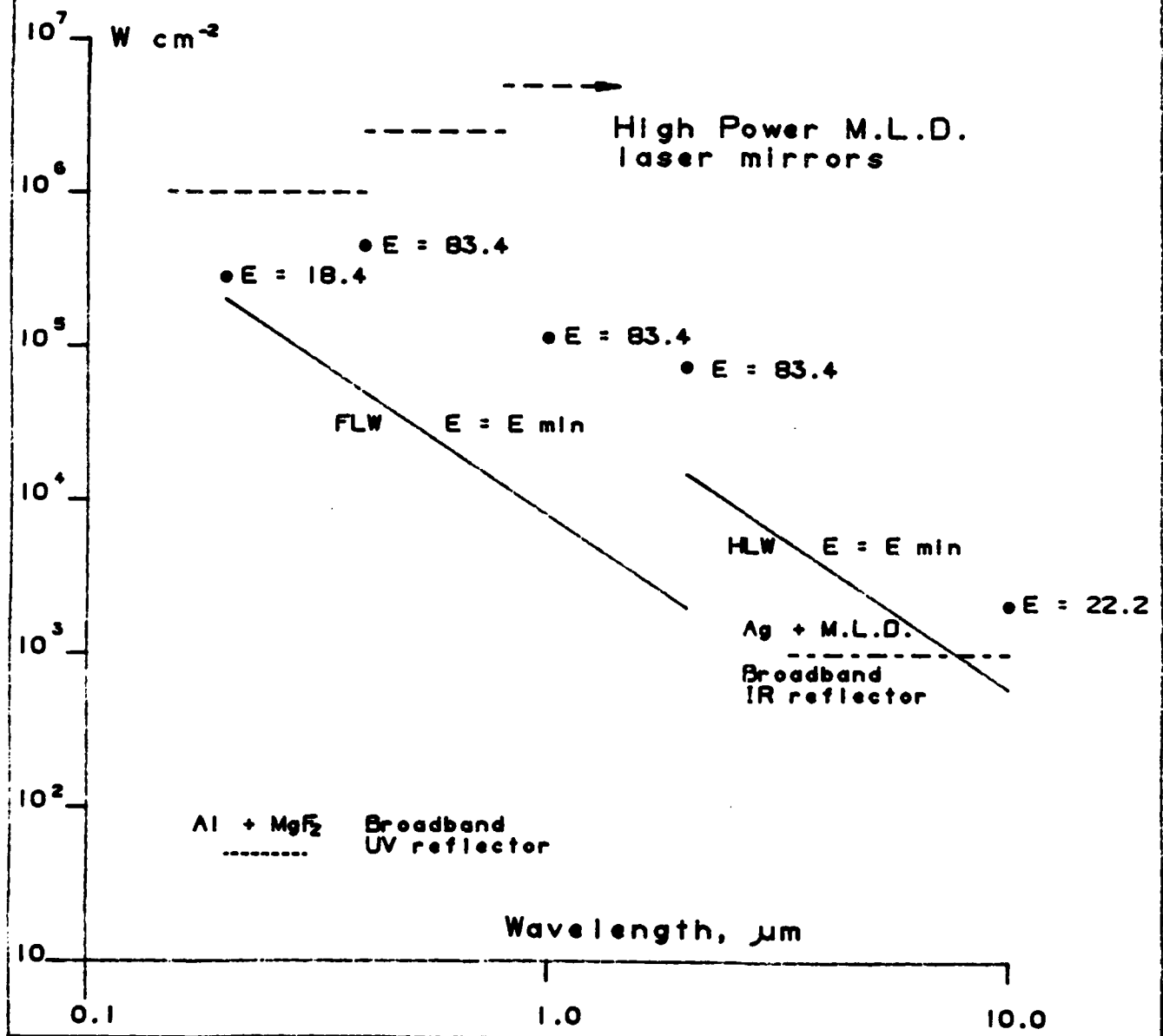


FIGURE 2
 PEAK INTRACAVITY FLUENCE ON THE OUTPUT COUPLER
 AS A FUNCTION OF WAVELENGTH. (3ps - WIDE PULSE)

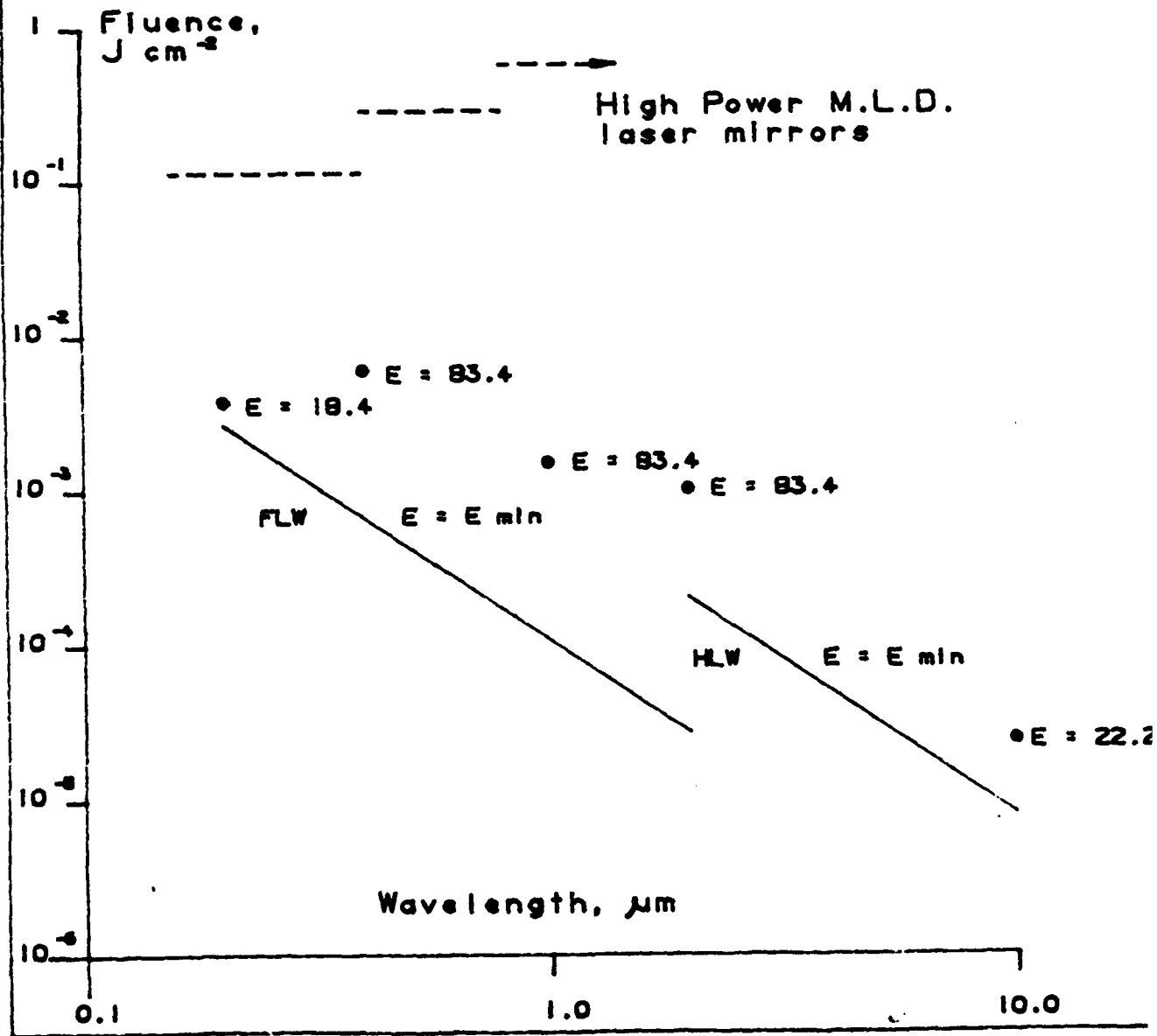


FIGURE 3
 AVERAGE OUTPUT POWER, WATTS

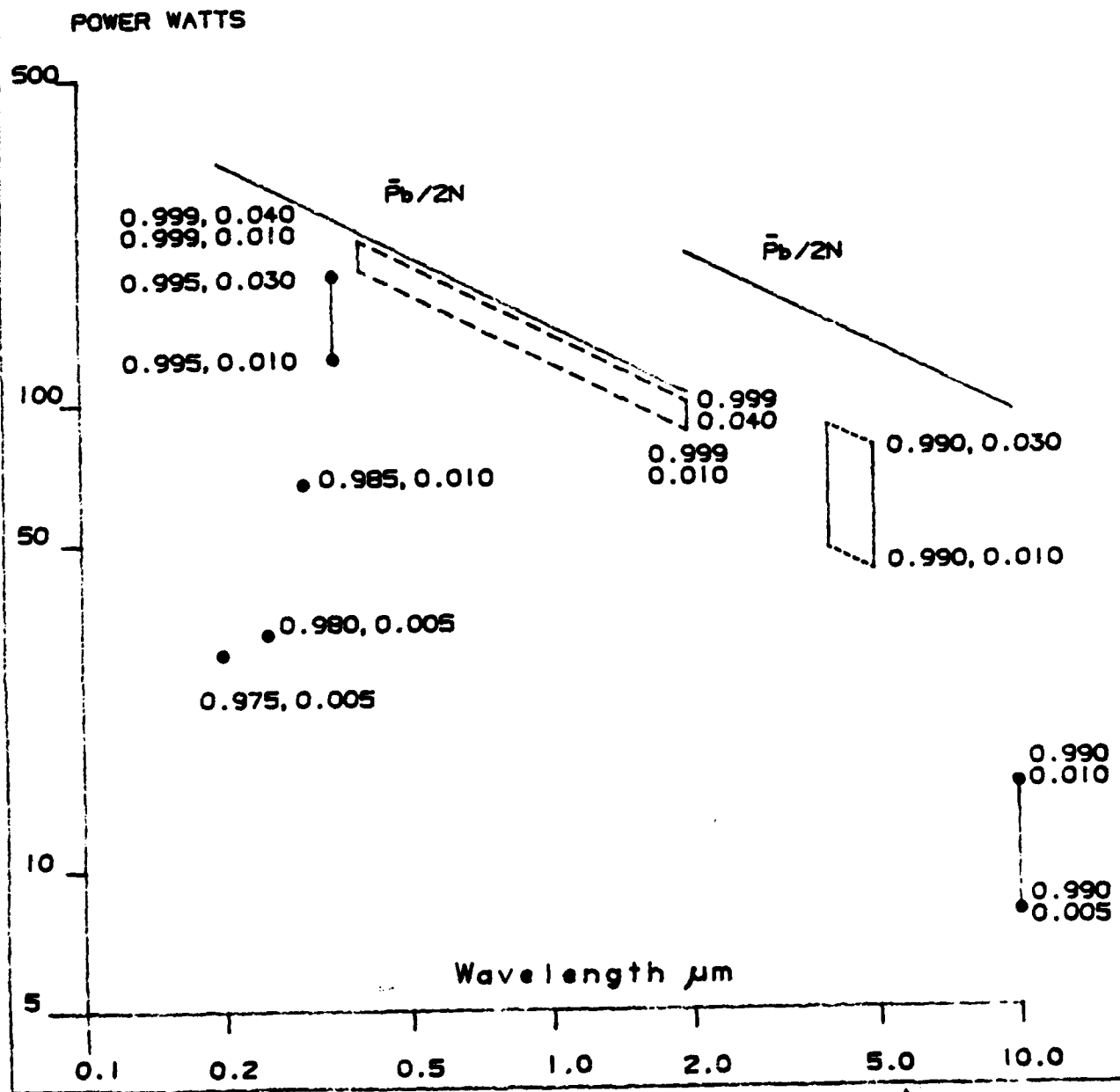


FIGURE 4
 PEAK OUTPUT IRRADIANCE, $W\ cm^{-2}$

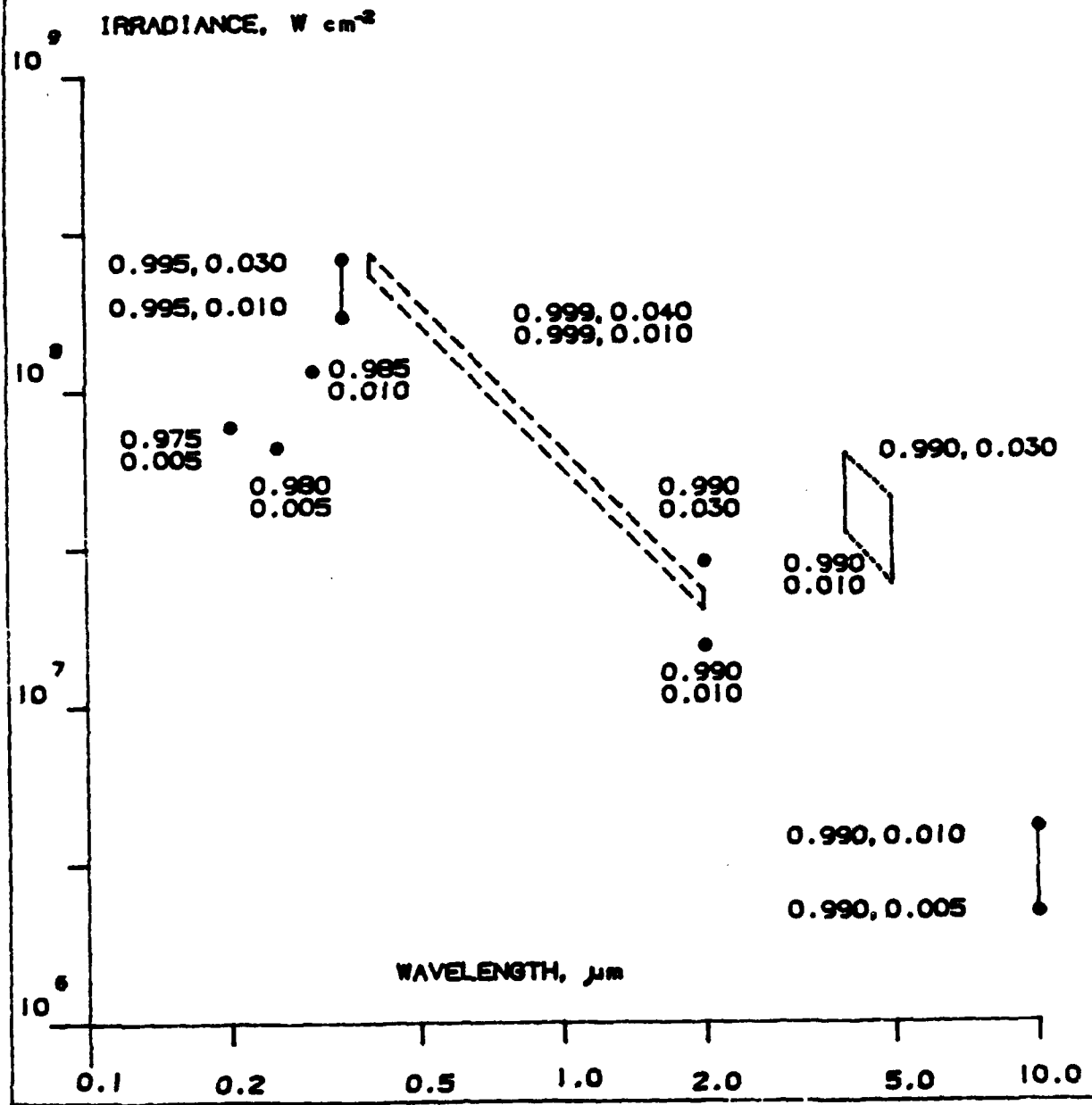
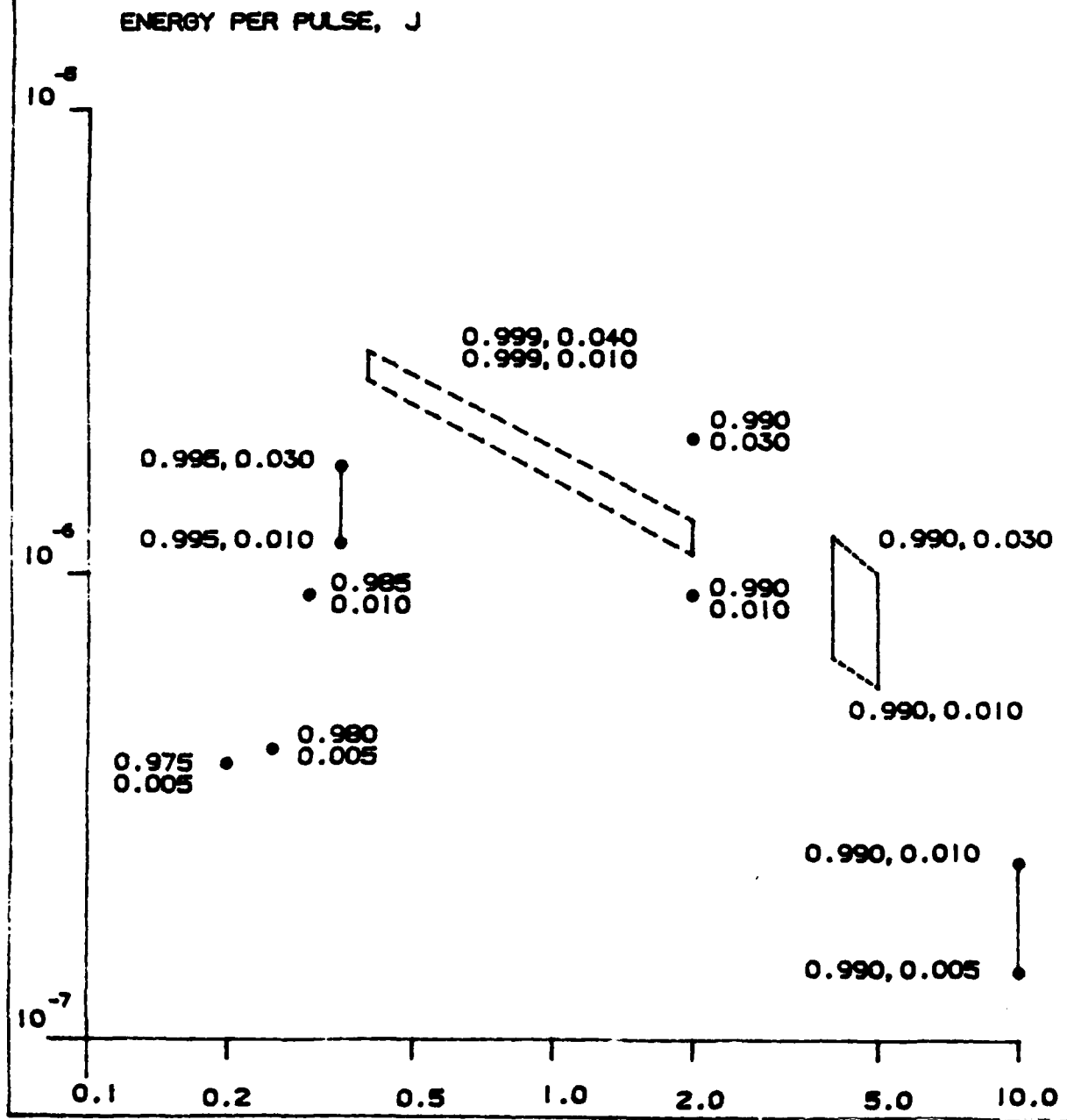


FIGURE 5
PEAK OUTPUT ENERGY, J



SYNCHRONOUSLY - PUMPED, CAVITY - DUMPED, DYE LASER: SEE
 J. M. HARRIS, R. W. CHRISMAN AND F. E. LYTLE
 APPL. PHYS. LETT., 26, 16 1975

TUNABLE FROM 570 TO 640 nm
 5 nJ/PULSE AT 580 nm AT < 500 KHz
 1 nJ/PULSE AT 580 nm AT 10 MHz

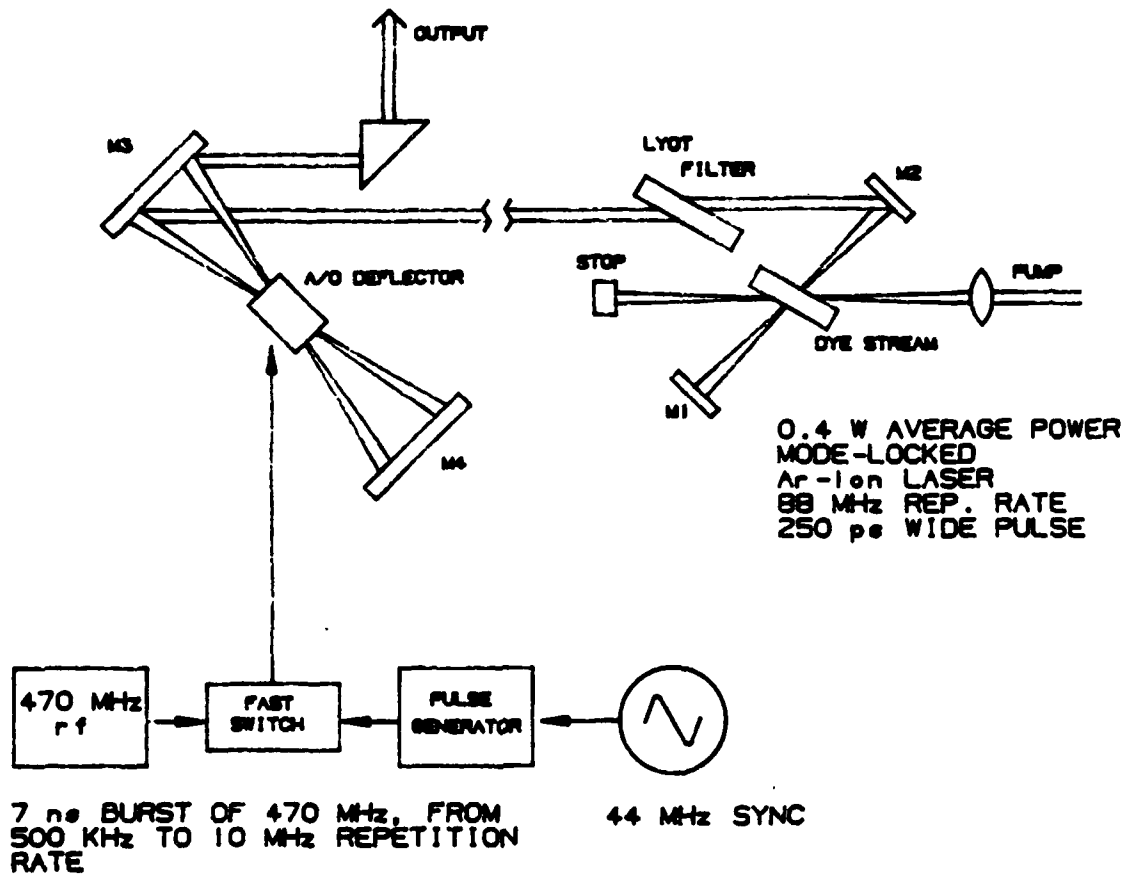


FIGURE 6

APPENDIX H

Design Note 7

Tuning the Optical Wavelength and Diffraction Losses in the IR

FEL Design Note 7

C. Johnson

November 18, 1987.

Tuning the optical wavelength and Diffraction losses in the IR

We expect to vary the FEL optical wavelength by changing the electron beam energy and the value of the peak magnetic field of the wiggler. We will scan the optical wavelength while maintaining approximately constant optical power by varying the magnetic field. The electron beam energy will be given by the number of orbits through the accelerator and by the energy gained per orbit. For a $\pm 20\%$ variation per orbit, the energy, in MeV, is given by

$$T = 5 + N_{orbit} (12 \pm 2.4) \text{ MeV.}$$

The values of the beam kinetic energy determine the optical wavelength and the small-signal, one-dimensional, fractional power gain G_p in the usual way (see earlier design notes). The fiducial parameters are defined in Design Note 6. It is interesting to note that for $N_{orbit} \geq 2$, the same optical wavelength can be obtained for two or more values of N_{orbit} (see Figure 1). In fact, at $B_0 = 5400$ Gauss the only gap in the optical wavelength occurs between $12 \mu\text{m}$ and $18.4 \mu\text{m}$, corresponding to the low energy limit of orbit 2 and the high energy limit of orbit 1. In theory, it is possible to cover this gap by decreasing the peak magnetic field from B_0 to $0.6 B_0$ with T held fixed at 19.4 MeV (e.g., see Figure 2 in Tang et. al., PAC Conf. Proc. 1987), so that the FEL could be tuned from 150 nm to $32 \mu\text{m}$. However, diffraction losses in the IR will not

support such a broad dynamic range of operation (see below).

To estimate diffraction losses, I have followed the procedure outlined in Design Note 6 (see D.N. 6, Table 3), but with the wavelength extended to 35 μm . The fractional power loss per aperture is plotted in Figure 2 for the wiggler vacuum chamber, the dump and D17 magnet vacuum chambers, and the cavity end mirrors. The dump magnet vacuum chamber is taken to be 2.5 cm x 2.5 cm. The quad magnet vacuum chambers do not contribute to the diffraction losses.

To compare these losses to the small-signal one-dimensional power gain, I assume that diffraction is the only loss mechanism:

$$R^2_{diff} = (1 - D_{MR})^2 (1 - D_W)^4 (1 - D_{MAG})^4$$

where MR , W , and MAG stand for the cavity end mirrors, the wiggler vacuum chamber, and the dump/D17 magnet pair. The quantity R^2_{diff} is compared to the minimum value that is required to overcome the oscillator threshold:

$$R^2_{min} = \frac{1}{1 + G_p}$$

The maximum wavelength is around 12 μm (see Figure 3).

In an actual optical resonator, the reflectivity of the cavity mirrors would have to be included:

$$R^2_{eff} = R_{HR} R_{OC} R^2_{diff}$$

so that the maximum value of the optical wavelength would be less than 12 μm . It should be emphasized that the diffraction losses in this design note are estimated, and that the small signal gain is for the one

dimensional case. It may be that optical guiding will offset diffraction so that the FEL will lase at wavelengths longer than 12 μm .

Erratum to Design Note 6

The stability condition on page 1 should read $0 < g_1 g_2 < 1$,

not $|g_1 g_2| < 1$.

ME SEISMOLOGICAL SERVICE TO INDIANS
BENTLEY & BAKER CO. MEMPHIS

46 5506

Figure 1

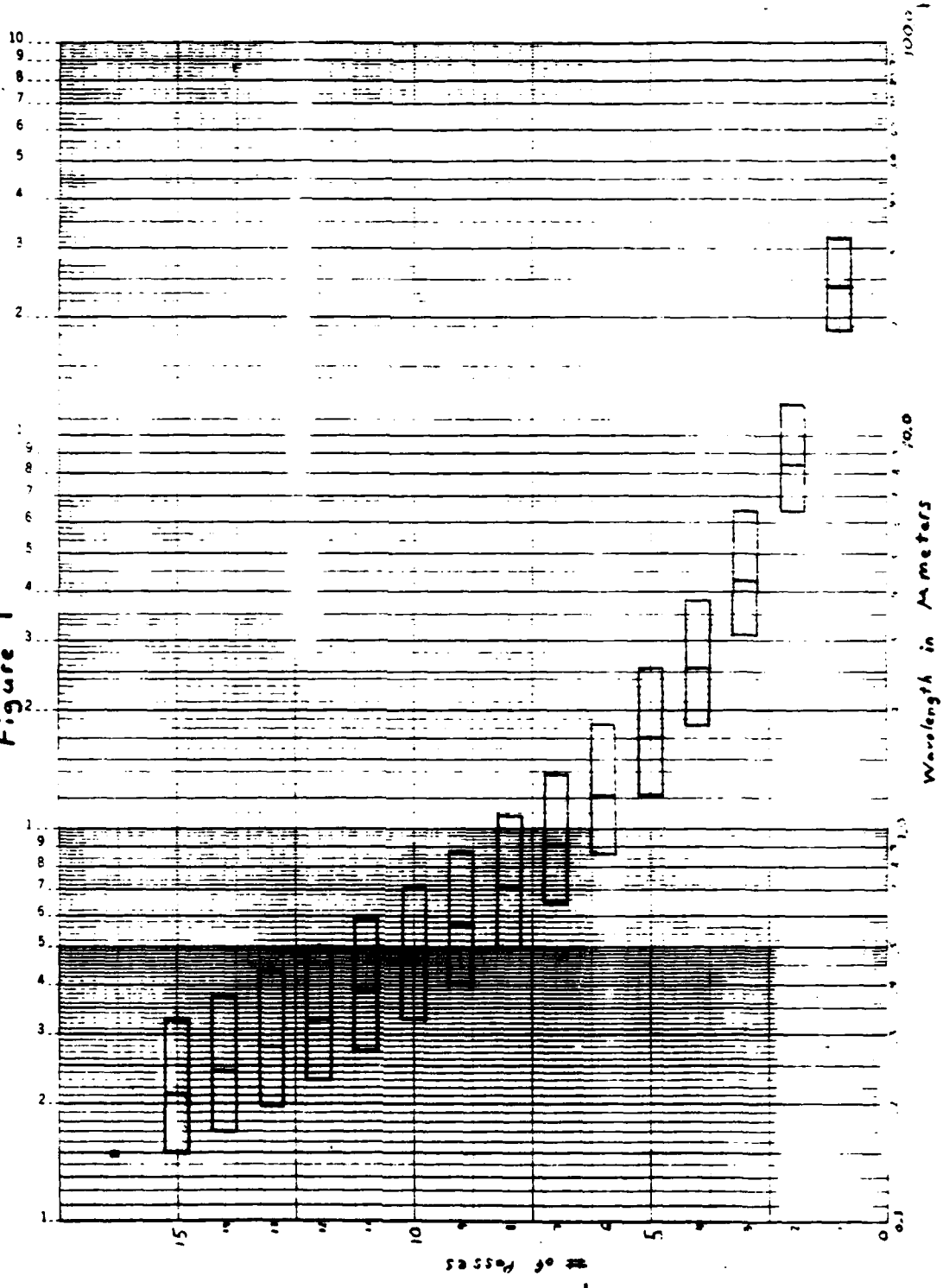


Figure 2

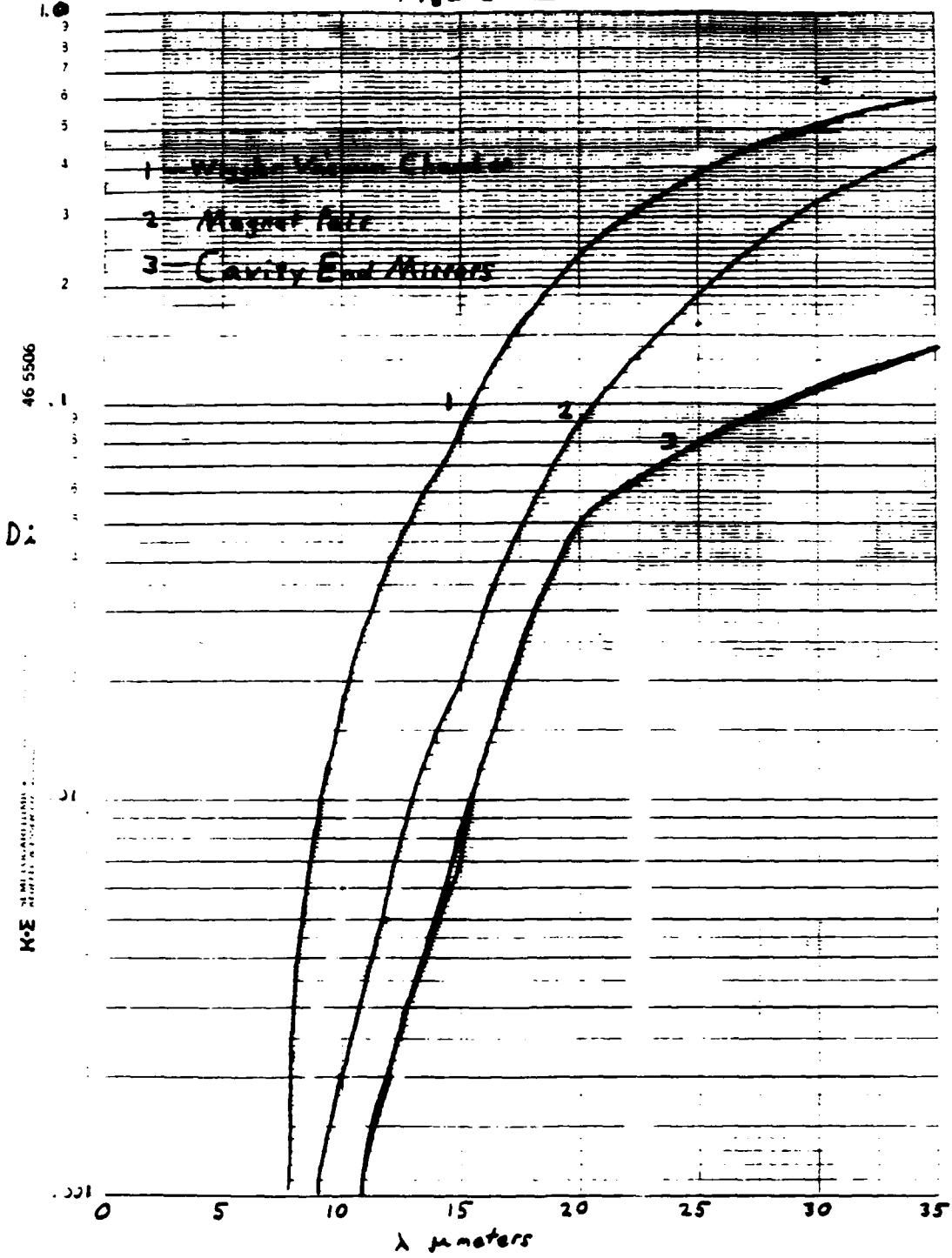
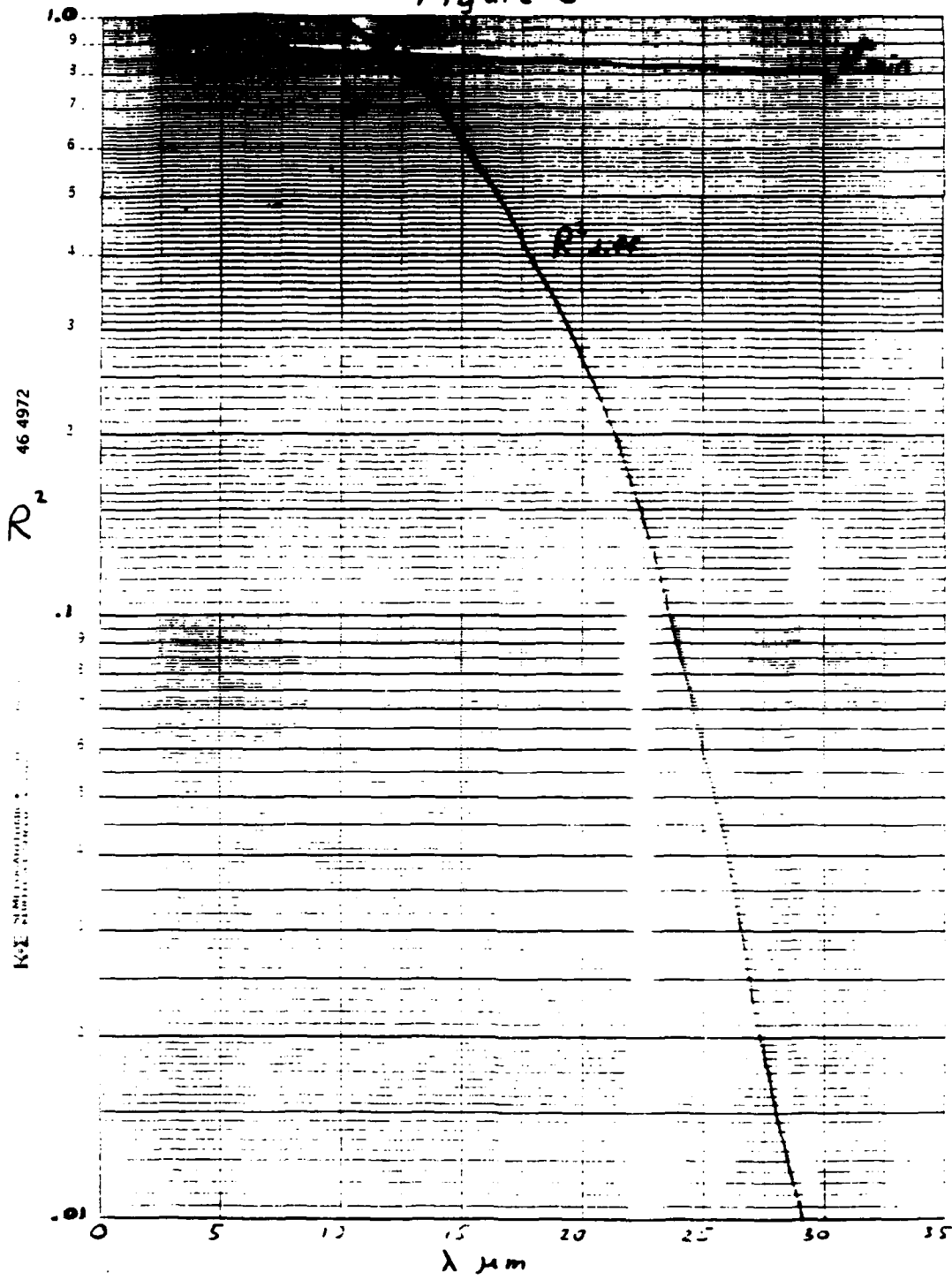


Figure 3



46-4972

R^2

K-1 SIMILAR...

APPENDIX I

Design Note 8

Electron Beam Phase Stabilization

FEL Design Note #8
Electron Beam Phase Stabilization

Samuel Penner
November 4, 1987

In a recent conversation with Tom Baer, he asked if it would be possible to stabilize the electron beam phase beyond the $\pm 0.5^\circ$ that we expect to achieve. His reason for doing so is that if the beam phase and therefore the RF frequency is sufficiently stable, it might (when combined with several other features) allow frequency locking between the RF and the FEL optical output. This could have very important metrological applications. The stabilization process would require a large bandwidth because some very high harmonic of the RF frequency is needed to begin the chain of frequency multiplications which relates RF frequency to optical frequency.

A preliminary look at this problem indicates that beam phase stabilization is possible by a feedback scheme, provided that a phase error signal can be derived from the beam. The feedback device is an RF cavity which modulates the beam energy preceding a portion of the beam transport system which provides time dispersion (i.e. transport matrix element $R_{56} \neq 0$). Specifically, a cavity with peak RF voltage ΔV located on the last return leg of the RTM will produce a phase change at the FEL of $\Delta\phi = R_{56}(\Delta V/E_0)$ where E_0 is the extracted beam energy. For the case of extraction at 185 MeV, our earlier transport calculations give $R_{56} = -54$ degrees per percent energy change. If the feedback cavity is phased so that the beam traverses it at its peak phase, a cavity voltage amplitude of 34 kV is required to change the beam phase by 1° at the FEL. A second cavity located on the extraction line (say on the segment between Q19 and D14) with the same amplitude and opposite phase relative

to the beam, will eliminate the energy modulation. The effect of these cavities on the transverse optics is negligible. The effect on the energy and phase spread of the beam is likewise negligible because of the small phase spread in the beam. In principle, by operating at larger amplitudes and different phases, these same cavities could be used to manipulate the beam longitudinal phase space, e.g., to shorten the pulse from its nominal 3° phase spread.

A single 2380 MHz cavity can provide the 34 kV amplitude drive. It must be a low Q cavity because we would like to have feedback response at the FEL optical cavity frequency, which is the 128th subharmonic of the RF fundamental frequency (18.594 MHz). This requires a cavity Q of order 100. Since $(R/Q) = 350 \Omega$ for the cavities in our main linac sections, a cavity of the same geometry with $Q = 100$ requires 33 kW of drive power. This is high, but not intractable. The power required could be further reduced by using a multiple cell cavity, e.g., a three cell cavity would require only 11 kW. It may also be possible to use less cavity voltage. At present the observed beam phase jitter at 5 MeV is less than 1° (peak to peak). Some of this jitter originates in noise in the high voltage terminal and very likely can be reduced. Further, if the phase jitter has no frequency components in the 18 MHz range, the cavity Q can be increased to reduce the power needed.

To preserve maximum bandwidth, the sensor which generates the phase error signal on the beam must be located near the RTM. It would not be feasible to generate the phase error signal at the FEL because the transit time of the beam from the feedback cavity to the FEL is approximately 80 ns. It would take a similar time for an error signal to travel back to the drive cavity. From the propagation delays alone, the maximum feedback bandwidth must be less than 6 MHz.

While it would be interesting to pursue these possibilities further, this development is beyond the scope of the present FEL project, and we have no funding at present to implement it.

APPENDIX J

Design Note 9

Lasing on the Harmonics

FEL Design Note 9
Lasing on the Harmonics

C. Johnson

March 15, 1988

The short wavelength, or ultraviolet, cutoff for lasing with the NBS/FEL is determined by the point where the small signal power gain no longer exceeds the cavity losses. This design note shows that we can operate at shorter wavelengths while sacrificing output power by adjusting the electron energy for operation at λ_1 , the "fundamental wavelength", and adjusting the cavity mirrors for operation at $\lambda_3 = \lambda_1/3$, the "third harmonic wavelength". This is because for *fixed lasing wavelength*, in the one-dimensional approximation, and with the maximum magnetic field, the small signal power gain in the third harmonic is higher than that of the fundamental. This is also true for the fifth harmonic, but not for harmonics with $n \geq 7$.

The maximum value of the one-dimensional, small-signal power gain, G_n , for the n^{th} harmonic is

$$G_n = n F_n^2(K) K^2 N^3 \frac{I}{I_A} \frac{\pi^2 \lambda_w^2}{\sigma_R \gamma^3}$$

where the symbols have their usual meaning [Ref. 1]. The ratio of the gain in the harmonic to that of the fundamental is

$$\frac{G_n(K)}{G_1(K)} = \frac{n}{1} \frac{F_n^2(K)}{F_1^2(K)} \frac{\gamma_1^3}{\gamma_n^3} = n \frac{F_n^2(K)}{F_1^2(K)} \left\{ \frac{\lambda_w}{\lambda} \frac{n\lambda}{\lambda_w} \right\}^{3/2} = n^{5/2} \frac{F_n^2(K)}{F_1^2(K)}$$

Here λ is the lasing wavelength. The cross sectional area of the radiation field cancels since the lasing wavelength is the same in either case. The functions F_n involve the differences of Bessel functions, where the argument

depends on the harmonic index and the value of the wiggler parameter, K . For the NBS FEL, K is between 1.0 and 0.6 (rms). Substituting for F_n [Ref. 2],

$$\frac{G_n(K)}{G_1(K)} = n^{5/2} \frac{\left[\frac{J_{n-1}(n\xi)}{2} - \frac{J_{n+1}(n\xi)}{2} \right]^2}{\left[J_0(\xi) - J_1(\xi) \right]^2},$$

where $\xi = K^2/(2(1+K^2))$. At $K = 1.0$, $\xi = 0.25$ and $G_3/G_1 = 1.677$ and $G_5/G_1 = 1.360$. At $K = 0.6$, $\xi = 0.13$ and $G_n < G_1$ for all values of n .

Having established that the harmonic gain can exceed that of the fundamental in certain limits, the actual value of the gain must be determined. The one-dimensional formulation neglects several effects and cannot be used to predict absolute values for the small signal power gain. Assuming that the ratio of the gain in a harmonic to that of the fundamental is given by the one-dimensional result, I have calculated the harmonic gain from Tang's 3-D calculations, with normalized beam emittance of 10 mm-mrad. I fitted three points in her figure (see Figure 6 in Ref. 1), corresponding to $K = 1.0$, $\epsilon_n = 10$ mm-mrad, and $\gamma = 350, 250,$ and 150 , to the function $a\lambda^b$. The result is $G_1(3-D) = 31.7\lambda^{0.71}$, where λ is in μm . Then, the gain in the third harmonic is 1.68 times $G_1(3-D)$. This information is plotted in Figure 1, along with representative values for the overall cavity power loss per pass. The cavity losses were calculated using excimer laser mirror specifications, see Table 1. The outcoupling factor is 5% for all wavelengths. The ability to lase on the third harmonic extends our operating range from 200 nm to about 150 nm.

Table 1

Mirror Parameters

Wavelength nm	Power Reflection Coefficient		$\frac{1 - R_{\text{eff}}^2}{R_{\text{eff}}^2}$
	High Reflector	Output Coupler	
146	0.960	0.910	0.145
158	0.970	0.920	0.121
172	0.980	0.930	0.097
193	0.990	0.940	0.075
212	0.990	0.940	0.075
222	0.990	0.940	0.075
248	0.990	0.940	0.075
266	0.990	0.940	0.075
282	0.990	0.940	0.075
308	0.990	0.940	0.075
325	0.999	0.949	0.055
337	0.999	0.949	0.055
352	0.999	0.949	0.055
400	0.999	0.949	0.055
1000	0.999	0.949	0.055

In the low-gain, one-dimensional approximation, the coupling efficiency η , which, in the case of an untapered wiggler and a lossless cavity, relates the average output power to the average power in the electron beam, is given by $\eta_n = 1/(2nN)$ [Ref. 2]. For the same lasing wavelength, the average power in the third harmonic is $\langle P_r \rangle_3 = \langle P_r \rangle_1 / (3\sqrt{3})$. The factor of $\sqrt{3}$ occurs because the third harmonic is lasing with a value of γ that is reduced by this factor, and the average electron beam power is linear in γ . In terms of the fiducial parameters (repetition rate of 74.375 MHz, peak current of 2 A, pulse width of 3 ps, and $K = 1.0$),

$$\langle P_r \rangle_1 = \eta_1 \langle P_b \rangle = 146.76/\sqrt{\lambda}, \text{ and}$$

$$\langle P_r \rangle_3 = \eta_3 \langle P_b \rangle = 28.24/\sqrt{\lambda},$$

where λ is in μm and $N = 130$. See Figure 2.

References

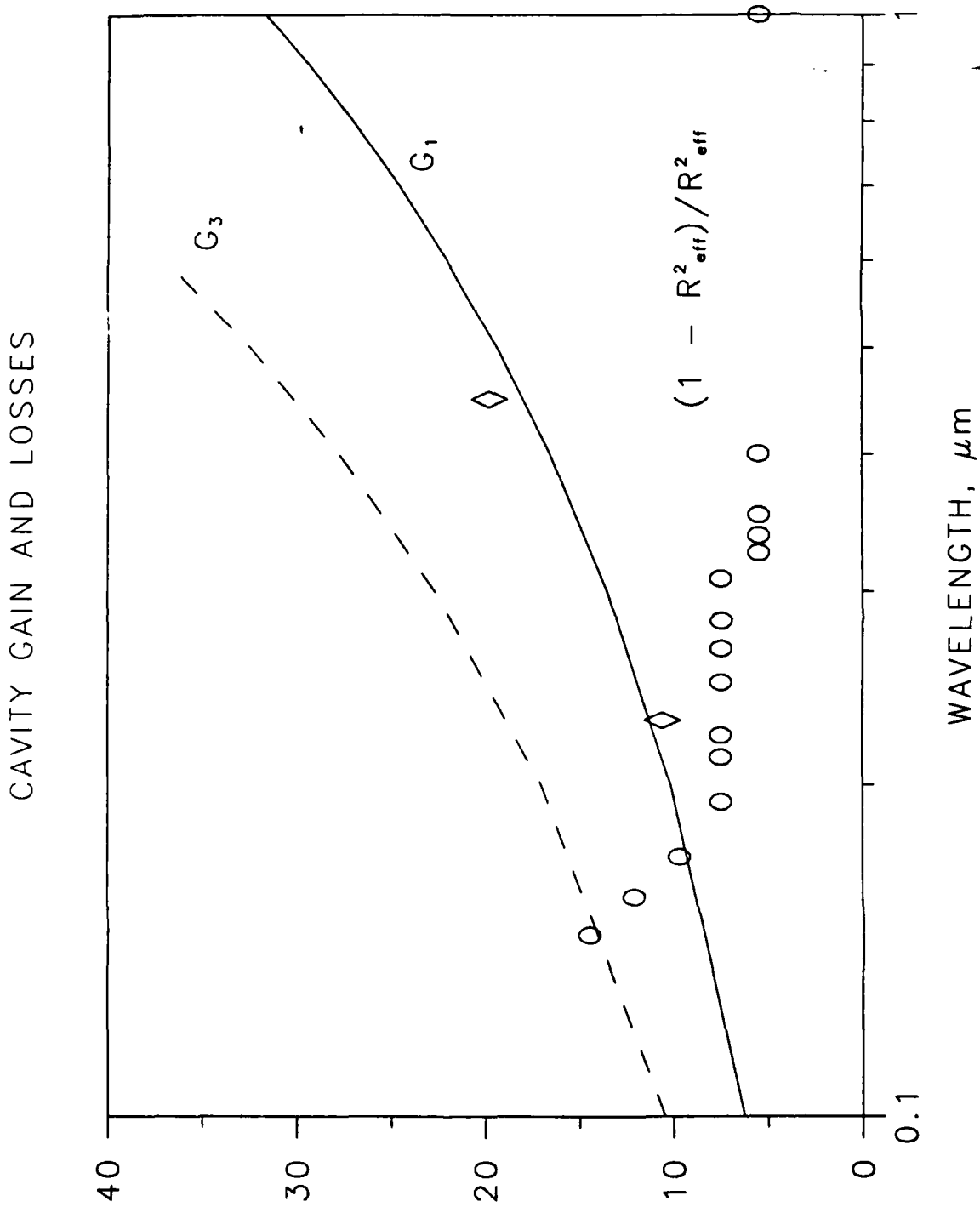
1. "The NBS/NRL Free Electron Laser Facility", S. Penner *et al.*, to appear in the *Proceedings of the Ninth International Free Electron Laser Conference*, (1988).
2. B. Hafizi and C.-M. Tang, personal communication, (1988).

Figure Captions

Figure 1. Typical cavity losses for multi-layer dielectric mirrors (open circles) and the calculated three-dimensional power gain for the fundamental (solid line) and third harmonic (dashed line). Tang's three-dimensional result for $\gamma = 350$ and 250 are shown as open diamonds.

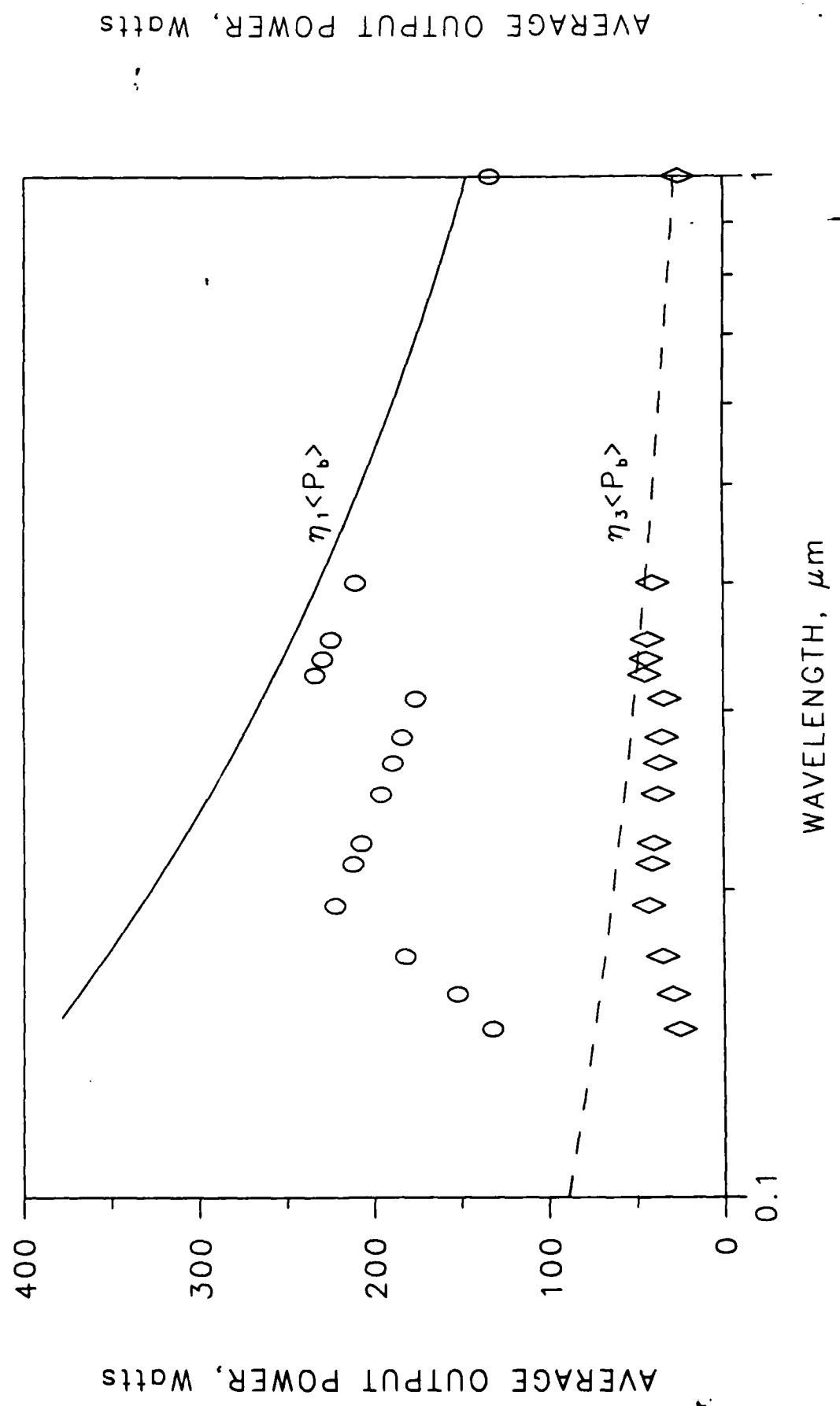
Figure 2. Calculated average output power for the NBS/FEL. The solid line and the open circles correspond to the maximum output power available and the actual output power obtained, using the mirrors and wavelengths listed in Table 1. The dashed line and the open diamonds are the equivalent result for the third harmonic.

SMALL SIGNAL POWER GAIN/LOSS, PERCENT



SMALL SIGNAL POWER GAIN/LOSS, PERCENT

NBS-NRL FEL; FIRST AND THIRD HARMONIC



AVERAGE OUTPUT POWER, Watts

AVERAGE OUTPUT POWER, Watts

APPENDIX K

Analysis of Free Electron Laser Performance Utilizing the

National Bureau of Standards' CW Microtron

**ANALYSIS OF FREE ELECTRON LASER PERFORMANCE
UTILIZING THE NATIONAL BUREAU OF STANDARDS' CW MICROTRON**

Cha-Mei Tang and Phillip Sprangle

Plasma Physics Division, Naval Research Laboratory, Washington, D.C. 20375-5000

Samuel Penner

Center for Radiation Research, National Bureau of Standards, Gaithersburg, MD 20899

Xavier K. Maruyama

Department of Physics, Naval Postgraduate School, Monterey, CA 93943

Abstract

The National Bureau of Standards' (NBS) CW racetrack microtron (RTM) will be utilized as a driver for a free electron laser (FEL) oscillator. The NBS RTM possesses many exceptional properties of value for the FEL: i) CW operation, ii) energy from 20-185 MeV, iii) small energy spread and emittance, iv) excellent energy stability, and v) high average power. The 1-D FEL gain formula predicts that the FEL would oscillate at the fundamental approximately from 0.25 μm to 10 μm when up-grading the peak current to ≥ 2 A. In this paper, we present 3-D self-consistent numerical results including several realistic effects, such as emittance, betatron oscillations, diffraction and refraction. The results indicate that the design value of the transverse emittance is small enough that it does not degrade the FEL performance for intermediate to long wavelengths, and only slightly degrades the performance at the shortest wavelength under consideration. Due to the good emittance, the current density is high enough that focusing, or guiding, begins to manifest itself for wavelengths $> 2.0 \mu\text{m}$.

Introduction

An FEL facility for applications, primarily in biomedical and material science research as well as for basic physics and chemistry, is to be situated at the National Bureau of Standards^{1,2}. A CW 185 MeV racetrack microtron (RTM)³ is under construction. The NBS Accelerator Laboratory consists of a series of interconnected, individually shielded, underground halls. The updated layout is indicated in Fig. 1. The FEL is expected to be operational by 1990.

The major limitation of an RTM as an FEL driver is that its peak current capability is lower than electron linacs which operate in the same energy range. However, the RTM is superior to pulsed linacs in energy spread and emittance. The RTM is comparable to a storage ring in terms of beam emittance and energy spread, but there is no restriction on insertion length or "stay clear" aperture. The beam energy can be varied continuously over a wide range without significant loss of performance. In addition, microtrons are compact and energy efficient. Because of the CW nature of the RTM, the generation of coherent photons is not hindered by a finite macropulse length.

The original design parameters of the NBS RTM are given in Refs. 1-3. The design calculations indicate a longitudinal emittance $\epsilon_L < 30$ keV-degrees and a normalized transverse emittance^{1,2} $\epsilon_N < 10$ mm-mrad. Based on recent measurements of the performance of the 5 MeV injector linac, the actual values of both the longitudinal and transverse emittance are expected to be smaller than the design values. The injector system must be upgraded to provide a peak current of ≥ 2 A in 3.5 psec micropulses, giving electron pulse length $\ell_{eb} \simeq 0.1$ cm. In order to keep the average electron beam power within the capability of the existing RF power system, the new injector will fill only a small fraction of the RF buckets (e.g., 1/24, 1/120 depending on electron beam energy). We are proceeding with a design of a photocathode injector system for this upgrade.

1-D Free Electron Laser Analysis

A first order evaluation of the FEL performance of the NBS RTM can be obtained from the 1-D small signal low gain formula⁴. The results indicate that sufficient gain can

be obtained at fundamental wavelengths in the range from $10 \mu m > \lambda > 0.25 \mu m$. The formula for the electric field amplitude gain G in the small signal, low gain regime, can be written as

$$G = F_1^2 \frac{\pi^2}{\sigma_R} \frac{I}{I_A} \frac{\lambda_w^2}{\gamma_0^3} K^2 N^3 \frac{\partial}{\partial \nu} \left(\frac{\sin \nu}{\nu} \right)^2,$$

where N is the number of wiggler periods, γ_0 is the initial relativistic gamma factor, $\sigma_R = \pi r_0^2$ is the cross-sectional area of the radiation, r_0 is the minimum $1/e$ radius of the Gaussian radiation field amplitude, $I_A = 17 \times 10^3$ A, I is the current in Amperes, $K = (|e|B_w \lambda_w / 2\pi m_0 c^2)_{RMS}$ is the wiggler parameter, B_w is the magnetic field in the wiggler, λ_w is the wavelength of the wiggler, $F_1 = J_0(b) - J_1(b)$ for a linearly polarized wiggler, $b = K^2 / 2(1 + K^2)$, $\nu = -N\lambda(\omega - \omega_0) / 2c$ is the normalized frequency mismatch, and $\omega_0 \sim 2\gamma^2 c(2\pi / \lambda_w) / (1 + K^2)$ is the resonant angular frequency. The function $\partial / \partial \nu (\sin \nu / \nu)^2$ has a maximum value of 0.54 when $\nu = -1.3$.

The power gain can be obtained by

$$G_p = (1 + G)^2 - 1.$$

In the low gain regime, $G_p \simeq 2G$. The FEL will oscillate when the power gain is greater than the losses per pass in the resonator. The 1-D gain formula is only a rough estimate. It is sensitive to the choice of filling factor.

The conceptual design consists of a linearly polarized wiggler with a period of $\lambda_w = 2.8$ cm, and a nominal magnetic field amplitude of $B_{w0} = 5400$ G. This can be constructed with a hybrid wiggler design with the gap separating the wiggler poles of $g = 1.0$ cm. A wiggler can be constructed conceptually in more than one section, such that a wiggler of shorter length can also be available. A shorter wiggler and a corresponding vacuum chamber may be necessary for long wavelength operation.

Figure 2 is a plot of the 1-D maximum small signal power gain versus wavelength, assuming a conservative peak current of 2 A. The open circles (o) are obtained with electron beam energies of 25, 50, 75, 125, and 175 MeV. The solid curves are obtained for the same electron beam energies, but varying the wiggler amplitude from $0.6B_{w0}$ to B_{w0} . The magnetic field in the wiggler is to be changed by varying the gap between the poles

from 1.4 cm to 1.0 cm. As the magnetic field decreases, the wavelength of the radiation decreases, and the gain is reduced.

3-D Effects on the Gain

Since FELs are not actually 1-D, 3-D effects will change the gain. Some of the 3-D effects that we will examine in this paper are finite transverse emittance, radiation diffraction and refraction, and some effects associated with finite-length electron pulses.

We will assess these three-dimensional effects using a fully 3-D self-consistent computer code, SHERA, developed at the Naval Research Laboratory. The formulation of the wave equation is based on the source dependent expansion⁵ of the radiation field, and the electron dynamics⁶ are evaluated self-consistently. We assume a waterbag distribution in the 4-D transverse emittance space, which leads to a parabolic profile for the electron beam density. Since the energy spread of the NBS RTM is very small, it will not be considered; and we will also not treat the effects of pulse slippage on the gain. The radiations are taken to have a Rayleigh length of 175 cm with the minimum radiation waist located at the center of the wiggler. Results for two different operating regimes will be presented.

The effect of the emittance on the performance of the FEL will be more important for short wavelength operations. Thus, our first example will be for $\lambda = 0.23 \mu\text{m}$ with $\gamma_0 = 350$. The pulse slippage distance, $N\lambda = 0.003 \text{ cm}$, is much shorter than the electron pulse length, ℓ_{eb} . The minimum $1/e$ radiation field amplitude waist is $r_0 = 3.57 \times 10^{-2} \text{ cm}$. Plots of the power gain, G_p , versus the normalized frequency mismatch, ν , are shown in Figure 3. Curve (a) gives the 1-D estimate of the gain. Curves (b), (c) and (d) are the gains calculated from the computer code for normalized transverse emittance of $\epsilon_N = 5, 10$ and 20 mm mrad , respectively. The radii of the electron beams were determined by properly matching the beam into the wiggler, i.e., the radii of the beams inside the wiggler is uniform. The matched beam radius condition is

$$r_{eb} = \left(\frac{\epsilon_N}{\gamma K_\beta} \right)^{1/2},$$

where $K_\beta = \sqrt{2}\pi K/\lambda_w \gamma$ is the betatron wavenumber for wiggler with parabolic pole faces⁷, where the focusing in both transverse directions is equal. The matched edge radius of the

electron beam can be rewritten as

$$r_{eb} = \left(\frac{\lambda_w \epsilon_N}{\sqrt{2\pi K}} \right)^{1/2},$$

independent of the beam energy. The matched edge radii of the electron beam are $r_{eb} \cong 1.77 \times 10^{-2}$, 2.50×10^{-2} and 3.54×10^{-2} cm for normalized edge transverse emittances of $\epsilon_N = 5$, 10 and 20 mm mrad, respectively. If the emittance becomes larger than 20 mm mrad, the radius of the electron beam will become larger than the radiation spot size, and the gain will be substantially reduced.

The effect of finite emittance on the gain is negligible for $\lambda = 1.25 \mu\text{m}$ with $\gamma_0 = 150$. The pulse slippage distance in this case is 0.016 cm, and it is still unimportant. Figure 4 shows plots of the power gain, G_p , versus the normalized frequency mismatch, ν , similar to Fig. 3. Again, the curve (a) gives the 1-D estimate of gain. Curves (b), (c) and (d) are the gains calculated from the computer code for normalized emittance of $\epsilon_N = 5$, 10 and 20 mm mrad, respectively. Since the wavelength is longer, the minimum $1/e$ radiation field amplitude waist becomes $r_0 = 8.3 \times 10^{-2}$ cm, and the electron beam radii are much smaller than the radiation waist. The gain at $\lambda = 1.25 \mu\text{m}$ is insensitive to the design value of the finite transverse emittance.

Figures 3 and 4 also show a shift of the zero crossing of the gain curves obtained from 3-D simulation. This shift comes from the change in the phase of the diffracting radiation field. It has no real important effect on the oscillation criteria for the examples under consideration.

Figure 5 plots the maximum 3-D power gain versus wavelength with a peak current of 2 A, for normalized emittances of 5, 10, and 20 mm mrad. Each curve is obtained for the identified electron beam energy, but varying the magnetic wiggler amplitude from B_{w0} to $0.6B_{w0}$, where the longer wavelength correspond to the larger magnetic field. Normalized emittance is very good in the long wavelength operating regime. In the shortest wavelength operating regime, the normalized emittance larger than 5 mm mrad should be avoided.

Since the current is a function of axial position in a finite length electron pulse, and pulse slippage is unimportant, the local gain is a function of the local current in the electron

pulse. For the first example at $\lambda = 0.23 \mu\text{m}$ with normalized transverse edge emittance $\epsilon_N = 10 \text{ mm mrad}$, the simulations indicate that the gain is proportional to the local current, consistent with the 1-D formula. For the second example at $\lambda = 1.25 \mu\text{m}$, the gain increases faster than the linear power of the current. Figure 6 is a plot of normalized power gain, i.e., power gain from simulation divided by the maximum 1-D power gain, versus the frequency mismatch at $\lambda = 1.25 \mu\text{m}$ with normalized transverse edge emittance $\epsilon_N = 10 \text{ mm mrad}$ for three different currents: (a) $I = 4.0 \text{ A}$, (b) $I = 2.0 \text{ A}$ and (c) $I = 0.5 \text{ A}$. We find that the normalized gain increases as current increases. This can be explained by the self-focusing or guiding phenomenon^{5,8-11} of the FEL. This is most easily observed in the plots of the normalized $1/e$ Gaussian radiation field amplitude radius, shown in Fig. 7. For $I = 0.5 \text{ A}$, the radiation radius behaves like a free space resonator radiation field, curve (- - -). For $I = 2 \text{ A}$, the radiation radius is less than the free space radius at the end of the wiggler as self-focusing begins to show, curve (—). If the current can be increased to 4 A , the radiation becomes even more focused, curve (.....). The reason that self-focusing is evident at such low current is that the emittance is very good and current density is high throughout the interaction region, i.e., high beam brightness $B_N = 2I/(\pi^2 \epsilon_N^2) > 4 \times 10^9 \text{ A/m}^2/\text{rad}^2$, where $I > 2 \text{ A}$ and edge emittance $\epsilon_N = 10 \text{ mm mrad}$.

Conclusions

The 3-D self-consistent simulation results from the computer code SHERA indicate that the design value of the transverse emittance is very good, so that it does not degrade the FEL performance for intermediate to long wavelengths. For the shortest wavelength under consideration, emittance larger than 5 mm mrad should be avoided. Due to the good emittance, the current density is high enough that focusing, or guiding, begins to manifest itself for wavelengths $> 2.0 \mu\text{m}$.

Acknowledgment

* Funded by SDIO through ONR contract No. N00014-87-f-0066.

References

- [1] C.M. Tang, P. Sprangle, S. Penner, B.M. Kincaid and R.R. Freeman, Nucl. Instr. and Meth. A250, 278 (1986). Also in: Free Electron Lasers, Proc. 7th Int. Conf. on FELs, eds., E.T. Scharlemann and D. Prosnitz (North-Holland, Amsterdam, 1986) p. 278.
- [2] X.K. Maruyama and S. Penner, C.M. Tang and P. Sprangle, Free Electron Lasers, Proc. of the 8th Intl. FEL Conf., ed., M. W. Poole (North-Holland, Amsterdam, 1987) p. 259.
- [3] S. Penner et al., IEEE Trans. Nucl. Sci. NS-32, 2669 (1985).
- [4] P. Sprangle, R.A. Smith and V.L. Granatstein, Infrared Millimeter Waves, Vol. I, ed., K.J. Button (Academic Press, New York, 1979) p. 279.
- [5] P. Sprangle, A. Ting and C.M. Tang, Phys. Rev. Lett. 59, 202 (1987), P. Sprangle, A. Ting and C.M. Tang, Phys. Rev. A36, (1987), and P. Sprangle, A. Ting and C. M. Tang, Free Electron Lasers, Proc. of the 8th Intl. FEL Conf., eds., M. W. Poole (North-Holland, Amsterdam, 1987) p. 136.
- [6] C.M. Tang and P. Sprangle, IEEE J. of Quantum Elec. QE-21, 970 (1985).
- [7] E. T. Scharlemann, J. Appl. Phys., 58, 2154 (1985).
- [8] P. Sprangle and C.M. Tang, Appl. Phys. Lett. 39, 677 (1981). Also in: C.M. Tang and P. Sprangle, Free-Electron Generator of Coherent Radiation, Physics of Quantum Electronics, Vol. 9, eds., S.F. Jacobs, G.T. Moore, H.S. Pilloff, M. Sargent III, M.O. Scully, R. Spitzer (Eddison-Wesley, Reading, MA, 1982) p. 627.
- [9] E.T. Scharlemann, A.M. Sessler and J.S. Wurtele, Phys. Rev. Lett. 54, 1925 (1985).
- [10] G.T. Moore, Opt. Comm. 52, 46(11084), 54, 121 (1985).
- [11] M. Xie and D.A.G. Deacon, same as ref. 1, p. 426.

Figure Captions

Fig. 1. Updated configuration for accelerator and FEL halls. The entire shielded complex is located 40 ft below ground level. Visible and infrared radiation will be directed to a ground level laboratory (indicated by the dashed lines) above the UV laboratory.

Fig. 2. Small signal power gain versus wavelength based on 1-D calculation.

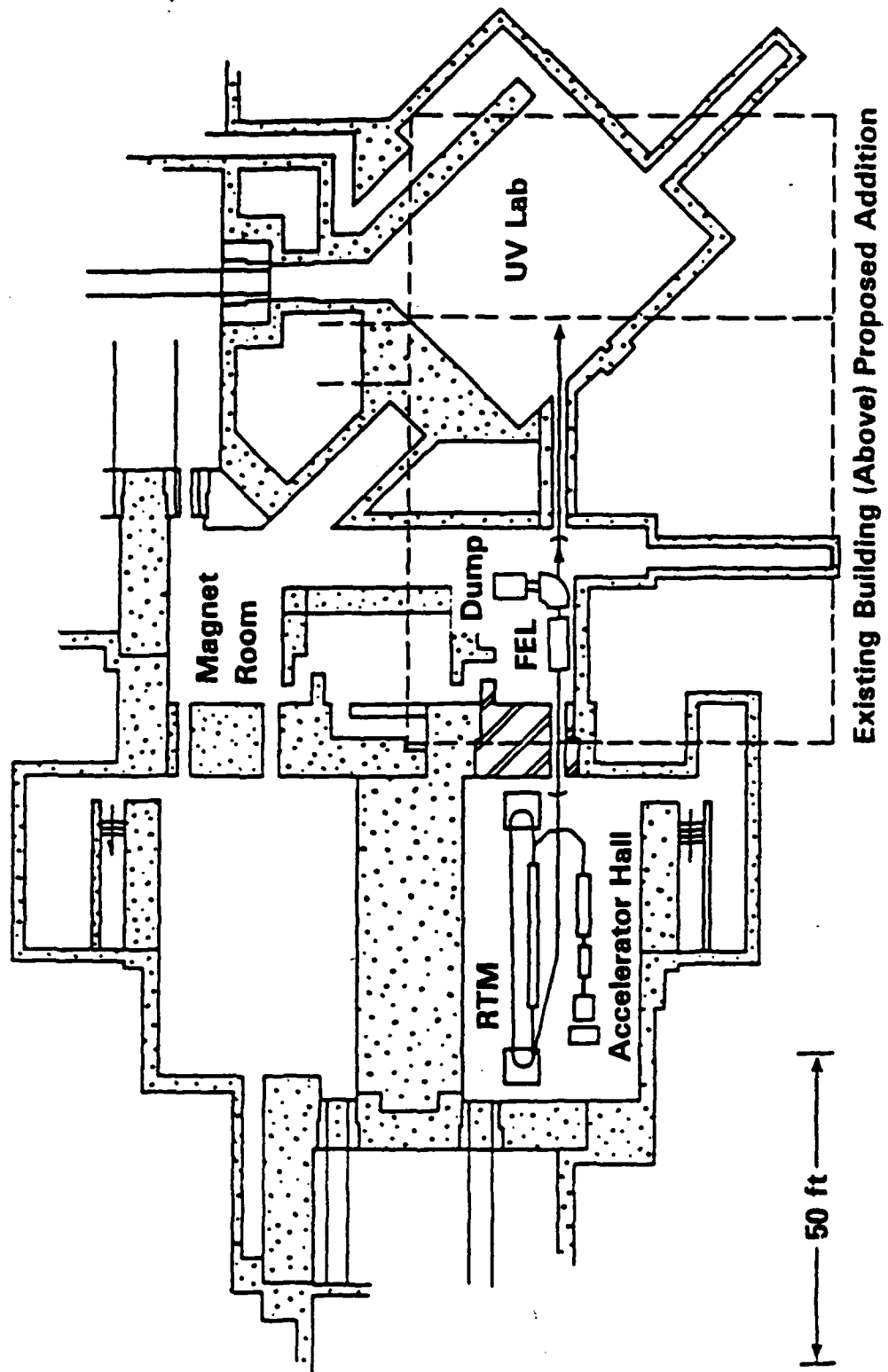
Fig. 3. Power gain, G_p , versus frequency mismatch, ν , at $\lambda = 0.23 \mu\text{m}$ with $\gamma_o = 350$. Curve (a) is based on 1-D gain formula. Curves (b), (c) and (d) are obtained from simulations with normalized transverse edge emittances of $\epsilon_N = 5, 10$ and 20 mm mrad , respectively.

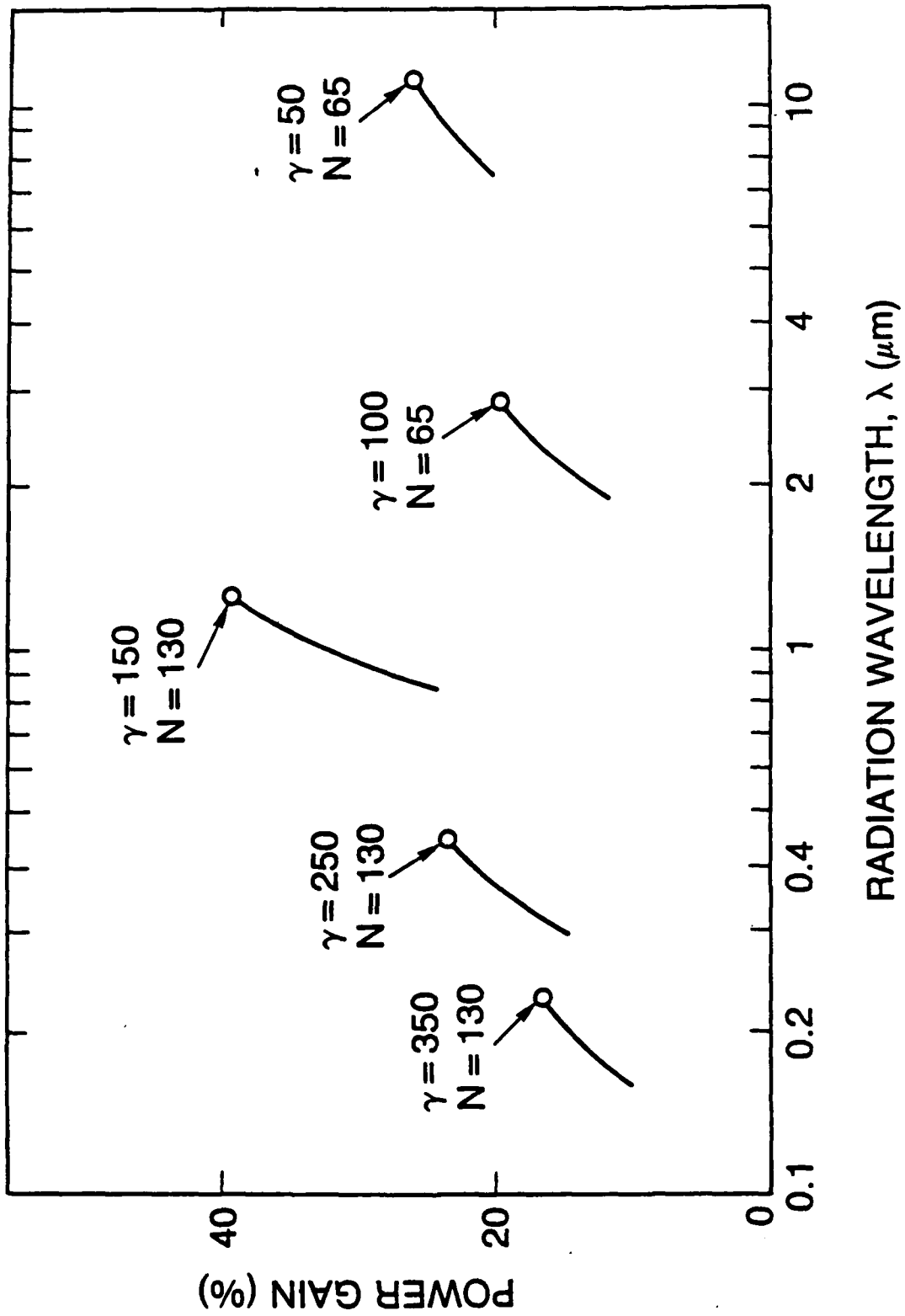
Fig. 4. Power gain, G_p , versus frequency mismatch, ν , at $\lambda = 1.25 \mu\text{m}$ with $\gamma_o = 150$. Curve (a) is based on 1-D gain formula. Curves (b), (c) and (d) are obtained from simulations with normalized transverse edge emittances of $\epsilon_N = 5, 10$ and 20 mm mrad , respectively.

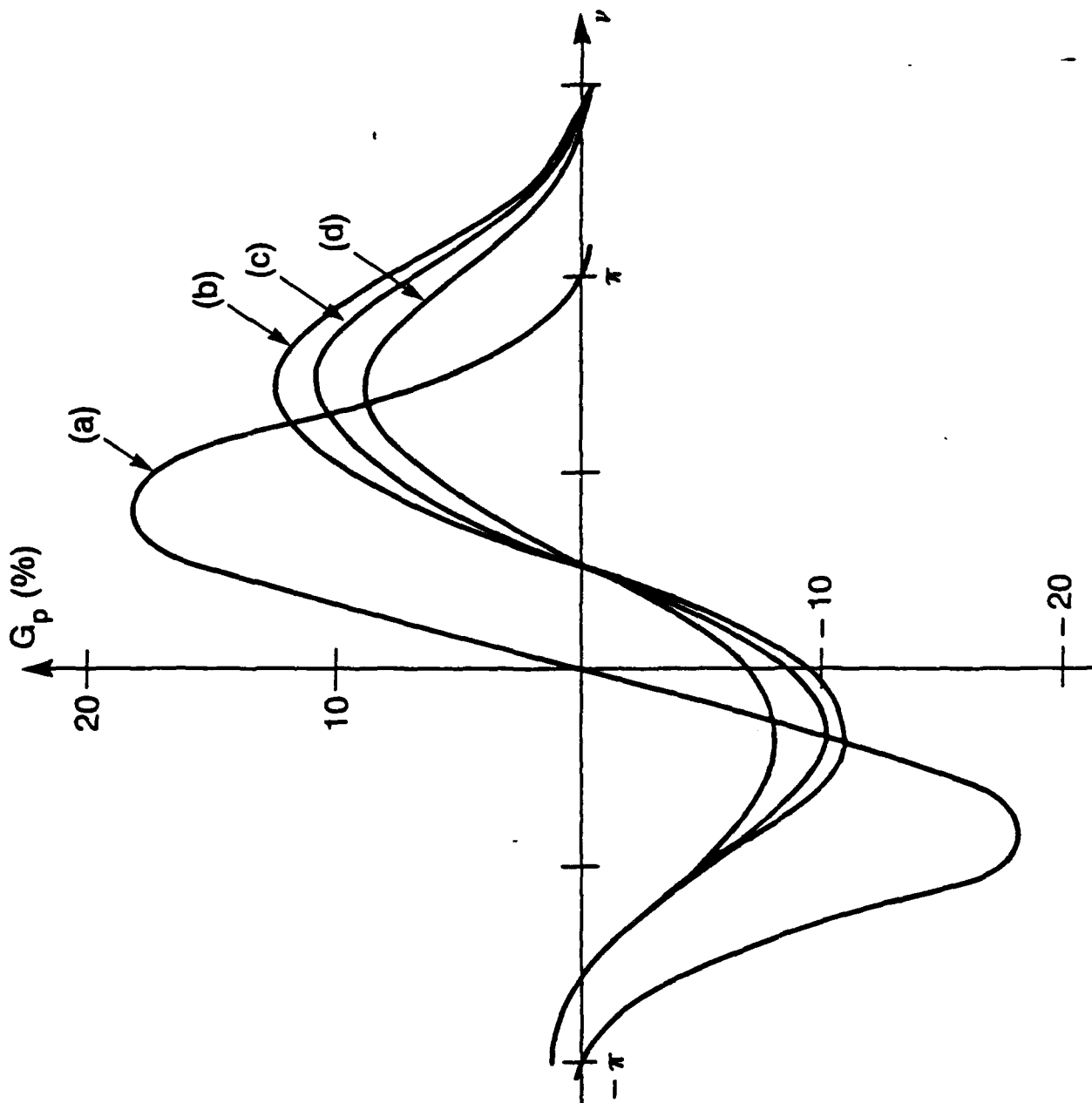
Fig. 5. Power gain versus wavelength based on a fully 3-D self-consistent simulation by varying energy and emittance of the electron beam, and the magnetic field of the wiggler.

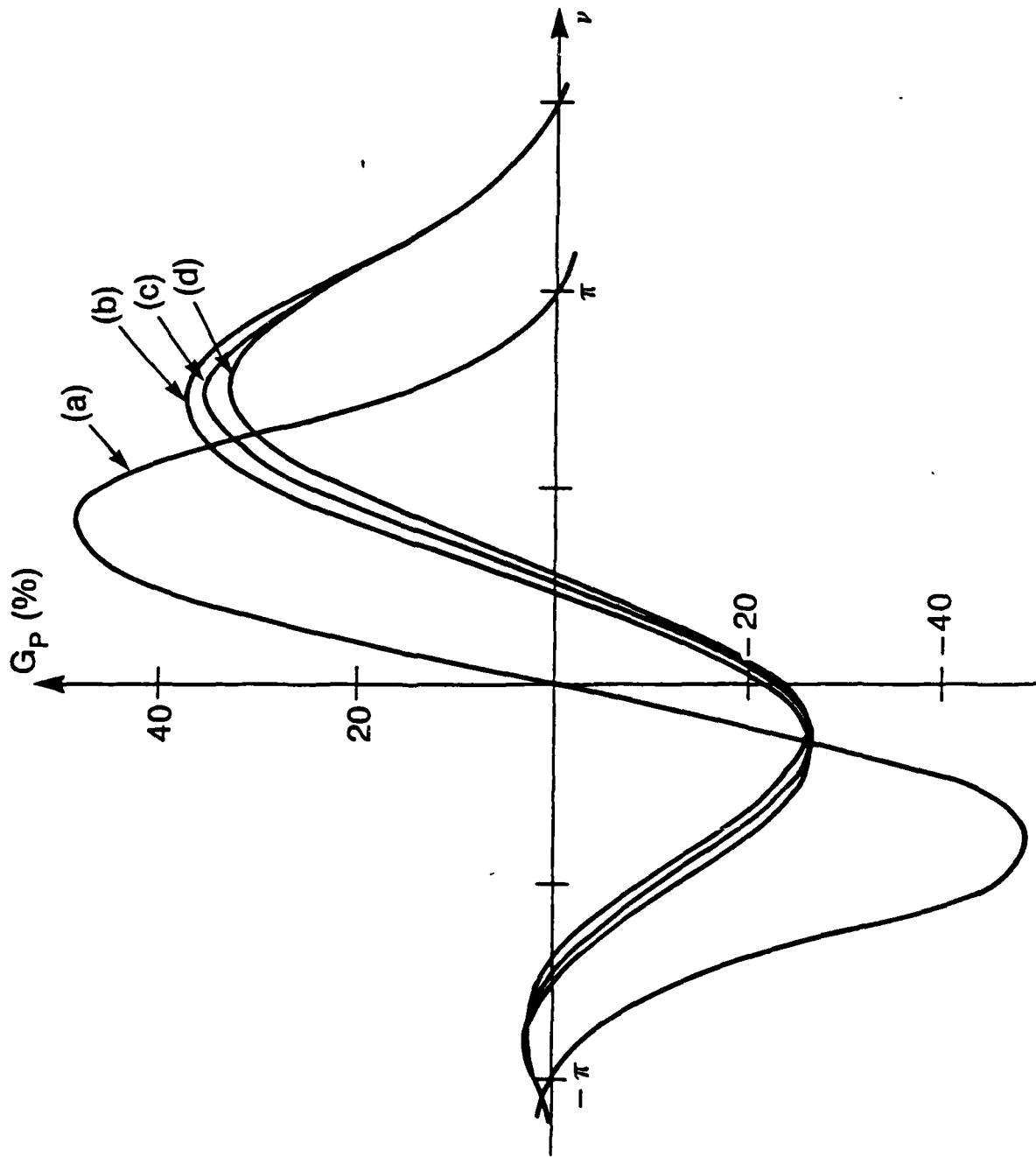
Fig. 6. Normalized gain versus frequency mismatch for $\lambda = 1.26 \mu\text{m}$ and edge emittance of $\epsilon_N = 10 \text{ mm mrad}$. Curves (a), (b) and (c) correspond to results obtained with currents of $I = 4.0, 2.0,$ and 0.5 A , respectively.

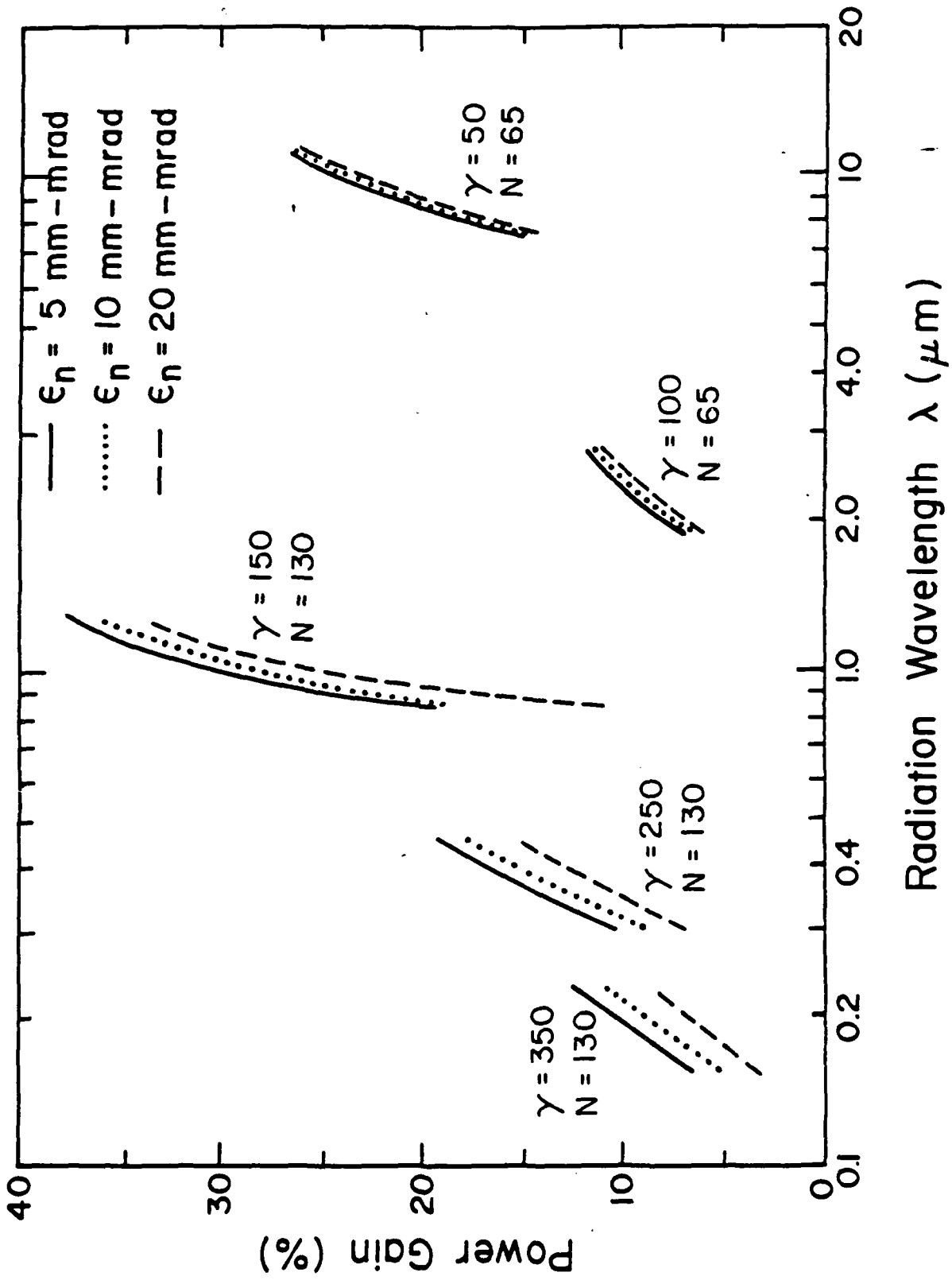
Fig. 7. Normalized $1/e$ Gaussian radiation field amplitude radius as a function of distance z in the wiggler with $\lambda = 1.25 \mu\text{m}$ and edge emittance $\epsilon_N = 10 \text{ mm mrad}$ for three different currents: (- - -) $I = 0.5 \text{ A}$, (—) $I = 2 \text{ A}$ and (.....) $I = 4 \text{ A}$.

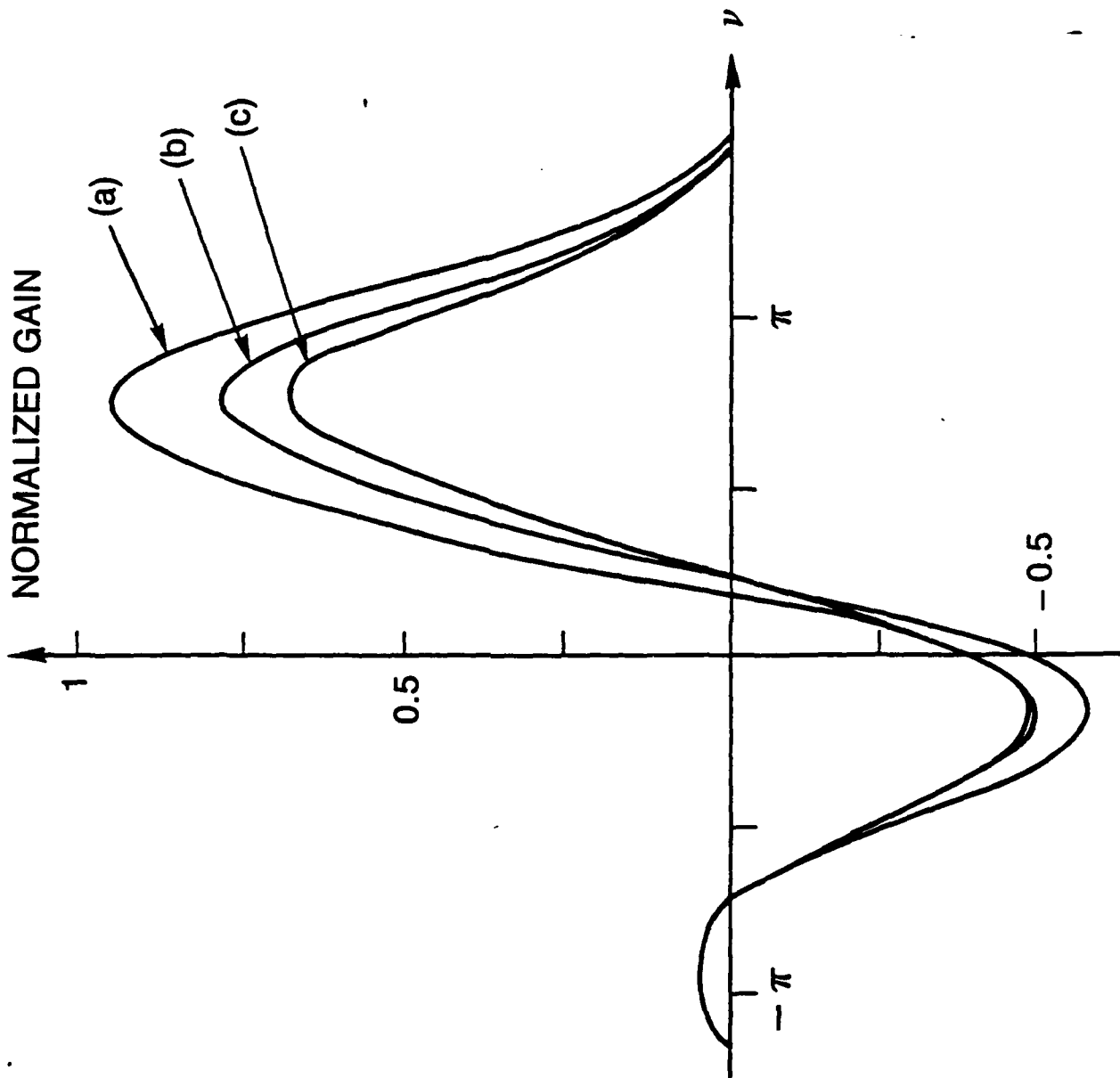


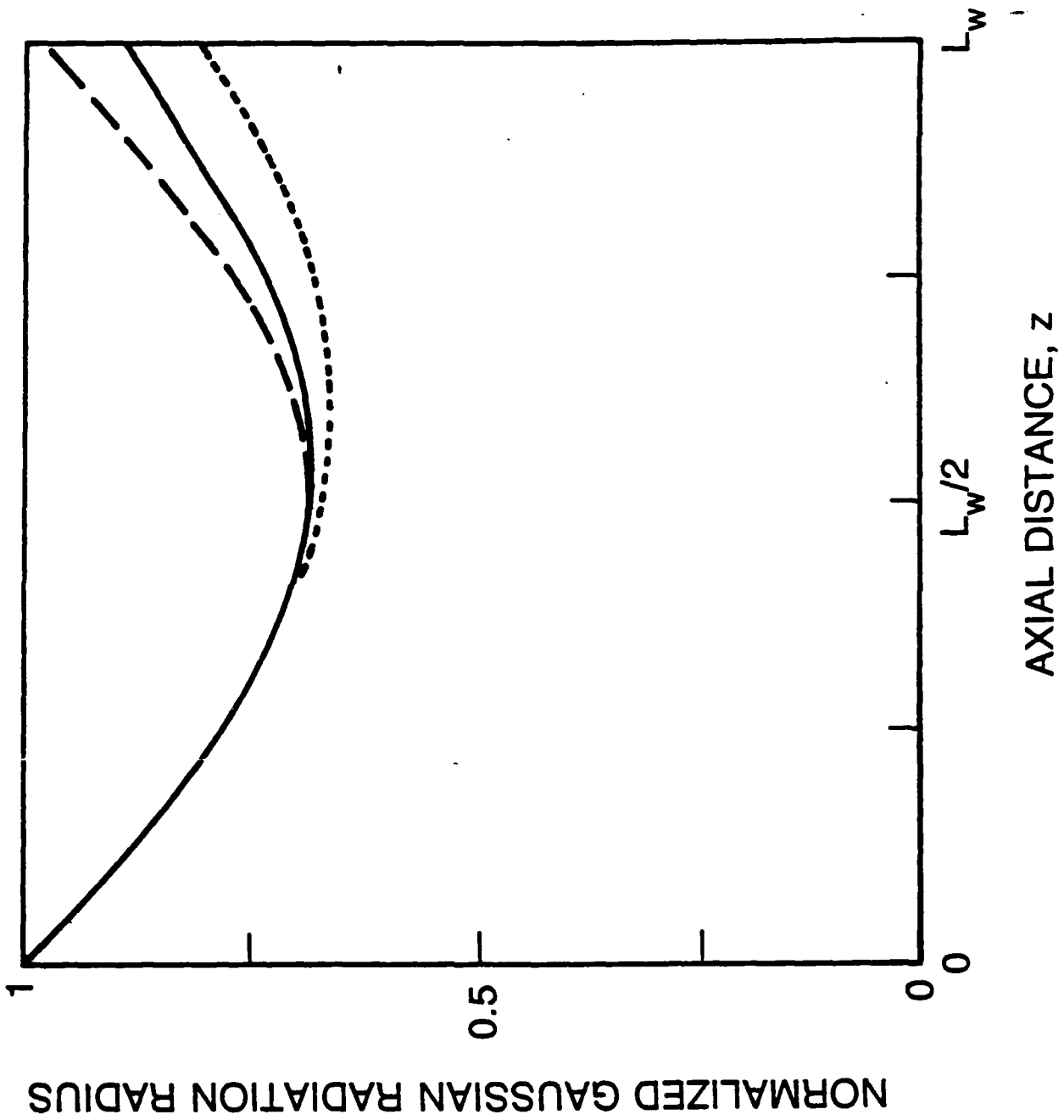












APPENDIX L

Reflection Matrix for Optical Resonators in FEL Oscillators

REFLECTION MATRIX FOR OPTICAL RESONATORS IN FEL OSCILLATORS

S. Riyopoulos^{a)}, P. Sprangle, C. M. Tang and A. Ting^{b)}

Plasma Theory Branch
Plasma Physics Division
Naval Research Laboratory
Washington DC 20375-5000

The transformations of Gaussian radiation beams caused by reflection off mirrors is an important issue for FELs operating as oscillators. The reflected radiation from a single incident Gaussian mode will contain other modes due to the finite mirror size, the deflection of the beam and mismatches in the curvature. A method for analytic computation of the reflection matrix is developed by taking the convolution of the source function at the surface of the mirror with the paraxial propagator. The mirror surface that reflects spherical incoming wavefronts into spherical outgoing is found to be a paraboloid. Integral expressions for the reflection coefficients R_{pq}^{mn} for any incoming mode u_{mn} into the outgoing u_{pq} are obtained as functions of the deflection angle ϕ , the reflected beam spot size W_0 and the mirror size. The coefficient R_{00}^{00} for the lowest-to-lowest mode reflection is determined analytically. The spot size W_0 can then be selected, depending on the mirror size, to maximize R_{00}^{00} . The ratio of the mirror size to the spot size is the dominant factor determining the reflection coefficient. The effects of deflecting the light beam enter as small corrections, of first order in the diffraction angle $\theta_d \ll 1$.

a) Science Applications Intl. Corp., McLean, VA 22102

b) Berkeley Research Assoc., Inc., Springfield, VA 22150

I. INTRODUCTION

Free Electron Lasers (FEL) operating as oscillators¹⁻⁷ require the trapping of light pulses between systems of mirrors (resonators).⁸⁻¹⁰ These pulses are repeatedly amplified via synchronous interaction with electron pulses passing through the wiggler. The simplest oscillator configuration is that of an open resonator with two opposed identical mirrors. The radiation vector potential for this arrangement is expressed in terms of the free space eigenmodes $A_{mn}(r) = A_{mn}(r)e_{mn}$ of the paraxial wave equation¹¹, where e_{mn} is the polarization vector and

$$A_{mn}(r) = \frac{u_{mn}(r;W)}{\left(1 + \frac{z^2}{b^2}\right)^{1/2}} e^{i \left[kz + \frac{k(x^2 + y^2)}{2R(z)} \right]} e^{i\delta_{mn}(z)} \quad (1)$$

The exponent $\phi(r) = k[z + (x^2 + y^2)/2R(z)]$ in (1) contains the rapidly varying phase on the wavelength scale $\lambda = 2\pi/k$. The constant phase wavefronts are spherical of curvature $1/R(z) = z/(z^2 + b^2)$. The spot size of the radiation envelope is $W(z) = w(1 + z^2/b^2)^{1/2}$, where $w = (2b/k)^{1/2}$ is the waist, and the distance z is measured from the position of the waist. The amplitude squared of the mode drops by 1/2 over a distance equal to the Rayleigh length b (also known as confocal parameter). Most of the radiation is confined within a cone parametrized by the diffraction angle $\theta_d = W/z = (\lambda/b\pi)^{1/2}$. The amplitude profile $u_{mn}(r;W)$ contains the transverse spatial variation, equivalent to a small k_{\perp} , perpendicular to the z -direction. Higher modes correspond to a larger effective k_{\perp} , responsible for the phase shift $\exp[i\delta_{mn}(z)]$. For a given k the mode is completely defined by the two independent parameters R and w (or any combination of two out of the four quantities R , w , z and b).

The functions $u_{mn}(r;W)$ depend on the elected coordinate system. In

rectangular coordinates (x, y, z) they are given by

$$u_{mn}(x, y; W) = a_{mn} H_m \left(\frac{\sqrt{2}x}{W} \right) H_n \left(\frac{\sqrt{2}y}{W} \right) e^{-\frac{x^2+y^2}{W^2}}, \quad (2)$$

where H_m, H_n are the Hermite polynomials, $a_{mn} = (2/W^2)^{1/2} (\pi 2^{m+n} m! n!)^{-1/2}$ is the normalization factor, setting the total electromagnetic flux carried by the mode equal to unity, and $\delta_{mn}(z) = (m+n+1) \tan^{-1}(z/b)$ is the slow phase. In cylindrical coordinates (r, θ, z) , where $\tan\theta = x/y$, $r = (x^2+y^2)^{1/2}$, $u_m^p(r, \theta; W)$ take the form

$$u_m^{\pm p}(r, \theta; W) = a_m^p \begin{pmatrix} \cos p\theta \\ \sin p\theta \end{pmatrix} \left(\frac{\sqrt{2}r}{W} \right)^p L_m^p \left(\frac{2r^2}{W^2} \right) e^{-\frac{1}{2} \frac{2r^2}{W^2}}, \quad (3)$$

where $+p$ ($-p$) signifies cosine (sine) poloidal dependence, L_m^p are the Laguerre polynomials, $a_m^p = (1/2\pi W^2)^{1/2} [m!/(m+p)!]^{-1/2}$ and $\delta_m^p(z) = (2m+p+1) \tan^{-1}(z/b)$.

The electron beam is an optically active medium that alters the characteristic parameters of the radiation after each passage. During the build-up period the modal content and the structure of the light pulses inside the oscillator will change. A numerical method has been developed recently optimizing the representation for the amplified radiation. In the source dependent expansion^{12,13} the waist size and the curvature of the elected modal basis is tailored according to the driving source term. That minimizes the number of modes required to describe the light beam. In general, the curvature and waist size of these modes does not match the curvature and waist of the vacuum eigenmodes for the resonator. Therefore the transfer matrix for a given mirror must be known for arbitrary incoming modes. This need stems from computational as well as physical reasons. The knowledge of the cavity reflection matrix R , together with the gain

matrix G through the wiggler, is necessary in determining the potential for steady state operation.

During high power operation, grazing mirror incidence may be necessary to avoid exceeding the dielectric breakdown limit for the reflection surface. Also, in case of a high per-pass gain with optical guiding, the waist for the reflected radiation would be much larger than the incoming. In two-mirror resonators the reflected radiation could hit the wiggler. Therefore, ring resonators, including three or more mirrors, must be employed for the deflection and recirculation of the light pulses. The study of the reflection matrix must be extended to include the effects of deflecting the light beam, in addition to finite mirror size and curvature mismatches.

The amplitude profile of the incoming radiation will be modified by reflection. A single incident mode $A_{mn}(r_i)$ will, in general, be partially reflected into different modes $A_{pq}(r_o)$ where $(m,n) \neq (p,q)$. This is caused by the deflection of the light beam, the finite size of the mirror and the curvature mismatches. Reflection into other modes will affect the interaction between the electron beam and the radiation in a number of ways. First the rms radius of the light beam will change, affecting the matching beam condition. Second, the light pulse will spread axially because of dispersion among different modes, since the phase velocity depends on the modal number (m,n) . Third, different phase advances during reflection among the various modes may render these modes out of phase after a number of bouncings off the resonator. For the above reasons the fraction of radiation scattered into other modes will contribute to the losses in FEL oscillators.

II. OUTLINE OF THE METHOD

The geometry of the reflection is illustrated in Fig. 1. The subscripts i and o denote the coordinate system used for expressing incoming and outgoing modes. r_i is defined with the \hat{z}_i axis along the direction of incidence and r_o has the \hat{z}_o axis along the direction of reflection. The origins are displaced from the mirror center by l_i and l_o respectively, where l_i is the distance of the minimum waist w_i for the incoming radiation and l_o is the distance of the minimum waist w_o for the reflected mode. A third coordinate system r_s with the origin at the mirror center and \hat{z}_s aligned with the mirror axis will be useful in the computations. Underlined quantities \underline{r}_i , \underline{r}_o and \underline{r}_s stand for the mirror surface coordinates in each reference frame. The transformations among the various frames are defined by.

$$x_i = x_s \cos \frac{\phi}{2} - z_s \sin \frac{\phi}{2},$$

$$x_o = x_s \cos \frac{\phi}{2} + z_s \sin \frac{\phi}{2},$$

$$y_i = y_s, \quad (4a)$$

$$y_o = y_s, \quad (4b)$$

$$z_i = z_s \cos \frac{\phi}{2} + x_s \sin \frac{\phi}{2} + l_i,$$

$$z_o = z_s \cos \frac{\phi}{2} - x_s \sin \frac{\phi}{2} + l_o.$$

We are interested in cases when the reflected radiation remains focused along some direction \hat{z}_o making an angle ϕ with the incoming \hat{z}_i . Then the reflected vector potential will also be expandable in free space eigenmodes $A_{pq}(r_o)$ of the paraxial equation in the new direction. The mirror surface generating focused reflection in the desired direction can not be arbitrary but must be appropriately defined. The angle of deflection ϕ will enter the equation defining the mirror surface. The other surface parameter, namely the curvature $1/R_m$, is a free parameter. It determines the curvature $1/R_o$ for the outgoing modes given the curvature $1/R_i$ of the incoming modes. In case of reflection by an arbitrary mirror

surface, the scattered radiation cannot, in general, be covered by the paraxial modes that do not form a complete set in three dimensions.

We consider incoming radiation of given curvature and of arbitrary amplitude profile $A^i(r_i)$, consisting of various modes (m,n) with the same $R_i(z)$. If both incident and reflected radiation are expanded into eigenmodes,

$$A^i(r_i) = \sum_{m,n} c_{mn}^i A_{mn}(r_i) , \quad (5)$$

$$A^o(r_o) = \sum_{p,q} c_{pq}^o A_{pq}(r_o) ,$$

the relation among the incident and reflected expansion coefficients c_{mn}^i , c_{pq}^o is formulated by

$$c_{pq}^o = R_{pq} c_{mn}^i , \quad (6a)$$

or

$$c_{pq}^o = \sum_{m,n} R_{pq}^{mn} c_{mn}^i , \quad (6b)$$

where R_{pq}^{mn} are the elements of the reflection matrix R .

We examine the case when the mirror dimensions ρ are much larger than the wavelength λ , $\lambda \ll \rho$ (otherwise diffraction rather than reflection would prevail). We also assume that the angle ζ subtended by the mirror $\zeta = \rho/R_m$, where R_m parametrizes the radius of curvature, is small, of the order of the diffraction angle θ_d , $\zeta = \theta_d = \epsilon$. The j -th component of the reflected vector potential at distance $|r_o - r_o| \gg \lambda$ from the mirror surface S is then given by

$$A_{(v)}^o(r_o) = -\frac{ik}{2\pi} \iint_S ds \frac{e^{ik|r_o - r_o|}}{|r_o - r_o|} A_{(v)}^s(r_o) (\hat{n} \cdot \hat{\Delta r}) . \quad (7)$$

In Eq. (7) $\hat{n} \cdot \Delta \underline{r}$ is the obliqueness factor where $\Delta \underline{r} = (\underline{r}_0 - \underline{r}_o) / |\underline{r}_0 - \underline{r}_o|$ and \hat{n} is the normal unit vector to the reflecting surface. The surface element ds is given by $ds = \delta[z_0 - f(x_0, y_0)] dx_0 dy_0 dz_0$ where $z_0 = f(x_0, y_0)$ is the surface equation. Equation (7) is the convolution of a source term $A^S(\underline{r}_o)$ at the mirror surface with the propagator $\exp(ik|\underline{r}_0 - \underline{r}_o|) / |\underline{r}_0 - \underline{r}_o|$, i.e., a superposition of spherical waves originating at S . The source term $A^S(\underline{r}_o)$ is specified from the incoming vector potential $A^i(\underline{r}_i)$ through the boundary conditions and the coordinate transformations (4). We will assume a perfectly conducting surface, where the incident and reflected fields are related by

$$A^S = -A^i + 2 (\hat{n} \cdot A^i) \hat{n}, \quad (8a)$$

and \hat{n} is the normal unit vector to the reflecting surface. When the solid angle subtended by the mirror is small, the last term in (8a) is very small and the boundary condition becomes,

$$A^S_{(v)} = -A^i_{(v)}. \quad (8b)$$

Relation (8b) corresponds to a phase shift by π during reflection. It is independent of the wave polarization, thus the subscript (v) is dropped. Cross polarization effects, due to the last term in (8a) are discussed in Ref. 10. Most of the computations will be performed on the mirror surface. To simplify the notation from now on, we drop the bar ($_$) under the mirror coordinates \underline{r} . Subscripted quantities such as r_i, r_o, r_s will signify the mirror surface in each reference frame. Unsubscripted coordinates will denote the observation point in the reflected radiation frame of reference.

We seek cases when the reflected radiation propagates focused along z_0 , contained within a cross section of dimensions $x, y \ll z - z_0$. The

expansion $|r-r_0| = (z-z_0) \{1 + [(x-x_0)^2 + (y-y_0)^2]/2(z-z_0)^2\}$ replaces the full propagator inside (7) with the paraxial propagator U_{-k} in that direction,

$$U_{-k}(r, r_0) = \frac{ik}{2\pi} \frac{e^{-ik(z-z_0)}}{z-z_0} e^{-ik \frac{(x-x_0)^2 + (y-y_0)^2}{2(z-z_0)}} \quad (9)$$

It is known that the profile of a given eigenmode $A_{mn}(x_0, y_0, z_0)$ at z_0 is generated by the propagator $U_k(r, r_0)$ acting on the mode $A_{mn}(x, y, 0)$ at $z=0$. The inverse propagator $U_{-k}(r, r_0)$ therefore reproduces $A_{mn}(x, y, 0)$ from $A_{mn}(x_0, y_0, z_0)$. This suggests multiplying and dividing the integrand inside (7) by $\exp[i\phi(r_0)] / [1 + z_0^2/b_0^2]^{1/2}$, recasting (7) in the form,

$$A^0(r) = \iint ds e^{i\Delta(r_0)} S(r_0) e^{i\phi_0(r_0)} U_{-k}(r, r_0), \quad (10)$$

where the source term $S(r_0)$ is,

$$S(r_0) = A^i[r_i(r_0)] (\hat{n} \cdot \Delta\hat{r}) \left[1 + \frac{z_0^2(r_0)}{b_0^2}\right]^{1/2}, \quad (11)$$

and the phase $\Delta(r_0)$ is given, in outgoing coordinates r_0 , by

$$\Delta(r_0) = k \left[z_i(r_0) + z_0 + \frac{x_i^2(r_0) + y_i^2(r_0)}{2R_i(r_0)} + \frac{x_0^2 + y_0^2}{2R_0(r_0)} \right]. \quad (12)$$

The expression for $\Delta(r_0)$ depends on the angle ϕ through the transformations between the incoming and the outgoing coordinates, Eqs. (4). Expression (10) is the approximation of the exact solution (7) to order

$[(x-x_0)^2 + (y-y_0)^2]/2(z-z_0)^2 - \epsilon^2$. It is valid provided that the surface S produces focused reflection along the desired direction. Otherwise, the paraxial limit will fail to encompass all the radiation contained in the original expression (7).

The term $\exp[i\Delta(r_0)]$ is varying rapidly, on the scale of the wavelength λ . Therefore, its convolution with the slowly varying source term over an arbitrary surface will be vanishingly small. In general, this corresponds to radiation scattering where only a small fraction of the incoming radiation is reflected along the considered direction ϕ . The integral (10) will be finite only when it is possible to satisfy the condition $\Delta(r_0) \approx \text{constant}$ over some surface S. If, in addition, S is much larger than λ , expression (10) will be finite only within a narrow angle $\delta\phi$ around ϕ . This guarantees that the reflected radiation remains focused along that direction. Therefore, a condition that the exact reflected radiation (7) be fully covered by the paraxial limit (10) is that

$$\Delta(r_0) = \text{const.}, \quad (13)$$

along the surface S. Accordingly, the optical path is the same along the various rays connecting an incoming wavefront with its mirror image (reflected) wavefront.

Requirement (13) defines the appropriate mirror surface $z_0 = f_0(x_0, y_0; \phi)$ for reflection in the elected direction. Expressing all quantities inside (13) in the mirror coordinate frame, applying the transformations (4) and using the scaling $x_s/R_m \sim y_s/R_m \sim \epsilon \ll 1$, $z_s/R_m \sim \epsilon^2$ we obtain from (13)

$$z_s = - \frac{1}{2R_m \cos \frac{\phi}{2}} \left[x_s^2 \cos^2 \frac{\phi}{2} + y_s^2 \right], \quad (14a)$$

where

$$\frac{1}{R_m} = \frac{1}{2R_o} + \frac{1}{2R_i}. \quad (14b)$$

Equation (14a) is the analytic expression for a paraboloid surface. R_m parametrizes the mirror curvature, being positive or negative for a convex or concave mirror respectively. The surface is reflection symmetric with $(zx)_s$ and $(zy)_s$ as the symmetry planes; there is no rotational symmetry around z_s . Surface (14a) can also be approximated, to second order in $(x_s/R_m)^2$, $(y_s/R_m)^2$ by hyperboloids or ellipsoids defined by

$$\left(z_s - R_m \cos \frac{\phi}{2}\right)^2 - x_s^2 \cos^2 \frac{\phi}{2} - y_s^2 = R_m^2 \cos^2 \frac{\phi}{2}, \quad (15a)$$

$$\left(z_s + R_m \cos \frac{\phi}{2}\right)^2 + x_s^2 \cos^2 \frac{\phi}{2} + y_s^2 = R_m^2 \cos^2 \frac{\phi}{2}. \quad (15b)$$

All the surfaces become spherical in the limit of perpendicular incidence $\phi = 0$, and plane mirrors when $R_m \rightarrow \infty$. Relation (14b) defines the curvature of the reflected modes from the incoming mode curvature and the curvature of the mirror.

Switching Eq. (12) into the mirror-aligned coordinates r_s through Eqs. (4), and using the surface constraints (14), it follows that

$$\Delta(r_s) = \text{const.} + O\left[k\rho \left(\frac{\rho}{R_m}\right)^2\right],$$

where ρ parametrizes the mirror size. A more complicated surface equation (higher than quadratic in x, y, z) is required to improve the constancy to a higher order. Since $k\rho \gg 1$, the approximation $\Delta(r_s) = \text{const.}$ is satisfactory for a first order expansion of the reflection matrix in powers of ρ/R_m , as long as $\rho/R_m \leq (k\rho)^{-1}$. In case $\rho/R_m > (k\rho)^{-1}$, the slow variation of $\Delta(x_s, y_s)$ over S must be included. That introduces an additional contribution in the reflection matrix, known as spherical aberration.

III. COMPUTATION OF THE REFLECTION MATRIX

The reflected radiation is expressed by

$$A^0(\mathbf{r}) = \int_S \int dx_0 dy_0 \sigma(x_0, y_0) e^{-i\phi_0(x_0, y_0)} U_{-k}(\mathbf{r}, \mathbf{r}_0), \quad (16)$$

where $\sigma(x_0, y_0) \equiv S[x_0, y_0, z_0(x_0, y_0)]$. Expanding the source $\sigma(x_0, y_0)$ in terms of $u_{mn}(x_0, y_0)$,

$$\sigma(x_0, y_0) = \sum_{m,n} R^{mn} u_{mn}(x_0, y_0; W_0). \quad (17)$$

and exploiting the property of the inverse propagator U_{-k} , the reflected vector potential $A^0(\mathbf{r})$ at $z = 0$ becomes

$$A^0(x, y, 0) = \sum_{m,n} R^{mn} u_{mn}(x, y; W_0), \quad (18)$$

where $W_0(z) = v_0 (1 + z^2/b_0^2)^{1/2}$, $v_0 = (2b_0/k)^{1/2}$. Expression (18) is a complete decomposition of the reflected radiation into paraxial eigenmodes for incident radiation of arbitrary profile.

According to the definition (6b), the R_{pq}^{mn} element of the reflection matrix R is obtained from the source term $\sigma_{pq}(x_0, y_0)$ inside (16) generated by a single incident eigenmode $A_{pq}[r_i(r_0)]$. The integration is performed in the mirror-aligned coordinates, taking advantage of the existing symmetries. The coordinates r_i and r_o , defining the incoming and outgoing wave functions, become explicit functions of x_s, y_s through the transformations (4). The surface equation (14a) is used to express z_s in terms of (x_s, y_s) . The mirror boundary

$$x_s^2 \cos^2 \frac{\phi}{2} + y_s^2 = \rho^2 \quad (19)$$

is defined by the intersection of the infinite surface (14a) with the plane $z_s = \text{const} = 2 \rho^2 \cos^2(\phi/2) / R_m$. After the above manipulations the reflection matrix elements take the form

$$R_{pq}^{mn} = \iint_S dx_s dy_s \frac{\bar{u}_{mn}(x_s, y_s) \bar{u}_{pq}(x_s, y_s)}{\left[1 + \frac{l_o^2}{b_o^2}\right]^{1/2}} \left[\frac{1 + \frac{z_o^2(x_s, y_s)}{b_o^2}}{1 + \frac{z_i^2(x_s, y_s)}{b_i^2}} \right]^{1/2} e^{i\Delta(x_s, y_s)} \quad (20)$$

$$\times e^{i\delta_{pq}^i(x_s, y_s) - i\delta_{mn}^o(x_s, y_s)} \left[\cos \frac{\phi}{2} \left(1 - \frac{x_s}{R_m} \sin \frac{\phi}{2} - \frac{x_s^2 \sin^2 \frac{\phi}{2}}{R_m^2} \right) \right],$$

where

$$\bar{u}_{mn}(x_s, y_s) = u_{mn}[x_o(x_s, y_s), y_s], \quad \bar{u}_{pq}(x_s, y_s) = u_{pq}[x_i(x_s, y_s), y_s].$$

Expression (20) is correct to order ρ^2/R_m^2 .

Each representation of R is tied to the choice of the basis functions $u_{mn}(r)$. In any case R, as given by (20), depends on four parameters¹⁰

$$R = R(\phi, \alpha, \mu; \xi). \quad (21)$$

ϕ is the reflection angle shown in Fig. 1. α is the ratio of the incoming to the outgoing spot size at the mirror, $\alpha = W_i(l_i)/W_o(l_o)$. $\mu = \rho/W_o$ parametrizes the mirror size compared to the radiation spot size. $\xi = W_o/R_m$ scales as the diffraction angle $\theta_d = W_o/l_o$ multiplied by the curvature mismatch R_o/R_m between the mirror and the radiation wavefronts. The spot size W_o enters as a free parameter because only the curvature $1/R_o$ for the reflected modes is specified by the mirror geometry. Since many

combinations of W_0 and l_0 apply to a given curvature according to paragraph Eq. (1), an additional selection rule for W_0 is needed. Note that W_0 does not have to match W_1 . This is obvious in cases when the mirror size ρ is smaller than W_1 . Each value of W_0 defines a complete set of modes for the reflected radiation, and an equivalent representation for R.

Parameters ϕ , α , and μ can be arbitrary. In most cases of interest, however, ξ is small, $\xi \ll 1$, of the same order as the diffraction angle θ_d . The analytic computation of the matrix elements is carried out by expanding the integral (20) in powers of ξ ,

$$R = R(0) + \xi R(1) + \xi^2 R(2). \quad (22)$$

The first order expansion is performed in Ref. 10. In this paper we review some of the general properties of R and focus on the reflection of the lowest mode u_{00} .

IV. LIMITING CASES

When the mirror radius tends to infinity ($1/R_m \rightarrow 0$), or in cases of vertical incidence on the mirror ($\phi = 0$), the higher order corrections in the reflection matrix R disappear,

$$R = R(0) \quad (23)$$

in both representations. The nondiagonal elements in R stem from the finite mirror size only. If, in addition, the mirror size is very large, $\mu \gg 1$, it is appropriate to take $W_0 = W_1$ as best representation for the reflected radiation. The $\alpha = 1$ limit yields

$$R_{pq}^{mn} = \delta_{pq}^{mn}. \quad (24)$$

Thus, in case of large curved mirror and vertical incidence, or large plane mirror and arbitrary incidence, the reflection matrix is the

identity matrix.

The case $\alpha = 1$ is of special interest for arbitrary angle of deflection ϕ and mirror curvature $1/R$, as it will be explained in the next section. For finite mirror size $\rho \geq \nu_0$, ($\nu \geq 1$), there exists zeroth order nondiagonal terms inside $R(0)$. Since $R(0)$ is independent of the angle of deflection ϕ , the mirror size yields the dominant contribution to the reflection into modes different than the incoming. The effects of the deflection of the light beam enter to first order in ξ , $R(1)$, or higher.

As the mirror size becomes very large and the limits of integration are extended to infinity the orthogonality among the various modes u_{mn} becomes effective. The off-diagonal terms in $R(0)$ become comparable to the first order terms $R(1)$ roughly when $1/\mu^2 \sim \xi \sim \theta_d$. At the limit $\mu \rightarrow \infty$ all the nondiagonal elements of R are reduced to order ξ or higher,

$$R_{pq}^{mn} = \xi R_{pq}^{mn}(1) + O(\xi^2), \quad m \neq p, n \neq q, \quad (25a)$$

and the only matrix elements of zeroth order in ξ are the diagonal

$$R_{mn}^{mn} = R_{mn}^{mn}(0) + O(\xi^2). \quad (25b)$$

in both Hermite and Laguerre representations. The lowest correction in the diagonal elements is of second order ξ^2 , while the first order contribution disappears. This is consistent with flux conservation during reflection in case of a large mirror.

The superposition principle can be used to describe reflection from more complex mirror surfaces. In case of a mirror with a hole the surface integral (7) over S is expressed as $\int_S = \int_{S_1} - \int_{S_2}$ where S_1 is defined by the mirror surface including the hole surface, and S_2 is the surface of the hole only. The total reflection matrix R is given by $R =$

$R(S_1) - R(S_2)$, the difference in the reflection matrices associated with mirrors S_1 and S_2 respectively. The transmission matrix T through a screen with an aperture of area S is given by $T = -R$, R being the reflection matrix for a mirror matching the aperture S . The transmission matrix, for radiation diffracted behind a finite size mirror is given by $T' = 1 - e^{i\pi} R$ where 1 is the identity matrix.

V. REFLECTION OF THE LOWEST ORDER MODE

The computation of all the truncated integrals for finite mirror surface is nontrivial. Most applications however involve the (0,0) lowest order mode as the dominant mode in both incoming and reflected radiation. The strategy here is to compute the element R_{00}^{00} of the reflection matrix first. Then the waist for the reflected modes W_0 can be selected so that it maximizes R_{00}^{00} . The optimum representation condition

$$\frac{\partial R_{00}^{00}}{\partial \alpha} = 0, \quad (26)$$

puts the maximum amount of the reflected radiation in the lowest mode (a different mode and matrix element may be chosen, if desired). It is pointed out that (26) does not improve the properties of the reflected radiation. It enables one to choose the best representation in terms of minimizing the coefficients of the undesired modes for the scattered radiation. Once W_0 is fixed by (26) then the exact location and size of the waist(s) for the reflected modes is determined by solving the system of equations

$$W_0 = v_0 \left[1 + \frac{l_0^2}{b_0^2} \right]^{1/2}, \quad \frac{1}{R_0} = \frac{l_0}{l_0^2 + b_0^2} \quad (27)$$

The element R_{00}^{00} is identical in both representations since the lowest order mode u_{00} is the same in rectangular and cylindrical coordinates. Performing the integration (20) yields R_{00}^{00} to first order in ξ

$$R_{00}^{00} = \frac{2\alpha}{1+\alpha^2} \left[1 - e^{-(1+\alpha^2)\mu^2} \right] + O(\xi^2). \quad (28)$$

Note that the first order term vanishes and the lowest correction is of second order in ξ^2 . The exact dependence on the mirror size ρ is parametrized by $\mu = \rho/W_0$, while $\alpha = W_i/W_0$ parametrizes the ratio of the incoming and scattered radiation spot sizes at the mirror. The optimization condition $\partial R_{00}^{00}(0)/\partial \alpha = 0$ yields, $\alpha^2 = 1 + \exp[-(1+\alpha^2)\mu^2] [\alpha^4 + (2\mu^2+1)\alpha^2 - 1]$. In case the mirror cross section is much larger than the spot size of the incoming mode, $\mu \gg 1$, $\alpha \rightarrow 1$ and the reflected spot size at the mirror matches the incoming, $W_0 = W_i$.

Large mirror size is desired to maximize the total reflection coefficient. The reflection coefficient η_R is given by $\eta_R = P_o/P_i$ where the incoming flux is $P_i = |c^i|^2 = \sum_{pq} |c_{pq}^i|^2$ and the outgoing flux is given by

$$P_o = |c^o|^2 = |R \cdot c^i|^2 = \sum_{mn} \sum_{pq} |R_{pq}^{mn} c_{pq}^i|^2. \quad (29)$$

In Fig. 2 we plot η_R for the lowest order incoming mode as a function of $\mu' = \cos(\phi/2) \rho/W_0 = \cos(\phi/2) \mu$. μ' parametrizes the size of the mirror surface projection into the plane perpendicular to the incoming radiation direction. The incoming radiation has a wavelength $\lambda = 1\mu$ (10^{-4} cm), waist $w_i = 10^{-2}$ cm at distance $l_i = 2.5 \times 10^3$ cm from the mirror and radius of curvature (at the mirror) $R_i = 2.5 \times 10^3$ cm. The mirror has a radius of curvature $R_m = 2.5 \times 10^3$ cm, yielding reflected modes of $R_o =$

2.5×10^3 (again l_0 and v_0 depend on the choice of W_0). In Fig. 3 we plot the reflection coefficients R_{pq}^{00} of the lowest order mode (0,0) into the first 25 modes (p,q) with $p \leq q \leq 5$, as a function of μ' . The deflection angle is 90° and the ratio of the spot sizes is 1. Increasing mirror size maximizes the diagonal element and minimizes scattering into other modes.

In Fig. 4 we fix the mirror size $\mu' = 2$ and the angle $\phi = 90^\circ$ and vary the spot size ratio α . The best representation, maximizing R_{00}^{00} and minimizing R_{pq}^{00} is obtained at $\alpha = 1$. However, for small mirror $\mu' = 0.66$, the maximum for R_{00}^{00} occurs at $\alpha \approx 0.70$ (see Fig. 5). Radiation reflected off mirrors smaller than the incoming spot size is best described by outgoing modes of reduced spot size $W_0 < W_i$. Also note from Fig. 5b that for small mirror size the total power reflected into the first 25 modes never exceeds 80% of the incoming flux; even with many more modes η_R remains less than 1. In Fig. 6 the reflection coefficients R_{pq}^{00} are plotted as functions of the angle of deflection ϕ for fixed $\alpha = 1$, $\mu' = 2$. It is seen that, for sufficiently large reflecting surface and good choice of the spot size W_0 , the reflection matrix is not very sensitive to ϕ . Comparison of Figs. 2 and 3 with the rest of the plots shows that the relative mirror size to the radiation spot size is the most important parameter to determine the reflection into other than the incoming modes.

ACKNOWLEDGEMENT

This work supported by SDIO and managed by SDC.

References

1. L. R. Elias, W. M. Fairbanks, J. M. J. Madey, H. A. Schwettman and T. I. Smith, *Phys. Rev. Lett.* 36, 717 (1976).
2. T. I. Smith, H. A. Schwettman, R. Rohatgi, Y. Lapierre and J. Edighoffer in Proceedings of the Eighth International FEL Conference, Glasgow, Scotland, edited by M. Poole (North Holland, Amsterdam, 1987), p. 1.
3. R. W. Warren, D. W. Feldman, B. E. Newnam, S. C. Bender, W. E. Stein, et al., in Proceedings of the Eighth International FEL Conference, Glasgow, Scotland, edited by M. Poole (North Holland, Amsterdam, 1987), p. 8.
4. K. E. Robinson, T. L. Churchill, D. C. Quimby, D. M. Shemwell, J. M. Slater, et al., in Proceedings of the Eighth International FEL Conference, Glasgow, Scotland, edited by M. Poole (North Holland, Amsterdam, 1987), p. 49.
5. M. Billardon, P. Elleaume, J. M. Ortega, C. Bazin, M. Bergher, et al., in Proceedings of the Eighth International FEL Conference, Glasgow, Scotland, edited by M. Poole (North Holland, Amsterdam, 1987), p. 72.
6. T. Masud, T. C. Marshall, S. P. Schlesinger and F. G. Yee, *Phys. Rev. Lett.* 56, 1567 (1986).
7. X. K. Maruyama, S. Penner, C. M. Tang and P. Sprangle, in Proceedings of the Eighth International FEL Conference, Glasgow, Scotland, edited by M. Poole (North Holland, Amsterdam, 1987), p. 259.
8. S. Solimeno and A. Torre, *Nucl. Instr.* A237, 404 (1985).
9. J. A. Murphy, *Intl. J. Infrared and Millimeter Waves* 8, 1165 (1987).
10. S. Riyopoulos and C. M. Tang, submitted for publication (1988).
11. See, for example, H. A. Hauss in Waves and Fields in Optoelectronics, (Prentice Hall, New Jersey, 1984), p. 180, and references therein.

12. P. Sprangle, A. Ting and C. M. Tang, Phys. Rev. Lett. 59, 202 (1987).
13. P. Sprangle, A. Ting and C. M. Tang, Phys. Rev. A36, 2773 (1987).

Figure Captions

Figure 1 Reflection geometry.

Figure 2 Plot of the total reflection coefficient η_R for the lowest order mode as a function of the mirror size μ' for $\phi = 90^\circ$ and $W_0 = W_i$.

Figure 3 Plots of the reflection matrix elements of the lowest order mode (0,0) into the first 25 modes $p \leq q \leq 5$. The magnitude $|R_{pq}^{00}|$ is plotted against the relative mirror size μ' . The angle of deflection $\phi = 90^\circ$ and $\alpha = 1$ ($W_i = W_0$).

Figure 4 Plots of (a) the reflection matrix elements $|R_{pq}^{00}|$, and (b) the reflection coefficient η_R into the first 25 modes, against the spot size ratio α for $\mu' = 2$ and $\phi = 90^\circ$.

Figure 5 Same as in Fig. 4 for $\mu' = 0.5$.

Figure 6 Plots of the reflection matrix elements $|R_{pq}^{00}|$ against the angle of deflection ϕ for $\mu' = 2$ and $\alpha = 1$.

